博 士 論 文

Structural Characterization of Hydrogenated Amorphous Carbon (a-C:H) Coating by Solid State ^{13}C NMR and Its Wear Mechanism under Shear

（固体^{13}C NMR法を用いた水素化非晶質炭素薄膜構造特性評価とせん断応力下の摩耗メカニズムの解析）

許 佼

CONTENTS

Acknowledgements

At the very first, I am honored to express my deepest gratitude to my dedicated supervisor Prof. Kato, who offered me invaluable help and constant encouragement during the three years of my doctoral program at University of Tokyo, and walked me through all the stages of writing this thesis. Without his scientific instructions, the thesis could not achieve its present form. I would like to express my heartfelt gratitude for his illuminating ideas, suggestions and criticisms with profound knowledge and rich research experience. I have learnt a lot from him not only about professional research but also professional ethics, both of which are inevitable characters to prepare myself as an excellent researcher in future.

Meanwhile, I am also extremely grateful to Dr. Kawaguchi, Dr. Watanabe and Dr. Hayashi from Tokyo Metropolitan Industrial Technology Research Institute (TIRI), as well as Prof. Choi and Prof. Nosaka from the University of Tokyo, for their meticulous guidance and invaluable suggestions in my experiments which are indispensable for the completion of this thesis.

Lastly but not least, my thanks would go to my beloved family for their loving considerations and great confidence in me all through these years, as well as my boyfriend for his meticulous love and solid support all the way from the very beginning of my study. Also, sincere gratitude is owed to my friends who listened to me and helped me during the hard period of overseas life.

Abstract

In this thesis, structural characterization of ion-vapor deposited hydrogenated amorphous carbon (a-C:H) coating has been studied by applying solid state ^{13}C NMR. Primarily, the $sp^3/(sp^3+sp^2)$ ratio of a-C:H coatings deposited under various substrate bias voltages within 0.5~3.5 kV was obtained by using ^{13}C MAS technique. As the bias voltage grew from 0.5 kV to 2 kV, both the hardness and residual stress of studied coatings reached its maximum value and then gradually reduced with further increase of bias voltage up to 3.5 kV, while the $sp^3/(sp^3+sp^2)$ ratio reduced continuously within the whole range of 0.5~3.5 kV. Also, higher $sp^3/(sp^3+sp^2)$ ratio was obtained by ^{13}C CPMAS spectra than that of ^{13}C MAS, which implies that in studied a-C:H coatings, there is a preferential coordination of hydrogen atoms to sp^3 C. Thus, the coating mechanical property is specifically proportional to the fraction of diamond-like cross-linked sp^3 C, rather than the total population of sp^3 C.

By employing ^{13}C MAS and ^{13}C CPMAS techniques, heterogeneous nanoclustering structure has been observed in studied a-C:H coatings. Two distinct types of sp^2 C clusters were discovered: one of them denoted as sp^2 C′ in content of 3~12 at.% is specifically localized in hydrogen-free regions, and the other in majority denoted as sp^2 C″ is hydrogenated or at least proximate to hydrogen atoms. As maximizing π bond energy tends to cause a segregation between sp^2 and sp^3 C and form localized sp^2 C clusters within sp^3 bonded matrix, the size of sp^2 C clusters is strongly dependent on ion energy in deposition process and thus affects the disordering of carbon network in medium range order. On basis of the notably consistent dependence of sp^2 C′ fraction and Raman G peak width on bias voltage within 0.5~3.5 kV, a heterogeneous nanoclustering model of sp^2 sites has been proposed in this thesis that the sp^2 C′ sites are embedded between dominant sp^2 C″ clusters and sp^3 C matrix as grain boundaries or trapped interfaces where sp^2 hybridized bonding are highly distorted. According to the Raman and optical band gap characterizations, it was learnt that the continuous grow of bias voltage can promote the nanoclustering of dominant sp^2 C″ clusters and

thus determine the fraction of boundary sp^2 C′ sites. When bias voltage is below 1 kV, there is a low localization of sp^2 C" sites with small cluster size so that the fraction of boundary sp^2 C' sites is also few; as it grows to 1.0~2.5 kV, higher ion energy enhances the clustering of sp^2 C into six-fold aromatic rings so that both the size and population of sp^2 C" clusters increases largely, and accordingly the fraction of boundary sp^2 C' sites increases obviously; however, further increase of bias voltage may promote a large expansion of sp^2 C" clusters through inter-connecting and re-ordering of individual sp^2 C" clusters into larger ones, so that the fraction of boundary sp^2 C′ sites will decrease significantly in turn. Consistently, as an effective indicator of carbon network disordering, the Raman G peak width increased to its maximum value at 2.0 kV and then gradually reduced with a gradual increase of bias voltage within 0.5~3.5 kV.

To confirm the validity of presented heterogeneous clustering model, an exponential fitting analysis on magnetization relaxation curve of sp^2 C″, sp^2 C′ and sp^3 C spins has been attempted by using saturation recovery technique. Results revealed that the spin-lattice relaxing of sp^2 C″ spins exhibited a typical stretched-exponential approximation with stretched index α equal 0.8 and T_1 equal 2.8 s, while the sp^2 C′ spins showed a typical single-exponential approximation with T_1 equal 5 s due to its hydrogen-free feature, and the sp^3 C spins showed single-exponential approximation with T_1 equal 3.7 s. Such differences of T_1 among sp^2 C″, sp^2 C′ and sp^3 C spins verify the heterogeneous structure of studied a-C:H coatings, and the stretched-exponential approximation of sp^2 C″ spins obviously suggests a partial distribution of paramagnetic centers near sp^2 C″ clusters. For ^{1}H spins, the magnetization recovery curves showed fine stretched-exponential approximation with stretched index α about 0.5 and T_1 within 20~40 ms and better bi-exponential approximation with two T_1 components fluctuating within 25~55 ms and 0.1~0.3 ms in fraction of 70~80% and 30%~20%, respectively, while both the ultra short component of T_1(H) and the stretched index α approaching 0.5 certainly suggest considerable presence of paramagnetic centers in studied coatings. An interrupted ^{13}C CPMAS saturation

recovery spectra with relaxing interval as the short component of T_1(H) showed that most of quick-relaxing protons localize in sp^2 C″ clusters but nearly absent in sp^3 matrix and boundary sp^2 C' sites. The Raman and optical band gap characterization revealed that the size of sp^2 C cluster grew continuously with an increase of bias voltage, yet below the threshold value of 2 nm.

In light of the specific heterogeneous structure of studied a-C:H coatings, their tribological property and wear mechanism in N_2 atmosphere and ambient air has been investigated by using a standard ball-on-plate tribometer. Obvious correlations between nanoclustering structure and friction performance of a-C:H coatings has been observed, especially as the tribotests conducted in N_2 atmosphere. Comparatively higher friction coefficient generally occurred in tribotests of diamond-like coatings, namely as bias voltage was 1.0~2.0 kV, while lower friction coefficient usually occurred in polymer-like and graphite-like coatings (still with hydrogen content about 18 at.%). A characterization of wear marks by Raman spectroscopy demonstrated that compared with as-deposited coating, the ball scar derived from B2.0 coating showed largest growth of *I(D)/I(G)* and reduce of G peak width with moderate upward shift of G peak position which implied a great transformation of sp^3 C to amorphous sp^2 C in aromatic rings, while the ball scar derived from B0.5 coating showed a reduce of *I(D)/I(G)* and G peak width with moderated upward shift of G peak position which implied a transformation of sp^2 C from aromatic rings to chains, in coordination with hydrogens and showing good solid lubricity. It seems that the boundary sp^2 C' sites trapping around sp^2 C" clusters may inhibit the formation of lubricant transfer layers enriched of sp^2 C-H bonds in chains under dry sliding conditions and lead to high friction coefficient.

Meanwhile, by performing overlapping tribotests of a-C:H coating/steel ball tribopairs in ambient air, both the morphological and chemical characteristic evolution of transfer layers during dry sliding were tracked by *ex situ* optical microscopy, XPS and SEM/EDX. Experimental results show that carbon-based transfer layer can be quickly built up in the first sliding cycle and covered by an oxygen-rich

chemisorption layer on the top surface. At the beginning of running-in period, steel balls are consumed more rapidly than a-C:H coatings so that transfer layer was mainly composed of loosely compacted debris with relatively higher content of iron oxides, and consequently brought out severe third-body abrasion of counterface. As sliding go by, size of wear debris decreases a lot while their compactness and adherence to steel surface improves markedly, finally leading to a gradual reduce of wear rate and friction coefficient. This ever-evolving wear process of studied a-C:H coating/steel ball tribopairs sliding in ambient air can be summarized by a three-stage model as presented in this thesis, taking the close correlations between average contact pressure and wear rate of sliders into consideration. The XPS detection of transfer layers showed that except for the widely-reported graphitization of carbons, a noticeable tribochemical oxidation on the top surface of transfer layers was also observed and strongly affected friction coefficient.

1 General introduction

Since the first deposition of amorphous carbon coating by Aisenberg and Chabot [1], hydrogenated amorphous carbon (a-C:H) coating has attracted great interesting for their outstanding performance such as high hardness and wear resistance, low friction in various conditions, wide band gap, good chemical inertness and promising potential as solid lubricants [2, 3]. Compared with naturally sp^3 or sp^2 hybridized carbon materials like diamond and graphite, a-C:H coating is composed by a combination of these two phases in an amorphous manner, with a coordination with hydrogen atoms. Reviewing the booming development of amorphous carbon coatings in past three decades, various types of carbon coatings have been investigated with a wide range of sp^3 hybridization and hydrogen contents [3-5], typically as described in Fig. 1.1 [6]. Correspondingly, the various types of carbon coatings exhibit a wide range of properties, particularly as the nanoindented hardness within 5~80 GPa and friction coefficient within the level of super-lubricity to 0.6. In total sp^3-hybridized phase like diamond, four valence electrons of carbon atom are coordinated to a tetrahedrally sp^3 orbital and make strong σ bonds to adjacent atom. In total sp^2-hybridized phase like graphite, three of the four valence electrons are coordinated to a trigonally sp^2 orbital forming σ bonds in a plane, and the forth electron lies in a pπ orbital normal to the σ plane forming a π bond. Specifically, the tetrahedrally coating (ta-C) usually prepared by filtered cathodic vacuum arc (FCVA) contain more than 80 at.% of sp^3 C and has high hardness around 80 GPa, while the magnetron sputtered a-C coating usually contain 20~30 at.% of sp^3 C and has hardness around 8~16 GPa [3~5]. By applying ion vapor or plasma deposition methods which use hydrocarbon gases as the carbon source, hydrogen atoms are doped into amorphous carbon coating and play an important role in its tribological performance [7-10]. In terms of the hydrogen content and carbon network features, a-C:H coatings are widely classified as polymer-like, diamond-like, and graphite-like coatings [8-11]. Tailoring the

$sp^3/(sp^3+sp^2)$ ratio and hydrogen content by controlling deposition methods and some critical parameters such as carbonaceous precursor, substrate material and temperature, depositing pressure and bias voltage, etc., the lubricant property of a-C:H coatings can be designed to meet diverse requirements for industrial applications.

To understand the complex correlations between structural characteristics and excellent performance of a-C:H coatings, there are some inevitable items especially as grasping the $sp^3/(sp^3+sp^2)$ ratio and clustering structure of a-C:H coatings. Besides, a deep understanding of fabricated defects would also be an indispensable item in recent study of a-C:H coatings. This doctoral thesis is aiming at the structural characterization of ion-vapor deposited a-C:H coating by using solid state ^{13}C NMR, and investigating the effects of clustering structure on tribological performance of a-C:H coatings. Except for a briefly introduction on the basic principles of solid state ^{13}C NMR characterization and relative experiments in Chapter 2, the original work of this thesis are reported in the following chapters as illustrated in Fig. 1.2. Specifically, Chapter 3 describes the fragment sample preparation for solid state NMR, particularly as regard to the chemical inertness of a-C:H fragment in acidic solutions; Chapter 4 reports the $sp^3/(sp^2+sp^3)$ ratio determined by different NMR techniques and compares the results with other characterization techniques; Chapter 5 presents the heterogeneous clustering structure of sp^2 sites and its growth mechanism; Chapter 6 reports the friction behavior and wear mechanism of a-C:H coating sliding against steel ball in N_2 atmosphere and ambient air, and discusses the correlations between clustering structure and tribological performance.

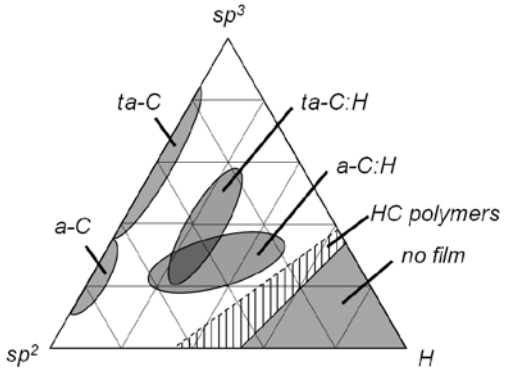

Fig. 1.1 Ternary phase diagram of bonding in amorphous carbon coatings.

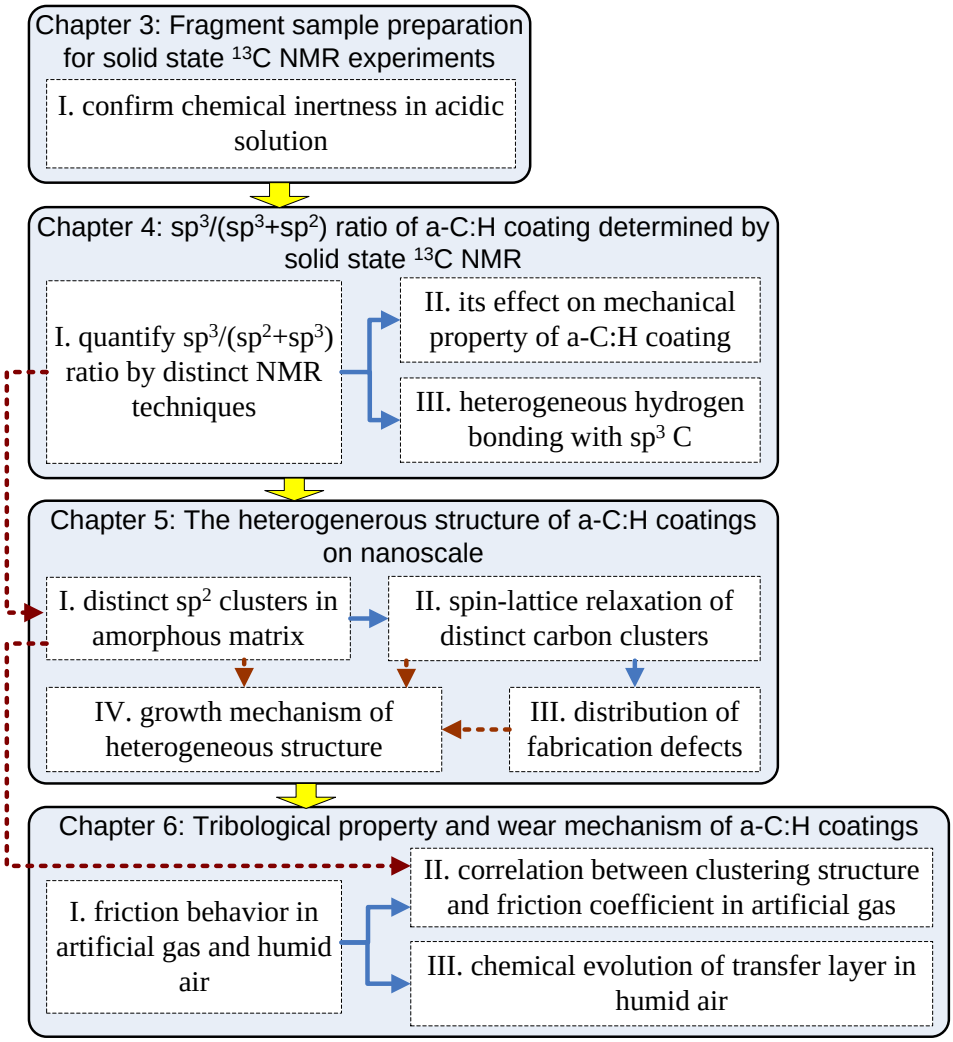

Figure 1.2 The outline of original work in this doctoral thesis and the emphases in each chapter.

1.1 Methods of chemical characterization for a-C:H coating

Generally, in order to characterize the chemical bonding of a-C:H coating, various techniques are employed which can be divided into three categories, that is optical spectroscopy, the electron spectroscopy and magnetic resonance [12].

1.1.1 Optical spectroscopic methods

Optical spectroscopic characterization such as Raman and infrared spectroscopy are the most convenient and frequently employed nondestructive techniques for qualitative study of bonding type and clustering structure of carbon coatings [13~20]. For example, the feature of visible Raman spectroscopy is its large sensitivity to sp^2 C

which can effectively follow the structural transformation of sp^2 sites. For all kinds of carbon coatings, their Raman spectra can be deconvoluted into two characteristic peaks: a graphite peak (G peak) center around 1580 cm^{-1} attributed to the stretching vibration of the sp^2 sites both in olefinic and aromatic structure, and a disorder peak (D peak) center around 1350 cm^{-1} merely attributed to the breathing mode of sp^2 sites in aromatic rings in an amorphous manner [13~16]. Generally, in analysis of visible Raman spectra, the peak intensity (or area intensity) ratio of D and G peaks, i.e. *I(D)/I(G)*, indicates the in-plane crystallite size and fractions of sp^2 C in aromatic rings [13], and the half-maximum (*FWHM*) of G peak represents the degree of network disordering [13, 21, 22]. Also, the center position of G peak is an sensitive indicator of graphite-like sp^2 clustering and generally shifts to higher wavelength as a function of substrate bias voltage [13-16, 21, 22]. However, the Raman excited by visible photons is merely sensitive to sp^2 sites but blind to sp^3 sites due to their higher lying σ states. Instead, the Ultra-Violet (UV) Raman at 244 nm (>5 eV) can provide higher energy for σ states excitation of both sp^2 and sp^3 sites, thus allows a direct observation of sp^3 sites. In UV Raman spectra of a-C:H coatings, except for the dominant G peak center around 1580~1620 cm^{-1} and a weak D peak around 1450 cm^{-1}, a new peak denoted as T peak appears around 1060~1100 cm^{-1} arising from sp^3 sites [13, 16, 17]. By deconvolution fitting, semi-quantitative information on $sp^3/(sp^3+sp^2)$ ratio can be investigated in terms of the shift of T and G peak and peak intensity ratio. With an increase of $sp^3/(sp^3+sp^2)$ ratio, both the ratio of *I(T)/(I(T)+I(G))* and G peak position will grow up to 0.3 and 1660 cm^{-1}, respectively, whereas the T peak position will shift down to 1050 cm^{-1} [23, 24]. However, it should be noticed that in UV Raman, the sensitivity to sp^2 Raman vibrations is still stronger than that to sp^3 by a factor of 5–10, hence can hardly be applied for quantitative analysis of sp^3 C fractions [12].

Another frequently applied optical spectroscopy is Infra-Red (IR) spectra which shows a wide region of vibrational transitions within 4000~10 cm^{-1} and preferable for the characterization of hydrogenated carbon coatings. Some researchers analyzed IR

spectra for semi-quantitative distinguishing of hydrogenated and non-hydrogenated sp^3 carbons [18, 19, 25] on basis of vibrational frequency attributions to various types of C-H bonds [3, 26, 27].

1.1.2 Electron spectroscopic methods

More accurate techniques for chemical composition and structure characterization of a-C:H coatings are electron spectroscopy, which typically includes scanning electron spectroscopy (SEM), X-ray photoelectron spectroscopy (XPS), X-ray near edge absorption spectroscopy (XANES), Auger electron spectroscopy(AES), transmission electron spectroscopy (TEM) and electron energy loss spectroscopy (EELS), etc. [28-33]. In case of XPS characterization, when the surface is irradiated by X-ray, an electron emission is resulted within the escape depth of photoelectrons near surface region, and the kinetic energy of emitted photoelectrons can be described by Eq. (1.1) [12]

$$E_k = h\nu - E_b - W_s \qquad (1.1)$$

where $h\nu$ is the energy of incident photon, E_b the binding energy of atomic orbital from which the electron originates, and W_s the spectrometer work function. As each type of chemical bond has a unique set of binding energies, their differences in chemical state can be revealed through the variations of binding energy, and the fraction of each type of chemical bond is linearly to the peak intensity of XPS spectra [28]. For example, in XPS spectra of C1s peak, the binding energy of sp^2 C=C is 284.5 eV, 0.8 eV lower than that of sp^3 C-C (284.5 eV) [28, 29, 30]. Well-accepted attributions of binding energy to diverse C- bonds have been listed in the handbook of X-ray photoelectron spectroscopy [30], except for the C-H bond which limits the application of XPS for hydrogenated carbon materials to some extent. However, it should be realized that the fractions of each type of bonds obtained through deconvolution fitting of XPS spectra is strongly affected by peak fitting formulas and constraint parameters, especially as the combined ratio of Gaussian and Lorentzian formulas, the width limit of each sub-peak and the shape of baseline [22, 28].

Similarly, the Auger electron emission arising from the creation of ions with an inner shell vacancy has also been investigated by using higher energy irradiation for chemical characterization of a-C:H coatings [31]. However, it is argued that the high-energy electron irradiation for long time in AES experiments can cause a local structural destruction of coating surface, thus make misunderstanding on chemical structure of bulk material [32].

Moreover, a spectroscopic analysis on the inelastic scattering energy loss of incident electrons after the interaction of electrons with coating surface generates EELS spectra [33, 34]. It typically includes a low loss region within 0~40 eV and a high loss region at C 1s (K edge) above 285 eV which is specifically named by XANES [35, 36]. A well-accepted quantification method of sp^2 fraction by EELS spectra was proposed by Berger et al. [34], who calculated the area intensity of 1s-π* carbon pre-K edge of tested sample and compared it with the EELS spectra of standard sample graphite within an appropriate energy window. Besides, Alexandrou et al. [37] proposed to use C60 as the standard sample to eliminate the orientation dependence side effect of graphite crystalline. However, the disadvantages of EELS are that the C 1s K edge only represents sp^2 sites, and the tested coatings must be detached from substrate materials and irradiated by high energy electron beam which may cause destructive damage of as-deposited coating.

1.1.3 Magnetic resonance methods

The third alternative method of chemical characterization for a-C:H coatings is magnetic resonance, typically as solid state NMR and EPR. The former one can be employed for the accurate quantification of sp^3 fractions [38-41], while the latter one is primarily used for the detection of fabricated defects in amorphous materials [42, 43]. Briefly, the mechanism of NMR experiment is that in static magnetic field M_0, the nuclei with magnetic moment μ may interact with the radio frequency (r.f.) irradiation, thus elucidates rich information on the local chemical environment of nuclear spins and the chemical structure of bulk material. NMR can inherently achieve a quantitative analysis on $sp^3/(sp^3+sp^2)$ ratio at molecular level, since the

intensity of macroscopic magnetization is well-linear to the concentration of NMR-active nuclear spins. More importantly, in NMR spectra each type of hybridization phase can give rise to a separate chemical shift with the same weighting factor [3]. Thus, NMR has been popularly applied as the most direct measurement of sp^3 fractions for carbon compounds such as coals and polymers [44-48]. Meanwhile, in NMR experiments we can use ^{1}H-^{13}C cross-polarization technique to evaluate the distance between ^{13}C and ^{1}H spins [39-41], and use magnetization recovery techniques to understand the clustering structure and fabrication defects of a-C:H coatings [41-43].

1.2 Friction behavior and wear mechanism of a-C:H coating in various atmospheres

While the mechanical property of a-C:H coatings is primarily determined by deposition methods, carbon sources, working pressure, substrate temperature, post-treatments of coating, etc., their tribological performance is additionally affected by sliding conditions, especially as friction atmosphere, relative humidity, loading conditions, sliding velocity, type of sliding motion, counterpart materials, etc. The contribution from each factor to the overall friction behavior varies from one type of a-C:H coating to another due to different tribochemical reactions [3, 4, 49-52]. Generally, the friction coefficient (CoF) of a-C:H coating ranges between 0.05 and 0.3 in ambient atmosphere [3, 4, 49, 50], and falls down to 0.01 in inert atmospheres (e.g. ultra-high vacuum (UHV) [7-9, 53], dry N_2 [4, 5, 54, 55]) and dry H_2 atmosphere [7, 8, 10, 53].

1.2.1 Lubricant mechanism of a-C:H coating

According to present reports, the solid lubricant mechanisms of a-C:H coating have generally been ascribed to two hypotheses, i.e. the friction-induced graphitization of carbon material and the passivation role of hydrogen atoms on contact surface [11]. The determinant lubricant mechanism varies from the types of a-C:H coatings and sliding conditions [3, 56]. Generally, the reports discussing about the effects of normal

load and sliding speed tend to support the friction-induced "graphitization" hypothesis [57-60], while the reports of sliding experiments in inert atmosphere and H_2 atmosphere, and the molecular dynamic (MD) simulations favor the "hydrogen passivation" mechanism [8, 11, 61, 62].

Earlier research of Racine et al. [56] and Erdemir et al. [57, 58] reported a typical decrease of CoF during running-in period which was accompanied by an establishment of friction-induced transfer layer between sliding counterparts. The Raman characterizations of carbon-based transfer layer had obviously suggested an increase of sp^2 C=C bonds in aromatic rings, which was clearly different from as-deposited coatings [57, 59]. They attributed the low CoF in steady state sliding to the weak shearing force between friction-induced graphite-like interlayer. However, other characterizations by TEM and EELS had generally revealed an amorphous structure of transfer layer [58, 63], and so far, no evidence has been proposed to correlate the reduce of CoF clearly to the degree of graphitization on contact surfaces.

By comparison, the "hydrogen passivation" mechanism can well explain the low friction behavior of a-C:H coating with a hydrogen content above 30 at.% [7, 9, 10] sliding in N_2 atmospheres, and is consistent with the loss of hydrogen content (or hydrogen diffusion [7, 10, 53-55] from inner of coating) on sliding surfaces. The polymer-like transfer layer in rich of sp^2 CH_2 chains can protect the tribopairs from direct rubbing and release the shearing force easily on hydrogen-saturated surfaces [4, 5]. The free electrons of hydrogen atoms may bond with dangling σ-bonds of carbon atoms on top surfaces, and the electrical charge density is permanently shifted to the other side of hydrogen atoms and away from contact surfaces [4].

1.2.2 Effects of humidity and oxygen in sliding atmosphere

The presence of H_2O and O_2 molecules in sliding atmospheres may affect the tribological property of amorphous carbon coatings strongly, and generally it causes an increase of CoF for a-C:H coatings. Typically, Erdemir [4] reported a great increase of CoF from 0.001 in dry N_2 to 0.04 in humid N_2 with additional presence of O_2 and 0.06 in humid air. The reason put forward in Ref. [4] is that there were lots of

free σ-bonds created on sliding surfaces which can chemically bond to active species from surrounding atmospheres and form strong adhesion forces between counterface. A similar degradation of CoF due to the large adhesion force had been discussed by other reaearchers [8, 52, 64, 65]. For example, Kim [52] observed a different dependence of CoF on atmosphere humidity for a-C:H coatings sliding in Ar atmosphere and ambient air. In his experiment, when the relative humidity of Ar atmosphere increased from 0% to 50% and 100%, the steady CoF grew up from 0.06 to 0.19 and 0.99, whereas in air with the same humidity, the CoF only fluctuated from 0.16 to 0.08 and 0.19, respectively. Also, Yuichi [65] found that when the plasma-deposited a-C:H coatings were exposed in ambient air with relative humidity of 50% for hours, an oxidation layer as thick as 1 nm with high content of C=O and C–O–C groups could be formed on the top surface of coating and lead to a rise of CoF from 0.2 to 0.4 sliding in humid air. However, different results were reported by Donnet et al [66] who controlled the partial pressure of H_2O and O_2 in UHV. When the partial pressure of O_2 in UHV increased from 0 to 60 hPa, the ultra-low friction behavior of a-C:H coating did not change markedly; in contrast, when the partial pressure of water vapor in UHV slightly increased from 0 to 0.5 hPa (relative humidity 2%), the CoF jumped from 0.01 to 0.1. They attributed the jump of CoF to the greatly reduced thickness of transfer layers [66]. Also, the weaker tribochemical effect of O_2 molecular than H_2O on high CoF of a-C:H coating were reported in Ref. [67].

1.2.3 Effects of friction-induced transfer layer

To achieve a steady low CoF in various sliding atmospheres, the formation of durable transfer layer is a dominant factor, which can protect rubbing counterparts from direct contact and confine the shearing force occurring between interfacial layers. The shearing ability of transfer layer is strongly dependent on the nature of as-deposited coating, sliding atmosphere and tribochemical interactions [63]. Compared with the tribotests of a-C:H coatings sliding against steel balls, durable

transfer layer has hardly been observed on ceramic balls sliding against a-C:H coatings [68], generally resulting in a relatively higher wear rate of counterparts [69]. For example, Erdemir et al. [70] slid ion-beam deposited a-C coatings against sapphire balls and observe no transfer layer on sapphire balls, and the same results were reported by Ronkainen et al. [71] and Lempert et al. [72] using alumina balls. The high CoF caused by using ceramic sliders can be solved by introducing doped atoms such as nitrogen into amorphous carbon coatings, typically as reported by K. Kato and N. Umehara et al. [73-75].

In order to characterize the structure of friction-induced transfer layer, various characterization techniques have been applied and widely revealed a graphitic transformation of carbon bonds in an disorder manner that was obviously different from "parent" coatings [5, 54, 57, 58]. In this issue, visible Raman spectroscopy is particularly popular because of its simplicity, time efficiency and high sensitivity to sp^2 hybridized carbons. Typically, Scharf and Singer et al [76-81] developed an *in situ* Raman spectroscopy to track the shift of Raman G and D peaks of transfer layers generated by various sliding distances without a counterpart separation after sliding tests. Unfortunately, to make a compromise of data acquisition and Raman spectra resolution, all the tribotests were performed at very low sliding velocity as 1 mm/s, and the acquired spectra could only elucidate comprehensive information of transfer layer and underneath coating. Besides, the carbon oxides [52, 65] and metal oxides [81] composed together in transfer layers can hardly be analyzed by Raman spectroscopy. Thus, in the study of wear mechanism in this thesis, we designed one set of overlapping sliding tribotests to track the evolution of transfer layers dynamically and characterized their chemical structures by using XPS.

1.3 The research purposes of this thesis

Based on the background reviewed above, the research purposes of this thesis are focused on study of the three inevitable issues, namely $sp^3/(sp^3+sp^2)$ ratio, sp^2 site clustering structure and fabricated defects by NMR techniques, specifically including

their dependences on deposition bias voltage, classifying diverse carbon bonds by various NMR techniques, studying cluster size and its variation with a combined usage of Raman and optical gap characterization, and investigating the distribution of fabricated defects. Additionally in view of engineering application, the tribological performance of studied coating in N_2 atmosphere and ambient air is investigated, and their correlations with the $sp^3/(sp^3+sp^2)$ ratio and sp^2 site nanoclustering structure are also discussed.

Furthermore, the originalities of this thesis mainly lie in the presented inhomogeneous structure model of ion-vapor deposited a-C:H coating, in terms of the preferential coordination of hydrogen atoms with sp^3 C, two distinct types of sp^2 clusters and the partial distribution of fabricated defects in sp^2 C" clusters (see detail in chapter 3~5). Also, we challenged to find out correlations between clustering structure and tribological performance of studied a-C:H coatings, observing inhibitive effect of boundary sp^2 C' sites on the formation of well-lubricant transfer layers in rich of sp^2 C-H bonds in chains (see detail in chapter 6).

Reference

[1] S. Aisenberg, R. Chabot. Ion-beam deposition of thin films of diamondlike carbon. J. Appl. Phys. 42, 2953-2958 (1971)

[2] A. Erdemir, C. Donnet. Tribology of diamond-like carbon films: recent progress and future prospects. J. Phys. D: Appl. Phys. 39, 311-327 (2006)

[3] J. Robertson. Diamond-like amorphous carbon. Mater. Sci. Eng., R. 37, 129-281 (2002)

[4] A. Erdemir. Genesis of superlow friction and wear in diamondlike carbon films. Tribol. Int. 37, 1005-1012 (2004)

[5] A. Erdemir, O. L. Eryilmaz, I. B. Nilufer, G. R. Fenske. Synthesis of superlow-friction carbon films from highly hydrogenated methane plasmas. Surf. Coat. Technol. 133-134, 448-454 (2000)

[6] W. Jacob, W. Moller. On the structure of thin hydrocarbon films. Appl. Phys. Lett.

68, 1771-1773 (1996)

[7] J. Fontaine, C. Donnet, A. Grill, T. Le. Mogne. Tribochemistry between hydrogen and diamond-like carbon films. Surf. Coat. Technol. 146-147, 286-291 (2001)

[8] C. Donnet, J. Fontaine, A. Grill, T. Le. Mogne. The role of hydrogen on the friction mechanism of diamond-like carbon films. Tribol. Lett. 9, 137-142 (2000)

[9] J. Fontaine, J. L. Loubet, T. Le. Mogne, A. Grill. Superlow friction of diamond-like carbon films: a relation to viscoplastic properties. Tribol. Lett. 17, 709-714 (2004)

[10] J. Fontaine, M. Belin, T. Le. Mongne, A. Grill. How to restore superlow friction of DLC: the healing effect of hydrogen gas. Tribol. Int. 37, 869-877 (2004)

[11] Cui Longchen, Lu Zhibin, Wang Liping. Probing the low-friction mechanism of diamond-like carbon by varying of sliding velocity and vacuum pressure. Carbon. 66, 259-266 (2014)

[12] K. Chu Paul, Li. Liuhe. Characterization of amorphous and nanocrystalline carbon films. Mater. Chem. Phys. 96, 253–277 (2006)

[13] A. C. Ferrari, J. Robertson. Interpretation of Raman spectra of disordered and amorphous carbon. Phys. Rev. B. 61, 14095-14107 (2000)

[14] M. A. Tamor, W. C. Vassell. Raman ‘‘fingerprinting’’ of amorphous carbon films. J. Appl. Phys. 76, 3823-3830 (1994)

[15] Craig A. Taylor, Mark F. Wayne, Wilson K. S. Chiu. Residual stress measurement in thin carbon films by Raman spectroscopy and nanoindentation. Thin Solid Films 429, 190–200(2003)

[16] K. W. R. Gilkes, S. Prawer, K. W. Nugent, J. Robertson, H. S. Sands. Direct quantitative detection of the sp^3 bonding in diamond-like carbon films using ultraviolet and visible Raman spectroscopy. J. Appl. Phys. 87, 7283-7289 (2000)

[17] V. I. Merkulov, J. S. Lannin, C. H. Munro, S. A. Asher, V. S. Veerasamy, W. I. Milne. UV studies of tetrahedral bonding in diamondlike amorphous carbon. Phys. Rev. Lett. 78, 4869-4872 (1997)

[18] C. D. Martino, F. Demichelis, A. Tagliaferro. Determination of the sp^3/sp^2 ratio in

a-C:H films by infrared spectrometry analysis. Diam. Rel. Mater., 4, 1210 (1995)

[19] P. I. Rovira, F. Alvarez. Chemical disorder in a-Si:C_x:H for x<0.6. Phys. Rev. B. 55, 4426-4434(1997)

[20] M. A. Tamor, J. A. Haire, C. H. Wu, K. C. Hass. Correlation of the optical gaps and Raman spectra of hydrogenated amorphous carbon films. Appl. Phys. Lett. 54, 123-125 (1989)

[21] J. Choi, K. Ishii, T. Kato, M. Kawaguchi, W. Lee. Structural and mechanical properties of DLC films prepared by bipolar PBII&D. Diam. Rel. Mater. 20, 845–848 (2011)

[22] Jiao Xu, Sadayuki Watanabe, Hideo Hayashi, Masahiro Kawaguchi, Takahisa Kato. Structural characterization of ion-vapor deposited hydrogenated amorphous carbon coatings by solid state ^{13}C nuclear magnetic resonance. J. Appl. Phys. 115, 014303 (2014)

[23] K. W. R. Gilkes, S. Prawer, K. W. Nugent, J. Robertson, H. S. Sands, Y. Lifshitz, X. Shi. Direct quantitative detection of the sp^3 bonding in diamond-like carbon films using ultraviolet and visible Raman spectroscopy. J. Appl. Phys. 87, 7283-7289 (2000)

[24] C. Z. Wang, K. M. Ho. Structure, dynamics, and electronic properties of diamondlike amorphous carbon. Phys. Rev. Lett. 71, 1184–1187 (1993)

[25] C. Donnet, J. Fontaine, F. Lefèbvre, A. Grill, V. Patel, C. Jahnes. Solid state ^{13}C and ^{1}H nuclear magnetic resonance investigations of hydrogenated amorphous carbon. J. Appl. Phys. 85, 3264-3270 (1999)

[26] B. Dischler. Amorphous hydrogenated carbon films, in: P. Koidl, P. Oelhafen (Eds.), EMRS Symp. Proc., Vol. 17, Les Editiones de Physique, Paris, 1987, p. P189

[27] T. Heitz, B. Drévillon, C. Godet, J. E. Bourée. Quantitative study of C-H bonding in polymerlike amorphous carbon films using in situ infrared ellipsometry. Phys. Rev. B. 58,13957–13973(1998)

[28] T. Y. Leung, W. F. Man, P. K. Lim, W. C. Chan, F. Gaspari, S. J. Zukotynski. Determination of the sp^3/sp^2 ratio of a-C:H by XPS and XAES. Non-Cryst. Solids,

254, 156 (1999)

[29] Matthias Ramm, Masafumi Ata, Klaus-Werner Brzezinka, Thomas Gross, Wolfgang Unger. Studies of amorphous carbon using X-ray photoelectron spectroscopy, near-edge X-ray-absorption fine structure and Raman spectroscopy.

[30] C. D. Wagner, W. M. Riggs, L. E. Davis, J. F. Wouler, G. E. Muilenberg (Editor). Handbook of X-ray photoelectron spectroscopy. Perkin-Elmer Corporation, Physical Electron Division, 6509 Flying Cloud Drive. Eden Prairie, Minnesota 55344

[31] Y. Mizokawa, T. Miyasato, S. Nakamura, K. M. Geib, C. W. Wilmse. The C KLL first-derivative X-ray photoelectron spectroscopy spectra as a fingerprint of the carbon state and the characterization of diamondlike carbon films. J. Vac. Sci. Technol. A5, 2809–2813 (1987)

[32] A. Fuchs, J. Scherer, K. Jung, H. Ehrhardt. Determination of sp^2/sp^3 carbon bonding ratio in a-C:H including irradiation damage by factor analysis of Auger electron spectra. Thin Solid Films. 232, 51-55 (1993)

[33] A. C. Ferrari, A. Libassi, B. K. Tanner, V. Stolojan, J. Yuan, L. M. Brown, S. E. Rodil, B. Kleinsorge, J. Robertson. Density, sp^3 fraction, and cross-sectional structure of amorphous carbon films determined by x-ray reflectivity and electron energy-loss spectroscopy. Phys. Rev. B., 62, 11089 (2000)

[34] S. D. Berger, D. R. McKenzie, P. J. Martin. EELS analysis of vacuum arc-deposited diamond-like films. Philos. Mag. Lett. 57,285–290,(1988)

[35] C. Lenardi, P. Piseri, V. Briois, C. E. Bottani, A. Li Bassi. Near-edge x-ray absorption fine structure and Raman characterization of amorphous and nano structured carbon films. J. Appl. Phys. 85, 7159-7167 (1999)

[36] R. Gago, I. Jiménez, J. Neidhardt, B. Abendroth, I. Caretti, L. Hultman, W. Möller. Phys. Rev. B., 71, 125414 (2005)

[37] I. Alexandrou, H. J. Scheibe, C. J. Kiely, A. J. Papworth, G. A. J. Amaratunga, B. Schultrich. Carbon films with an sp2 network structure. Phys. Rev. B 60, 10903–10907 (1999)

[38] H. J. Pan, M. Pruski, B. C. Gerstein. Local coordination of carbon atoms in

amorphous carbon. Phys. Rev. B., 44, 6741 (1992)

[39] K. R. Carduner, M. J. Rokosz, M. A. Tamor, W. C. Vassell. Solid State NMR Study of Carbon Bonding in Amorphous Hydrogenated Carbon Films. Appl. Meg. Res., 2, 647-653 (1991)

[40] M. A. Tamor, W. C. Vassell, K. R. Carduner. Atomic constraint in hydrogenated "diamondlike" carbon. Appl. Phys. Lett., 58, 592 (1991)

[41] C. Donnet, J. Fontaine, F. Lefèbvre, A. Grill, V. Patel, C. Jahnes. Solid state ^{13}C and ^{1}H nuclear magnetic resonance investigations of hydrogenated amorphous carbon. J. Appl. Phys., 85, 3264 (1999)

[42] A. M. Panich. Nuclear Magnetic Resonance Studies of Nanodiamonds. Critical Reviews in Solid State and Materials Sciences. 37, 276 - 303 (2012)

[43] A. M. Panich, G. B. Furman. Nuclear spin-lattice relaxation and paramagnetic defects in carbon nanomaterials. Diam. Rel. Mater. 23, 157-161 (2012)

[44] J. C. C. Freitas, F. G. Emmerich, G. R. C. Cernicchiaro, L. C. Sampaio, T. J. Bonagamba. Magnetic susceptibility effects on ^{13}C MAS NMR spectra of carbon materials and graphite. Solid State Nuclear Magn. Reson., 20, 61 (2001)

[45] H. L. Retcofsky, R. A. Friedel. Carbon-13 magnetic resonance in diamonds, coals and graphite. J. Phys. Chemi., 73, 68-71 (1973)

[46] Y. Maniwa, M. Sato, K. Kume, M. E. Kozlov, M. Tokumoto. Comparative NMR study of new carbon forms. Carbon, 34, 1287-1291 (1996)

[47] A. Dilks, S. Kaplan, A. V. Laeken. A ^{13}C-NMR investigation of plasma polymerized ethane, ethylene, and acetylene. J. Poly. Sci.: Poly. Chem. Edit., 19, 2987 (1981)

[48] R. A. Friedel, H. L. Retcofsky. Carbon-13 Nuclear Magnetic Resonance spectra of olefins and other hydrocarbons. J. Am. Chem. Soc., 85, 1300 (1963)

[49] A. Gangopadhyay. Mechanical and tribological properties of amorphous carbon films. Tribol. Lett. 5, 25–39 (1998)

[50] E. B. D. Bourdon, A. Raveh, S. C. Gujrathi, L. Martinu. Etching of a-C:H films by an atomic oxygen beam. J. Vac. Sci. Technol. 11, 2530- 2535 (1993)

[51] H. X. Li, T. Xu, C. B. Wang. Annealing effect on the structure, mechanical and tribological properties of hydrogenated diamond-like carbon films. Thin Solid Films 515, 2153-2160 (2006)

[52] D. S. Kim, T. E. Fischer, B. Gallois. The effects of oxygen and humidity on friction and wear of diamond-like carbon films. Surf. Coat. Technol. 49, 537-542 (1991)

[53] J. Fontaine, T. Le. Mogne, J. L. Loubet. Achieving superlow friction with hydrogenated amorphous carbon: some key requirements. Thin Solid Films. 482, 99-108 (2005)

[54] A. Erdemir, C. Bindal, J. Pagan, P. Wilbur. Characterization of transfer layers on steel surfaces sliding against diamond-like hydrocarbon films in dry nitrogen. Surf. Coat. Technol. 76-77, 559-563 (1995)

[55] A. Erdemir. Design criteria for superlubricity in carbon films and related microstructures. Tribol. Int. 37, 577-583 (2004)

[56] B. Racine, M. Benlahsen, K. Zellama, M. Zarrabian, J. P. Villain. Hydrogen stability in diamond-like carbon films during wear tests. Appl. Phys. Lett. 75, 3479-3481 (1999)

[57] J. C. Sánchez-López, A. Erdemir, C. Donnet. Friction-induced structural transformations of diamond-like carbon coatings under various atmospheres. Surf. Coat. Technol. 163-164, 444-450 (2003)

[58] Y. Liu, A. Erdemir, E. I. Meletis. An investigation of the relationship between graphitization and frictional behavior of DLC coatings. Surf. Coat. Technol. 86-87, 564-568 (1996)

[59] A. A. Voevodin, A. W. Phelp, J. S. Zabinski, M. S. Donley. Friction induced phase transformation of pulsed laser deposited diamond-like carbon. Diam. .Rel. Mater. 5, 1264-1269 (1996)

[60] T. Le Huu, H. Zaidi, D. Paulmier, P. Voumard. Transformation of sp^3 to sp^2 sites of diamond like carbon coatings during friction in vacuum and under water vapour environment. Thin Solid Films. 290-291, 126-130 (1996)

[61] A. Erdemir. The role of hydrogen in tribological properties of diamond-like carbon films. Surf. Coat. Tech. 146 –147, 292–297 (2001)

[62] L. Pastewka, S. Moser, M. Moseler. Atomistic insights into the running-in, lubrication and failure of hydrogenated diamond-like carbon coatings. Tribol. Lett. 39, 49–61 (2010)

[63] C. Donnet, M. Belin, J. C. Auge, J. M. Martin., A. Grill, P. Patel. Tribochemistry of diamond-like carbon coatings in various environments. Surf. Coat. Technol. 68/69, 626-631 (1994)

[64] K. Jia, Y. Q. Li, T. E. Fischer, B. Gallois. Tribology of diamond-like carbon sliding against itself, silicon nitride, and steel. J. Mater. Res. 10, 1403-1410 (1995)

[65] K. Yuichi, K. Makoto. Influence of exposure to an atmosphere of high relative humidity on tribological properties of diamondlike carbon films. J. Vac. Sci. Technol. A. 7, 2311-2413 (1989)

[66] C. Donnet, T.Le. Mogne, L. Ponsonnet, M. Belin, A. Grill, V. Patel, C. Jahnes. The respective role of oxygen and water vapor on the tribology of hydrogenated diamond-like carbon coatings. Trib. Lett., 4, 259-265 (1998)

[67] J. Andersson, R.A. Erck, A. Erdemir. Friction of diamond-like carbon films in different atmospheres. Wear. 254, 1070–1075 (2003)

[68] J. P. Hirvonen, J. Koskinen, A. Antilla, R. Lappalainen, R. O. Toivanen, E. Arminen and M. Trkula. Characterization and unlubricated sliding of ion-beam-deposited hydrogen-free diamond-like carbon films. Wear. 141,45-58 (1990)

[69] Jiao Xu, Masahiro Kawaguchi, Takahisa Kato. Evolution of Transfer Layers on Steel Balls Sliding against Hydrogenated Amorphous Carbon Coatings in Ambient Air. Tribol. Inter. 70, 42-51 (2014)

[70] A. Erdemir, M. Switala, R. Wei and P. Wilbur. A tribological investigation of the graphite-to-diamond-like behavior of amorphous carbon films ion beam deposited on ceramic substrates. Surf. Coat. Tech. 50, 17-23 (1991)

[71] H. Ronkainen, J. Likonen, J. Koskinen. Tribological properties of hard carbon

films produced by the pulsed vacuum arc discharge method. Surf. Coat. Tech. 54/55, 570-575 (1992)

[72] G. D. Lempert, Y. Lifshitz, S. Rotter, A.J. Armini and S. Bunker. Tribological evaluation of hydrogen-free ion beam deposited diamondlike carbon coatings. Nucl. Inst. Metho. in Phys. Res. Sect. B: Beam interactions with materials and atoms. 80-81, 1502-1506 (1993)

[73] K. Kato, N. Umehara, K. Adachi. Friction, wear and N_2-lubrication of carbon nitride coatings: a review. Wear. 254. 1062–1069 (2003)

[74] T. Tokoroyama, M. Goto, N. Umehara, T. Nakamura, F. Honda. Effect of nitrogen atoms desorption on the friction of the CN_x coating against Si_3N_4 ball in nitrogen gas.

[75] T. Tokoroyama, N. Umehara, H. Tomita, Y. Takanoshita. Effect of Surface Roughness and Transfer Layer of Mating Ceramic Parts for Ultra Low Friction Phenomena in Sliding between CNx and Ceramics. Trans. Jpn Soc. Mech. Eng. C 69, 2824-2829 (2003)

[76] I. L. Singer, S. D. Dvorak, K. J. Wahl, T. W. Scharf. Role of third bodies in friction and wear of protective coatings. J. Vac. Sci. Technol. A. 21, 232-240 (2003)

[77] T. W. Scharf, I. L. Singer. Role of third bodies in friction behavior of diamondlike nanocomposite coatings studied by in situ tribometry. Trib. Trans. 45, 363-371 (2002)

[78] T. W. Scharf, I. L. Singer. Monitoring transfer films and friction instabilities with in situ Raman tribometry. Trib. Lett. 14, 3-8 (2003)

[79] T. W. Scharf, I. L. Singer. Quantification of the thickness of carbon transfer films using Raman tribometry. Trib. Lett. 14, 137-145 (2003)

[80] C. Donnet, A. Erdemir. Tribology of Diamond-Like Carbon Films: Fundamentals and Applications. Springer; 2007, p. 201-236.

[81] T. W. Scharf, I. L. Singer. Role of the transfer film on the friction and wear of metal carbide reinforced amorphous carbon coatings during run-in. Tribol. Lett. 36, 43-53 (2009)

2 Basic principles of solid state ^{13}C NMR characterization and its experiments

2.1 Basics of solid state ^{13}C NMR

For 1/2 nuclei such as ^{13}C and ^{1}H spinning in a uniform external magnetic field B_0, two quantized spin states can be established, i.e. +1/2 and -1/2, which represents the low and high spin energy state, respectively. Accordingly, the magnetic moment μ of low energy state +1/2 is positively aligned with the external field B_0, while μ of the high energy -1/2 spin state is opposed to the direction of B_0. As the population of nuclei in these two energy states follows Boltzmann distribution with a Boltzmann factor as $e^{(-Ei/KT)}$ in which K is the Boltzmann constant and T is the abstract temperature, the number of nuclei at low energy state is higher than that of the high energy state. As a result, one net nuclear magnetization M_0 will be established aligned with the positive direction of B_0, as shown in Fig. 2.1a and Fig. 2.1b, and

$$M_0 = \sum \mu_i = \frac{N\gamma^2\hbar^2 I(I+1)B_0}{3KT} \qquad (2.1)$$

where μ_i is the magnetic moment of i th nucleus, N the number of nuclei, $\hbar$ the Planck constant, I the spin quantum number. Each μ_i is determined by the nuclear spin I_i *as* $\mu_i=\gamma I_i$ where γ is the magnetogyric ratio, a constant for a given type of nucleus.

In static magnetic field, the nuclear moment precesses around B_0 at *Larmor frequency* ω_0, and

$$\omega_0 = \gamma B_0 \qquad (2.2)$$

In the acquisition of NMR spectra, by applying a radiofrequency (r.f.) wave B_1 along x axis which fulfills the *Bohr condition* $\Delta E=h\nu=\gamma hB_0/2\pi$, the transitions between spin quantized states can be affected and captured spectroscopically. From the perspective of electromagnetism, applying B_1 along x axis excites the nuclei at low energy state to -1/2 state, so that the net nuclei magnetization M_0 will deflect toward x-y plane (see in

Fig. 2.1c). After the irradiation by B_1, the excited spins will relax to its equilibrium state +1/2, so that the deflected nuclei magnetization M_0 will recovery to z direction, and during this relaxation process, the recovering magnetization *M(t)* may cut the magnetic inductive line of detective coils and generate inductive current.

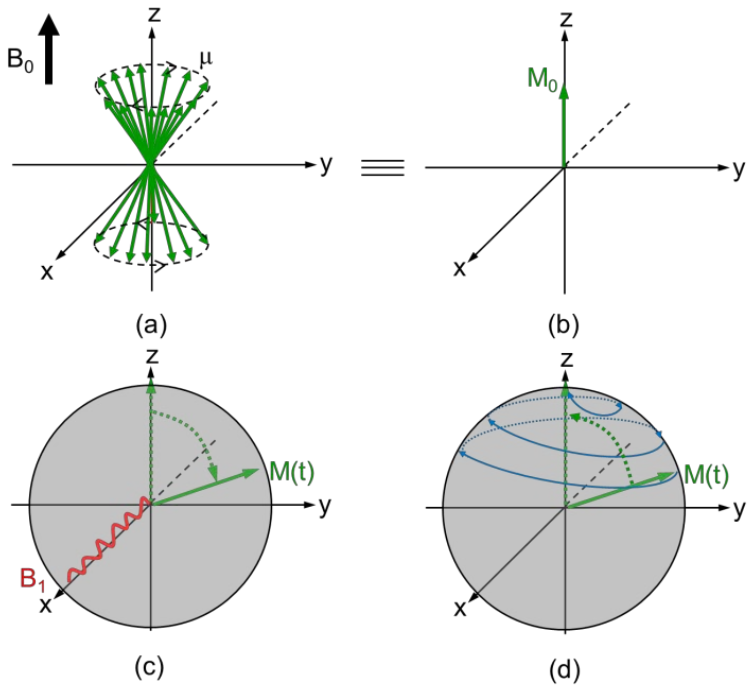

Fig. 2.1 The schematic illustration of the formation of net nuclear magnetization and the effect of r.f. waves B_1 on nutation.

The mechanism of NMR characterization is clearly demonstrated in the equation of total Hamiltonian (Eq.(2.3)) [1, 2] that for spin 1/2 nuclei, the measured resonance frequencies are not only dominated by Zeeman interaction (H_z) between observed nuclei and B_0, but also the various types of local interactions which can reflect the local chemical environment of given nuclei and spectroscopically display it in the domain of frequency as separated peaks. Also, the peak intensity is linear to the populations of nuclei in the same bonding structure.

$$H_{tot} = H_z + H_{d.\mathrm{homo}} + H_{d.heter} + H_{cs} + H_{rf}(t) + R(t) \quad (2.3)$$

where H_Z is the Zeeman, $H_{d,homo}$ the local interaction between observed nuclei and local magnetic field generated by neighboring homo-nuclei, $H_{d,heter}$ the local

interaction between observed nuclei and local magnetic field generated by neighboring hetero-nuclei, H_{CS} the local interaction between observed nuclei and local magnetic field generated by neighboring bonded electrons (i.e., chemical shift interaction), $H_{rf}(t)$ the experimentally controlled Hamiltonian produced by r.f. irradiation, $R(t)$ the coupling of studied nuclei to local fluctuating magnetic fields derived from paramagnetic impurity centers, primarily from unpaired electrons which shields a few fraction of neighboring nuclei from observation and also broadens the bandwidth of NMR spectra due to electron-nuclei interactions.

NMR characterization is inherently quantitative since the intensity of net magnetization M_0 is strongly related to the population of active spins. By using controllable radiofrequency waves, more sophisticated information on bonding structures of a-C:H coatings can be obtained. However, in practice anisotropic broadening usually occurs in solid state ^{13}C NMR spectra due to the chemical shielding, dipolar interaction, spin-spin couplings and magnetic susceptibility, which greatly restrains the resolution of NMR spectrum. Only simplifying the H_{tot} by using special geometrical sample manipulations or radiofrequency pulses can we focus attention on one specific type of interaction [1, 2]. For example, the Zeeman interaction can be eliminated from Eq.(2.3) by changing the reference frame to a rotating frame at the resonance frequency of observed nuclei. By comparison, other terms in Eq. (2.3) are in the order of perturbations of Zeeman term, and can be selectively suppressed by the controllable item H_{rf}(t). For a-C:H coatings with nature abundance of ^{13}C nuclei (1.1 at.%), the homonuclear dipolar coupling between ^{13}C nuclei is too weak because of its low population and large inter-nuclear distance, whereas the heteronuclear dipolar coupling between ^{13}C and ^{1}H nuclei is dominant and largely responsible for the line broadening of solid state NMR spectra due to the distinct hybridization phases sp^1, sp^2 and sp^3 of carbon atoms and various $CH_{(0\leqslant n\leqslant 3)}$ bonding configurations.

To improve the resolution of NMR spectra, a significantly important technique known as magic-angle-spinning (MAS) [3] was proposed in 1953 to eliminate the

broadening effects of chemical shift anisotropy Δ_{CS} which is larger than spinning frequency and thus narrow the peaks. This technique typically requires the sample spins rapidly in a cylindrical rotor around a spinning axis oriented at the magic angle 54.74° with respect to the static magnetic field B_0, as shown in Fig. 2.2.

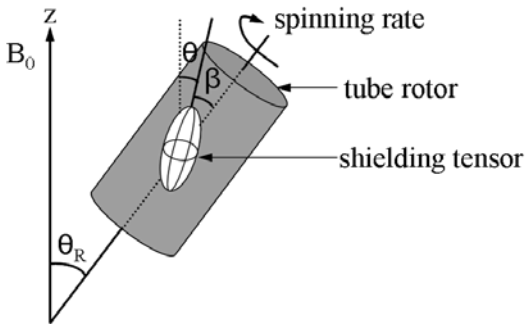

Figure 2.2 The schematic illustration of magic-angle spinning technique. The solid fragments spin rapidly in a cylindrical tube rotor about a spinning axis oriented at the magic angle (θ_R=54.74°) with respect to the applied magnetic field B_0. Magic-angle spinning removes the effects of chemical shielding anisotropy and heteronuclear dipolar coupling. The chemical shielding tensor is represented here by an ellipsoid; it is fixed in the molecule to which it applies and so rotates with the sample. The angle θ is the angle between B_0 and the principal *z*-axis of the shielding tensor; β is the angle between the *z*-axis of the shielding tensor principal axis frame and the spinning axis.

2.2 High-power ^{1}H decoupled single pulse

When we observe a dilute nucleus like ^{13}C with 1.1% abundance and ^{15}N with 0.365% abundance with ^{1}H or other abundant nucleus nearby, high-power ^{1}H decoupled single pulse is an important technique to remove the broadening effects of ^{1}H-^{13}C heteronuclear coupling and improve resolution of NMR spectra. As shown in Fig. 2.3 and Fig. 2.4, high-power ^{1}H decoupled single pulse starts from a 90° single pulse at the frequency of ^{13}C resonance which deflects the net magnetization of ^{13}C to the axis of *y* around *x* axis, and at this moment *t* is defined as zero, at which the component magnitude of $M_C(t)$ along *y* axis is equal to its initial value established merely under the effect of static magnetic field B_0. During the magnetization

relaxation process, the component magnitude of $M_C(t)$ along each axis is acquired with a continuous decoupling of ^1H spins interactions, as described by Eq. (2.4)

$$M_x = M_0 \sin\theta_0 \sin\omega_0 t \exp(-t/T_2) \qquad (2.4a)$$

$$M_y = M_0 \sin\theta_0 \cos\omega_0 t \exp(-t/T_2) \qquad (2.4b)$$

$$M_z = M_0[1-(1-\cos\theta_0)\exp(-t/T_1)] \qquad (2.4c)$$

where ω_0 is the precession frequency of ^{13}C along z axis from $y \rightarrow x \rightarrow -y \rightarrow -x \rightarrow y$, θ_0 the pulse angle initially as 90°, T_2 the spin-spin relaxation time standing for the decaying time constant of transverse magnetization, and T_1 the spin-lattice relaxation time standing for the establishing time constant of longitudinal magnetization.

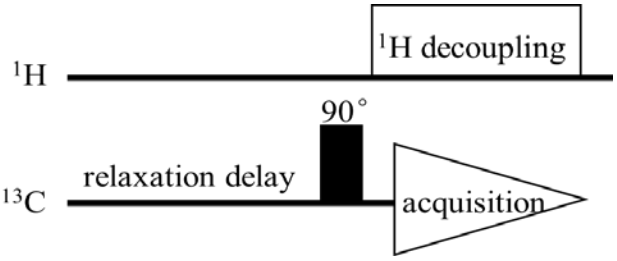

Fig. 2.3 The pulse sequence diagram of high-power ^1H dipolar decoupled single pulse sequence.

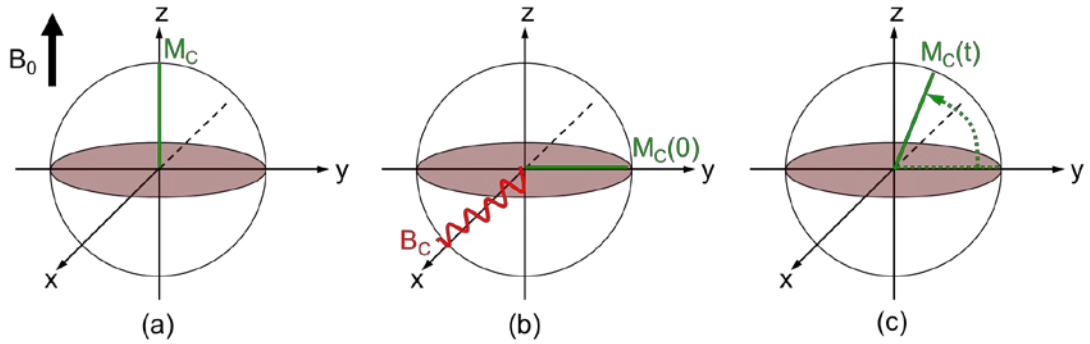

Fig. 2.4 The schematic illustration on magnetization transverse of high-power ^1H dipolar decoupled single pulse sequence.

Thus, precession is an inevitable free transverse of magnetization along z axis, while deflection (i.e. nutation) is a forced transverse of magnetization along x axis. The mechanism of ^1H decoupling is applying a continuous high-power irradiation

(100~1000 watts) at the resonance frequency of ^{1}H spins which make the magnetization of ^{1}H spins fully excited and stay at its saturation state.

The original signal acquired in detecting coils is a free induction decaying (FID) signal in domain of time, consisting of various ^{13}C resonance frequencies which cannot be directly used for chemical structure analysis. In order to learn about ^{13}C spins in different chemical environments, a Fourier transformation of FID signal is needed which transforms it into the domain of frequency as given in Eq. (2.5), containing the information on magnetization magnitude M_0 and resonant frequency ω_0 together. As FT transformation is a linear operation, the FT transformation of superposed signals in time domain is equal to the summation of each FT transformed signal, so that all the resonant frequency can be recognized at the same weight factor.

$$M_0 \sin\theta_0 \cos(\omega_0 t)\exp(-t/T_2) \xrightarrow{FFT} \frac{M_0 \sin\theta_0 / T_2}{(1/T_2)^2 + (\omega - \omega_0)^2} \qquad (2.5)$$

However, as the spin resonant frequency is closely dependent on local chemical environment but varies slightly in magnitude order of 10^{-6} of ω_0, a standard sample is required to define the zero position of chemical shift. Generally, we choose tetramethylsilane (TMS) because of its chemical equivalent structure of four carbon atoms, and thus the chemical structure of resonance spins can be characterized by the chemical shift from zero and the detected peaks as defined by Eq. (2.6)

$$\delta = \frac{\omega_0 - \omega_{TMS}}{\omega_{TMS}} \times 10^6 \qquad (2.6)$$

2.3 High-power decoupled ^{1}H-^{13}C cross polarization

Cross polarization (CP) is a spectral editing technique mediated by the heteronuclear dipolar interactions between ^{1}H and dilute spins like ^{13}C and ^{15}N. The use of ^{1}H-^{13}C CP-MAS can improve the signal/noise ratio of ^{13}C spectra and greatly shorten the relaxation time of ^{13}C nuclei between acquisition scans. The following is a schematic explanation on the main features of CPMAS sequence, as shown in Fig. 2.5 and Fig. 2.6.

It is based on a doubly rotating frame: one of them is a rotating frame of ^{1}H spins (x'-y-z') in which all the magnetic fields due to ^{1}H pulses are static, while the other one is a rotating frame of ^{13}C spins (x-y-z) in which all the magnetic fields due to ^{13}C pulses are static. At the beginning, a 90° single pulse at ^{1}H resonance frequency is applied along x axis of laboratory frame which deflects the ^{1}H magnetization to y axis along x axis of laboratory frame. And then, the magnetic field B_H known as spin-lock field is dephased to y' axis of rotating frame to maintain the ^{1}H magnetization in y' axis. At this moment, B_H acts as the only magnetic field in the rotating frame of ^{1}H spins in the same way as B_0 applied in laboratory frame which establish the equilibrium ^{1}H magnetization without radiofrequency waves. Meanwhile, the contact

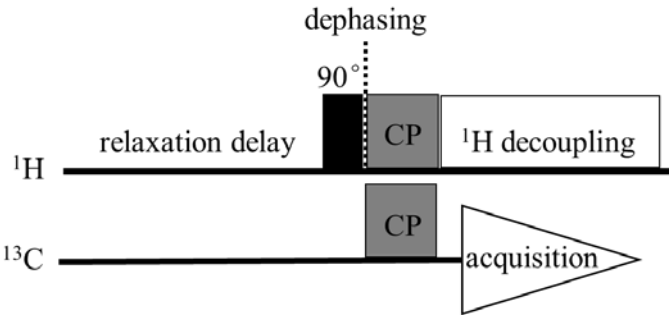

Fig. 2.5 The pulse sequence diagram of ^{1}H-^{13}C CPMAS.

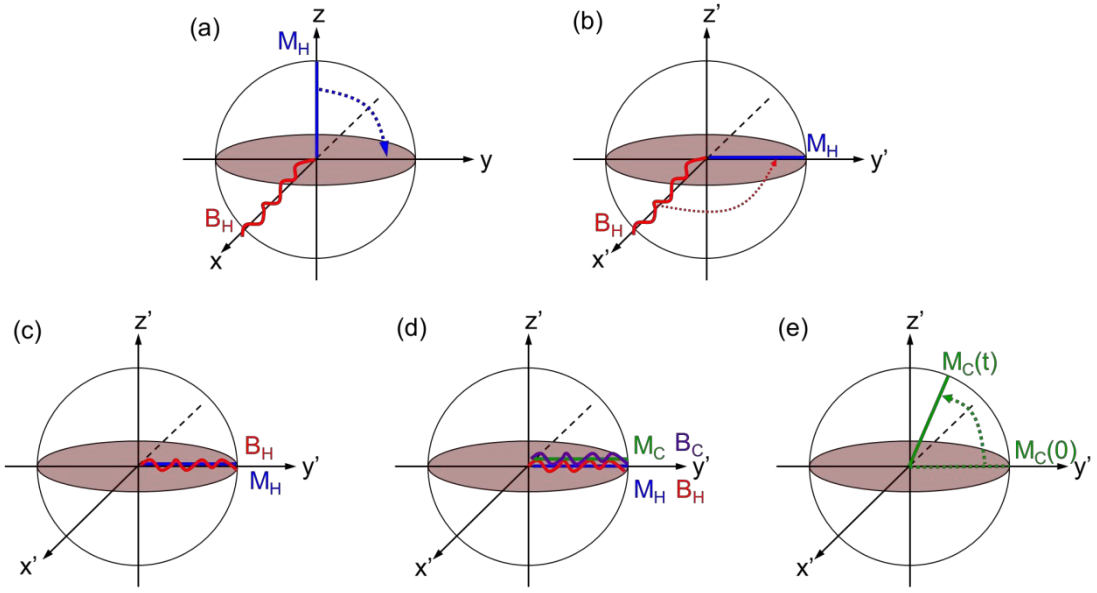

Fig. 2.6 The schematic illustration on magnetization transverse of ^{1}H-^{13}C CPMAS pulse sequence.

pulse B_C is applied to ^{13}C spins along *y'* axis of rotating frame at the frequency of ^{13}C resonance, and the amplitude of two contact pulses have to be carefully set to achieve the *Hartmann-Hahn* matching condition Eq.(2.7)

$$\gamma_H B_H = \gamma_C B_C \qquad (2.7)$$

which sets the spin states energy gap of ^{1}H and ^{13}C spins in rotating frame as equal, so that a transition requiring energy of ^{1}H spins can be compensated by a transition energy releasing from ^{13}C spins. Such a dipolar coupling between ^{1}H and ^{13}C spins introduces a re-distribution of energy to maintain the total energy of spin system as a constant. At last, FID signal of ^{13}C spins is acquired with ^{1}H decoupling technique, which is same as the single pulse decoupling sequence introduced in Sec. 2.2.

At very short contact time, the initial polarization transfer to ^{13}C spins is from the most closet ^{1}H spins. As the contact time increases, the polarization transition from other nearby ^{1}H spins will be enhanced. However, as the spin-lock magnetic field is too weak to maintain the initial ^{1}H magnetization, there will be a theoretical maximum signal of ^{13}C spins, and the dynamic cross polarization from excited ^{1}H spins to ^{13}C is described by Eq. (2.8) [3, 4]:

$$\frac{S(t)}{S(0)} = \left(\frac{1}{1-T_{CP}/T_{1\rho}}\right)\left[1-\exp\left(\frac{\left(1-T_{CP}/T_{1\rho}\right)}{T_{CP}}t\right)\exp\left(-\frac{t}{T_{1\rho}}\right)\right] \qquad (2.8)$$

in which *S(t)* is the signal intensity at time *t*, *S(0)* the theoretical maximum signal, T_{CP} a time constant describing cross-polarization transfer, $T_{1\rho}$ the spin-lock relaxation time.

2.4 Spin-lattice relaxation time measurement by saturation recovery sequence

Spin lattice relaxation is an energy exchange process between individual nuclear spins and external "lattice" which acts as an energy sink of spin system to establish and restore the net magnetization to its equilibrium value along *z* axis. For a-C:H coatings with nature abundance of ^{13}C nuclei and no molecular rotation, the spin-lattice relaxation of ^{13}C spins is strongly dominated by heteronuclear dipolar-dipolar (DD) interactions, sometimes with a combination of electron-nuclear

interactions associated with fabricated defects (will be discussed in Chap. 5). In fact, dipolar-dipolar interaction arises from a total magnetic field composed of the static magnetic field B_0 and local magnetic fields generated by nearby spins. The strength and direction of local magnetic fields are determined by the inter-nuclear distance and their orientation to B_0.

In the measurement of spin-lattice relaxation time (T_1) by modern NMR instrument, the component magnetization is recorded in domain of time as described in Eq. (2.4), and then transformed to domain of frequency. The most frequently used sequence for T_1 measurement include saturation recovery sequence and inversion recovery sequence. The former one is applicable for nuclear spins with long T_1 and the relaxation delay between acquisition scans only need 1 s, while the latter one can achieve a higher accuracy of T_1 determination with a compromise of experiment time, because it needs $5T_1$ at least for the full relaxation of magnetization before the next repetition of acquisition scans [5-8].

From the prospective of saving experiment time, we choose saturation recovery method in this study and its sequences for ^{1}H and ^{13}C spins are illustrated in Fig. 2.7 and Fig. 2.8, respectively. Saturation sequence is started from one set of 90° single pulses with a gradually shortened interval from T_1 (roughly estimated) to 1% or 1‰ of T_1. This set of saturation sequence continuously deflects the growing longitudinal magnetization of observed nuclei to transverse plane and disperse it in *x*-*y* plane due to the non-uniformity of static field B_0. Because of the shortening interval between 90° pulses, the magnitude of longitudinal magnetization gradually decreases to zero and finally achieves the saturation state of spin system. In following, there is a relaxation interval (denoted as τ) between saturation sequence and the last 90° pulse, which should be set reasonably for accurate measurement of T_1. .Generally, we set τ/T_1 as {0.01, 0.1, 0.2, 0.35, 0.5, 0.9, 1.2, 1.6, 2.3, 5} successively, so that the data of magnetization magnitude can distribute uniformly in its graph as a function of τ.

In some cases, cross-polarization technique is also applied between the last 90° single pulse and acquisition pulse in saturation-recovery experiment of ^{13}C, as shown

in Fig. 2.9, to selectively investigate the recovery behavior of protonated or proton-proximate carbons [5, 6].

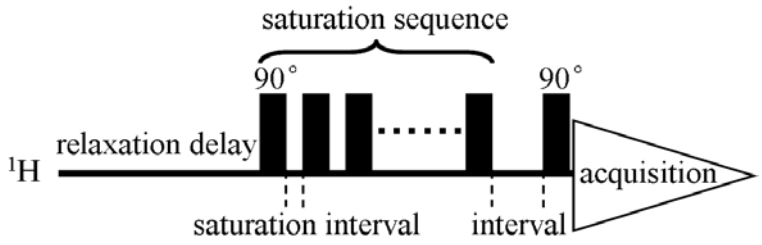

Fig. 2.7 The pulse sequence diagram of ^{1}H saturation recovery.

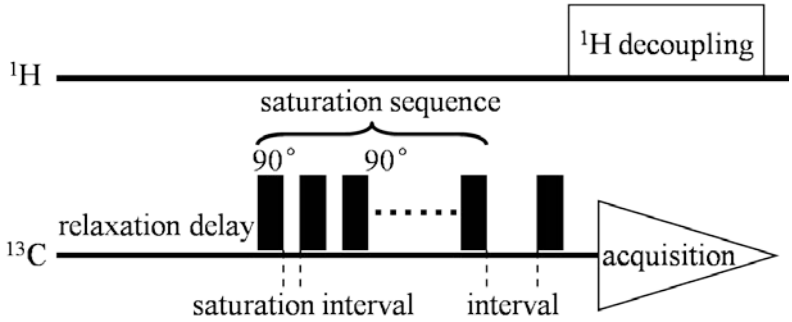

Fig. 2.8 The pulse sequence diagram of high-power ^{1}H dipolar decoupled ^{13}C saturation recovery.

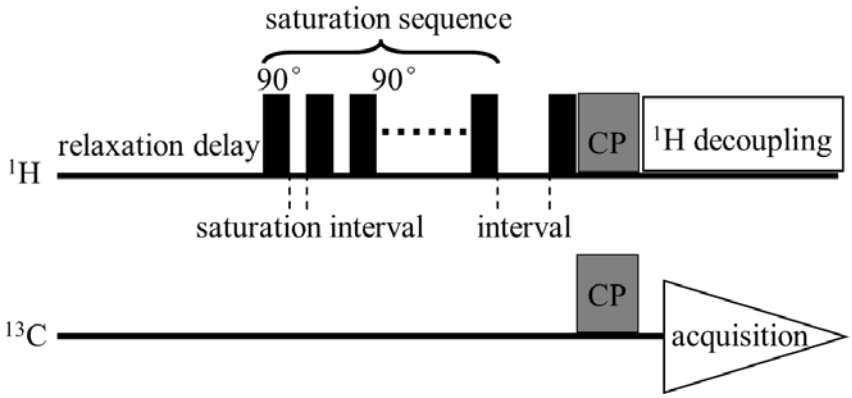

Fig. 2.9 The pulse sequence diagram of interrupted high-power ^{1}H dipolar decoupled ^{13}C saturation recovery with CPMAS technique.

References

[1] Hellmut Eckert. Solid state NMR as a tool of structure and dynamics in solid state chemistry and materials science: recent progress and challenges. Current Opinion in Solid State and Materials Science.1, 466-476 (1996)

[2] K. M. McNamara, K. K. Gleason, D. J. Vestyck, J. E. Butler. Evaluation of diamond films by nuclear magnetic resonance and Raman spectroscopy. Diam. Rel. Mater. 1, 1145-1155 (1992)

[3] M. J. Duer. Solid-State NMR Spectroscopy Principles and Applications. Cambridge: Blackwell Science Ltd, 2002, p. 73-103

[4] G. C. Levy, R. L. Lichter, G. L. Nelson. Carbon-13 Nuclear Magnetic Resonance Spectroscopy. Second Edition. Florida: Krieger Publishing Company, 1993, 211-245

[5] C. Jäger, J. J. Titman, R. J. Newport. Detection of structural heterogeneity in amorphous-C:H films by NMR. Thin Solid Films. 227, 3-6 (1993)

[6] C. Jäger, J. Gottwald, H. W. Spiess, R. J. Newport. Structural properties of amorphous hydrogenated carbon. III. NMR investigation. Phys. Rev. B. 50, 846-852 (1994)

[7] K. R. Carduner, M. J. Rokosz, M. A. Tamor, W. C. Vassell. Solid state NMR study of carbon bonding in amorphous hydrogenated carbon films. Appl. Meg. Res., 2, 647-653 (1991)

[8] C. Donnet, J. Fontaine, F. Lefèbvre, A. Grill, V. Patel, C. Jahnes. Solid state ^{13}C and ^{1}H nuclear magnetic resonance investigation of hydrogenated amorphous carbon. J. Appl. Phys., 85, 3264-3270 (1999)

3 Fragment sample preparation for solid state ^{13}C NMR experiments

3.1 Introduction

As regard to the structure characterization of artificially synthesized carbon materials by solid state NMR, small amount of pioneering research work had been carried out in 1990s [1-5]. In 1992, McNamara and Gleason [1, 2] measured natural diamond powder and chemical-vapor-deposited (CVD) diamond films by applying static single pulse. Polycrystalline diamond films were produced by hot-filament reactor using acetone as the carbon source. Si substrates were seeded with 0.25 pm natural diamond particles and the film thickness was controlled as 5~10 μm. In their static single pulse experiments, diamond films were sliced by a diamond saw together with silicon substrates into 4×9 mm slivers, and then directly inserted into NMR coil. As the carbon source acetone was labeled with ^{13}C at methyl site with an overall gas-phase enrichment of 22%, a narrow sp^3 C peak was perfectly observed at 36±2 ppm relative to tetramethylsilane (TMS) in ^{13}C spectra, even without the use of magic-angle spinning (MAS) technique. Same results were reported by H. Lock [3, 4], except that the Si substrates were removed by dissolving in aqueous HNO_3/HF solution, and the resulted diamond fragments were cleaned thoroughly in distilled water. A similar sample preparation process was reported by S. Hayashi and F. Hoshi et al. [5]. In their NMR investigation of ^{13}C-enriched single-wall carbon nanotubes prepared by catalytic decomposition of CH_4, raw products were dissolved in 3 mol/L HNO_3 aqueous solution, and the resulted fragments were filtered and dried in ambient air.

Specifically in field of amorphous carbon coatings, Pan et al. [6] studied r.f. sputtered a-C coatings grown on Cu substrates by ^{13}C MAS technique, and observed two broad peaks centered at 130 ppm and 62 ppm which were attributed to sp^2 and sp^3 C, respectively. Cu substrates were removed by dissolving in HCl aqueous solution and the resulted a-C fragments were cleaned thoroughly in distilled water for NMR

experiments. Similar spectra were observed by Demichelis [7] for r.f.-sputtered a-C coatings on Al foils which were dissolved in dilute HCl aqueous solution.

By comparison, one simpler sample preparation was presented by Glozan et al. [8] for ta-C coatings grown by filtered cathode arc deposition. The ta-C fragments were collected from fused silica substrates which could be easily removed due to the large residual stress in ta-C coatings. Similarly, Carduner et al. [9] deposited a-C:H coatings by r.f.-biased parallel-plate reactor on glass substrates. Deposition was lasted until the coatings peeled off from glass substrates due to their intrinsic compressive stress and turned into fine fragments.

No matter what kind of fragment preparation methods is adopted, there is a basic principle that the chemical structure of bulk materials can be perfectly represented by fragment specimens, yet, with a compromise of morphological change. In this chapter, we discussed this significant issue seriously by using Raman spectroscopy and ERDA.

3.2 Experimental details

3.2.1 a-C:H coating grown by ion-vapor deposition

In this thesis, a-C:H coatings were grown on Si (100) wafers and iron sheets at 200℃ by a ion-vapor deposition system as illustrated in Fig. 3.1. Carbon source toluene (C_7H_8) with natural abundance of ^{13}C (1.1 at.%) was ionized by a hot filament and the resulted ionized species bombarded toward negative-pulse biased substrates for 3 hours, which allowed a coating thickness about 1 μm. A base pressure less than 3×10^{-3} Pa was achieved in vacuum chamber before deposition, and the working pressure in vacuum chamber was controlled as 0.1 Pa. The composition of resulted ionized species were detected by a quadruple mass spectroscopy, as shown in Fig. 3.2. Due to the low ionization efficiency of hot-filament decomposition method, the fragmentation degree of C_7H_8 was quite low, so that in the resulted ionized vapor, there was a larger content of $C_7H_7^+$ and other species such as $C_8H_{10}^+$, $C_5H_9^+$, $C_3H_3^+$, $C_2H_4^+$, CH^+, C^+, H_2 and H^+.

The bonding structure of studied coatings were effectively controlled by the

substrate bias voltage as 0.5 kV, 1.0 kV, 1.5 kV, 2.0 kV, 2.5 kV, 3.0 kV, 3.5 kV at a frequency of 1 kHz and a pulse duty of 25%, and correspondingly the coatings were referred to as B0.5, B1.0 etc., as listed in Tab. 3.1 with their hydrogen content. The hydrogen content was determined by high-resolution elastic recoil detection analysis (Kobelco, HRBS 1000) with a probe beam of 0.5 MeV N^+ incident on the coating surface at an angle of 67.5° with respect to the surface normal. In order to improve the adhesion between carbon coatings and iron substrates, an a-C:H:Si interlayer as thick as 10 nm was firstly deposited under a bias voltage of 1.5 kV using tetramethylsilane (TMS) as the carbon source.

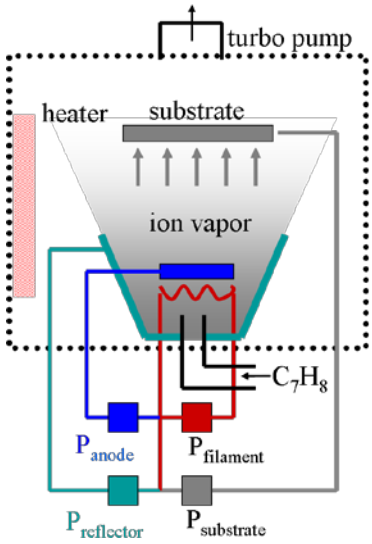

Figure 3.1 The schematic illustration of ion-vapor deposition system.

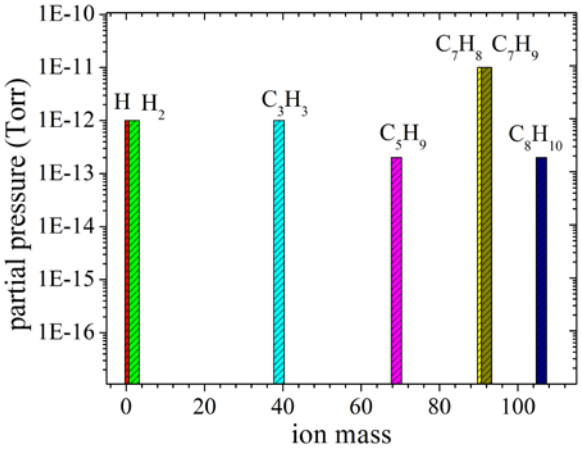

Figure 3.2 The components of ion vapor when the deposition bias voltage was 1.5 KV.

Meanwhile, the morphology of studied coating on silicon wafer and iron sheet was observed by scanning electron microscope (SEM), as described in Fig. 3.3. Compared

with the polished silicon wafer, the top surface of iron sheet is rough, so that the roughness of a-C:H coating deposited on iron sheet is also high.

Table 3.1 The substrate bias voltage and hydrogen content of studied a-C:H coatings.

Deposited coatings	Bias voltage (kV)	Hydrogen content (at.%)
B0.5	0.5	35
B1.0	1.0	32
B1.5	1.5	22
B2.0	2.0	20
B2.5	2.5	19
B3.0	3.0	18
B3.5	3.5	17

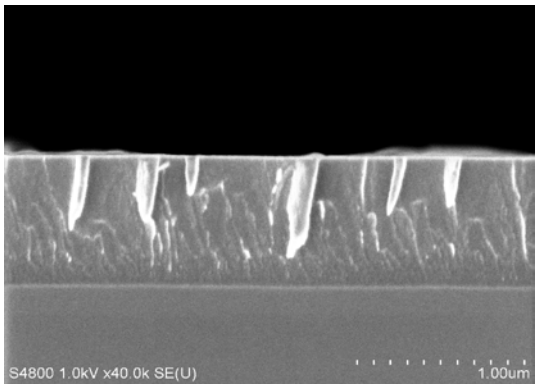

(a) B1.5 coated on Si(100) wafer

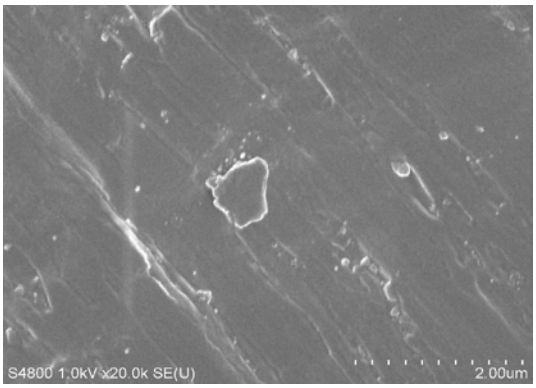

(b) uncoated steel sheet

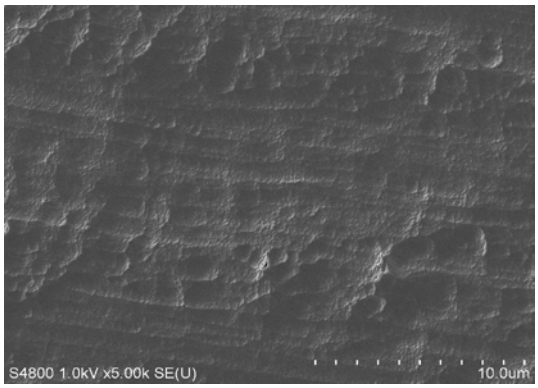

(c) B1.5 coated on steel sheet

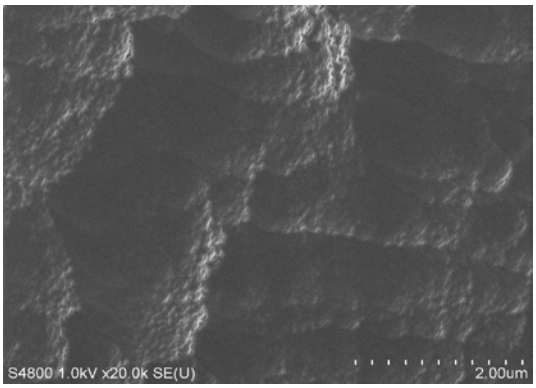

(d) B1.5 coated on steel sheet

Figure 3.3 The SEM observation of ion-vapor deposited coatings on silicon wafer and

iron sheets when the bias voltage was 1.5 kV. (a) is a cross-sectional observation, while (b)~(d) are top-view observations.

3.2.2 Dissolution process of as-deposited a-C:H coating

Due to the potential annealing effects of 200℃ deposition temperature for long time in this ion-vapor deposition system, as well as the comparatively lower residual stress in resulted coatings, the metal-substrate dissolution process described in Ref. [6] was adopted in this thesis for sample preparation of solid state NMR experiments, as illustrated in Fig. 3.4 step by step. Coating-covered iron sheets were immerged into 6 mol/L HCl solutions at 60℃ until all the iron sheets were dissolved. Next, the a-C:H

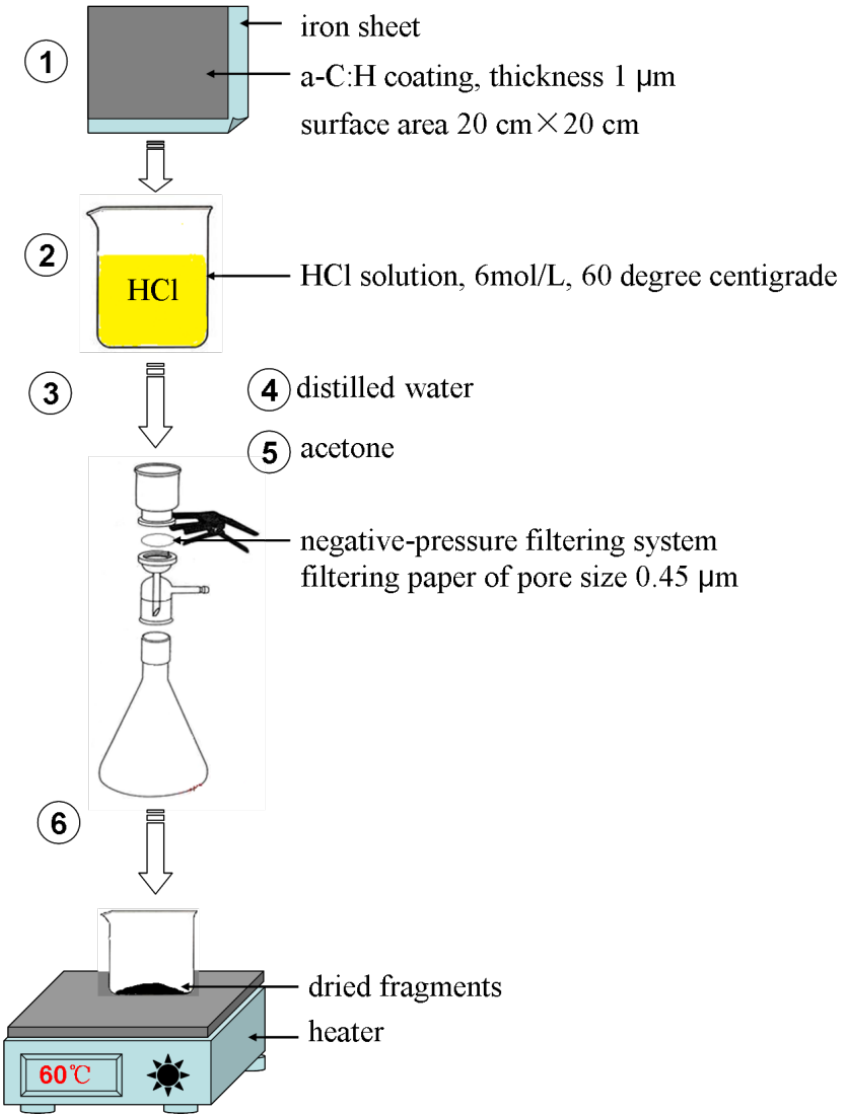

Figure 3.4 The schematic illustration of fragment preparation process for solid state NMR experiments.

fragments were filtered through a negative-pressure filtering system using a layer of filtering paper with a pore size of 0.45 μm, then thoroughly cleaned by distilled water and acetone successively, and finally dried in ambient air at 60℃. An XPS characterization of well-prepared fragments showed that the remained content of iron atoms in fragments were generally below 0.1 at.%, which has negligible effects on the uniformity of static magnetic field B_0 and the balance of rotating sample tubes.

3.3 Results and discussions

3.3.1 Optical spectroscopic observation of a-C:H fragment

At first, well-prepared a-C:H fragments were observed by optical microscope, as shown in Fig. 3.5. Because of the rough surface of iron substrates, the surface of a-C:H fragments was also rough and showed no dependence on substrate bias voltage.

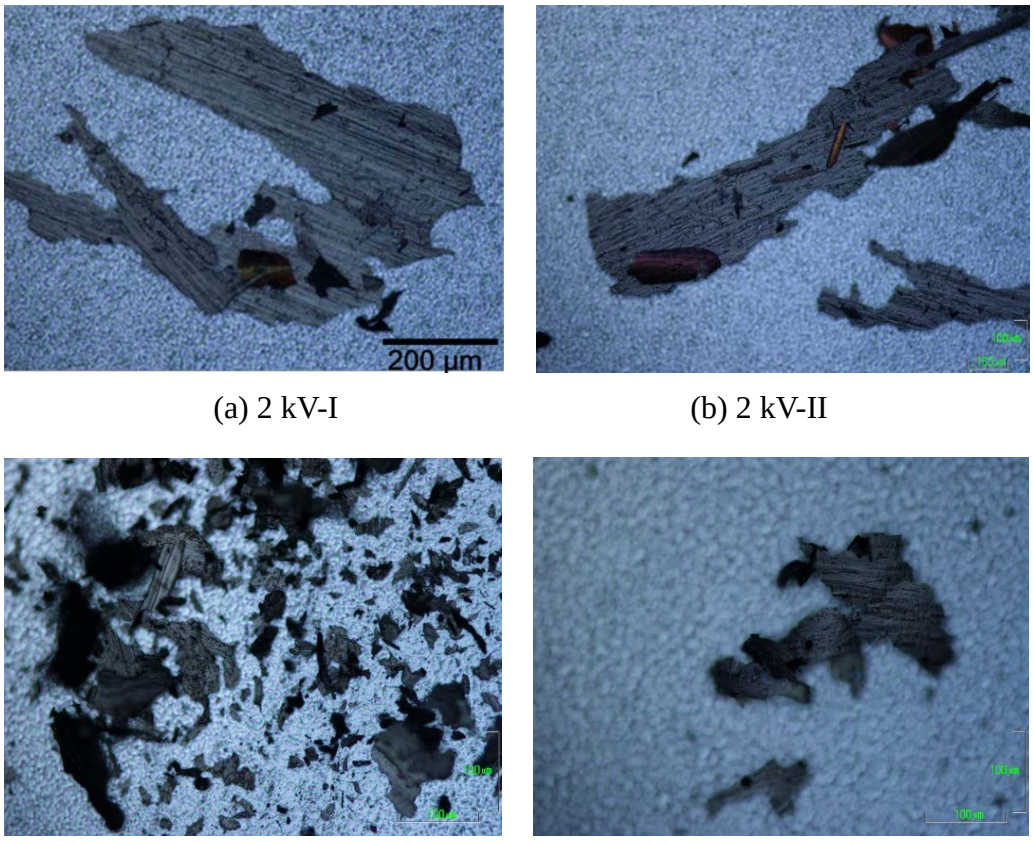

(a) 2 kV-I (b) 2 kV-II

(c) 3.5 kV (d) 4 kV

Figure 3.5 Optical microscopy observation of dried a-C:H fragments derived from coatings deposited under various bias voltages.

3.3.2 Chemical inertness of a-C:H fragment in HCl aqueous solution

In order to confirm the chemical inertness of studied coatings, both the as-deposited coatings and well-prepared fragments were characterized by visible Raman spectroscopy with 0.5 mW laser power of 532-nm wavelength (doubling-Nd-YAG). Due to the rough surface of as-deposited coating on iron sheet and well-prepared fragments, the diameter of laser spot was reduced less than 10 μm to focus on rough surface during acquisitions well.

Additional, considering the potential effects of HCl solution concentrations and dissolution durations on fragment property, other two groups of tests were set, as listed in Tab. 3.2. In each condition, one slice of a-C:H coated Si wafer was placed into HCl solutions with the other slice of un-coated iron sheet, and both of them were in the same surface area of 5×5 cm^2.

Table 3.2 The two groups of aqueous conditions for the dissolution of B2.5 coating.

Group I		Group II	
HCl concentration (mol/L)	Dissolution duration (minute)	HCl concentration (mol/L)	Dissolution duration (minute)
2	700	6	5
4	270	6	60
6	20	6	180
8	15	6	360
10	10		
12	5		

All the comparative Raman spectra are displayed in Fig. 3.6 and Fig. 3.7. Firstly, Fig. 3.6 compares the baseline-calibrated Raman spectra of a-C:H coatings and fragments prepared under 0.5, 2.0 and 3.5 kV bias voltage. The spectra deviation between these two types of samples was in the order of experimental error, which suggests a notable chemical inertness of studied a-C:H coatings in acid solutions. Such a negligible deviation was possible caused by the release of chemical bonding in

the interface between as-grown coating and iron substrate. Secondly, as regard to the two groups of comparative experiments (as described in Fig. 3.7), we found that all the spectra could be divided into two groups which were identical to that of the two as-deposited coatings (denoted as 1 and 2), yet, in no obvious dependence on aqueous conditions. In despite of this, it is clear that these two groups of Raman spectra exhibit the same peak position and line shape, while their difference only relies on the peak intensity which is merely caused by the deviation of coating thickness of tested slices.

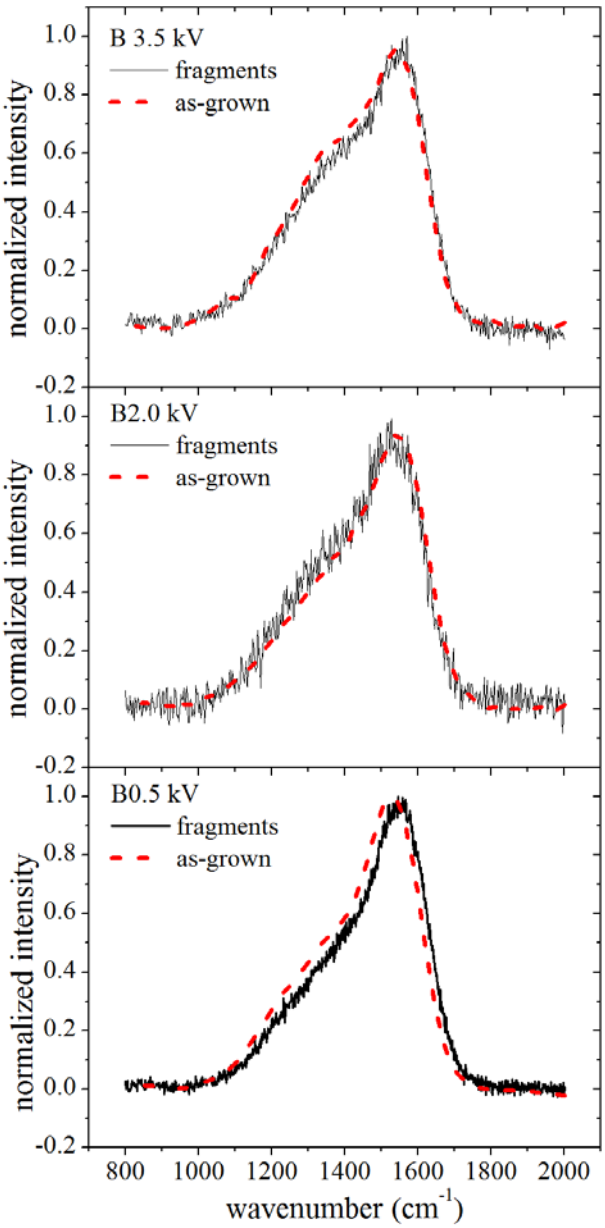

Figure 3.6 The comparison of Raman spectra between as-deposited coatings and resulting fragments prepared in HCl solution with the same concentration of H^+ ions.

It is noted that this hot filament deposition system cannot provide samples with good thickness uniformity in large area. The ion density near the center of ion gun is higher than that of border region, so that the coating in center position parallel to ion gun is slightly thicker than coating in border areas. The tested slices of a-C:H coatings were cut apart from one specimen but in two different regions, so that all the spectra were divided into two groups but showed no dependence on aqueous conditions. However, it is believable that the chemical structure of bulk materials is perfectly maintained during this acid dissolution process.

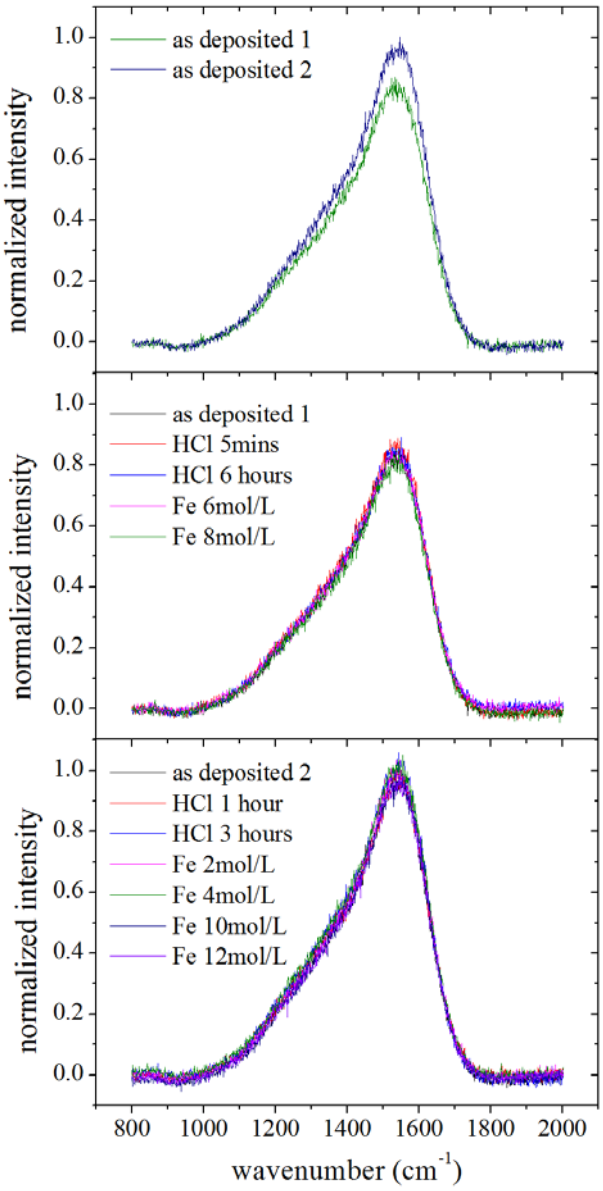

Figure 3.7 The comparison of Raman spectra between as-deposited coatings and processed coatings prepared in HCl solution with various concentration of H^+ ions.

Fig. 3.8 shows a well-understood structural transformation of a-C:H coatings with an increase of ion energy [10, 11], from polymer-like carbon (PLC) to diamond-like carbon (DLC) as bias voltage was below 2 kV and then further to graphite-like carbon (GLC) as the bias voltage grew up to 3.5 kV. In the whole range of bias voltage within 0.5~3.5 kV, the G-peak position shifted continuously up to higher wavenumber from 1540 cm^{-1} to 1560 cm^{-1}, and the peak area ratio *I(D)/I(G)* grew from 1.3 to 2.1. These tendencies are widely known to be related to the decrease of hydrogen content

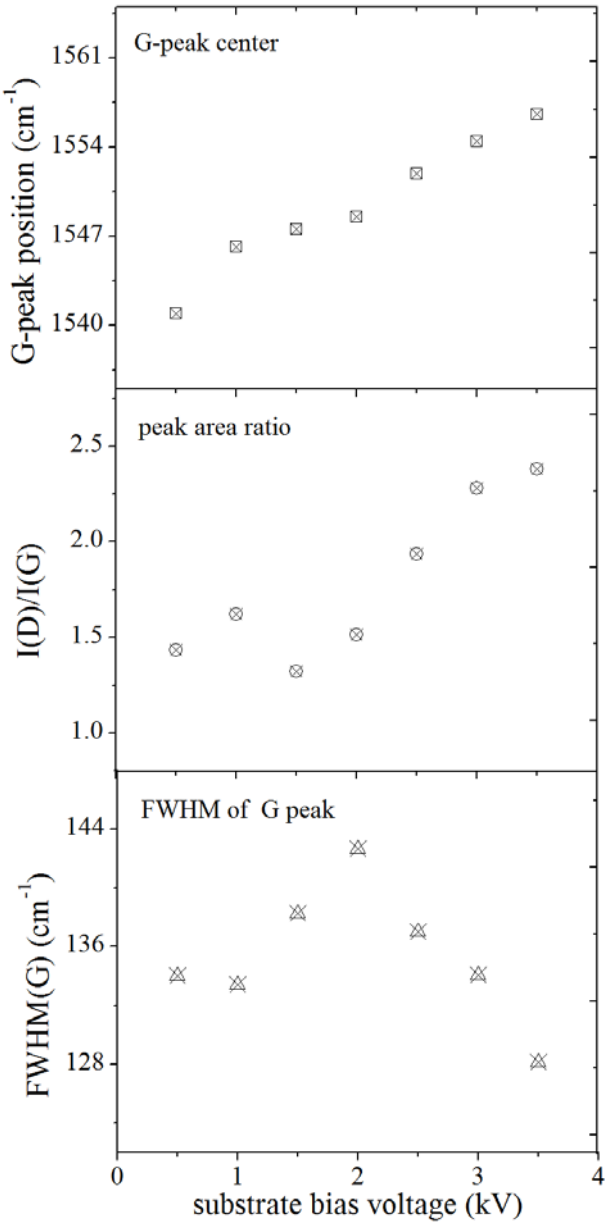

Figure 3.8 Raman parameters of B0.5~B3.5 fragments calculated from double Gaussian fitted of G and D peak as the function of substrate bias voltage.

and the increase of sp^2 C in aromatic ring. As the G-peak position is below 1550 cm^{-1}, i.e. bias voltage within 0.5~2.0 kV, the *FWHM(G)* grew upwards from 132 cm^{-1} to its maximum value of 144 cm^{-1} due to the diamond-like structure and disordering of carbon network, including bond-angle and bond-length distortion. In the high wavenumber region of G-peak position above 1550 cm^{-1}, i.e., bias voltage within 2.0~3.5 kV, the *FWHM(G)* reduced from its maximum to 128 cm^{-1} for the significant increase of graphite-like sp^2 clusters.

3.3.3 Stability of hydrogen in a-C:H fragment during dissolution process

In addition to Raman characterization, another important issue in following work is the stability of hydrogen atoms during this acidic dissolution process. As mentioned in Chapter 2 that in a-C:H coatings with natural abundance of ^{13}C, the relaxation behavior of ^{13}C spins is mainly dependent on ^{1}H-^{13}C heteronuclear interactions, so that the content of hydrogen in well-prepared fragments is an important factor in following analysis. Some reports [12, 13] deduced that in a-C:H(:Si) coatings, there are some free hydrogen molecules trapped in holes of amorphous carbon network and may be diffused due to thermal energy or break of local framework [12-15]. Thus, we measured the hydrogen content of acid-treated slices of a-C:H coatings (the same ones tested in Sec. 3.3.2) by using high-resolution ERDA. In Fig. 3.9, the hydrogen content depth within 60 nm of acid-treated a-C:H coatings are compared with that of the second as-deposited a-C:H coating (cut apart from the center area of specimen as described in Sec. 3.3.2) in depth direction, and in Fig. 3.10 the average hydrogen content calculated within 60~300 Angstrom depth are compared. Interestingly, it was found that almost for all the acid-treated samples, their hydrogen content was lower than that of as-deposited coating by 2~5 at.% in detection depth direction, which suggested that there is a few loss of hydrogen molecular during fragment preparation. Fortunately, such a few loss of trapped hydrogen molecular has limited impacts on the dominant heteronuclear interactions between bonded ^{13}C and ^{1}H spins and can be reasonably neglected.

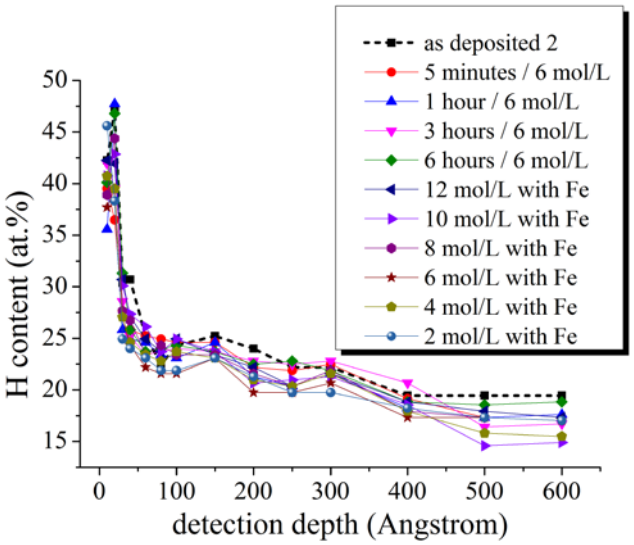

Figure 3.9 The hydrogen concentration of a-C:H coatings as a function of detection

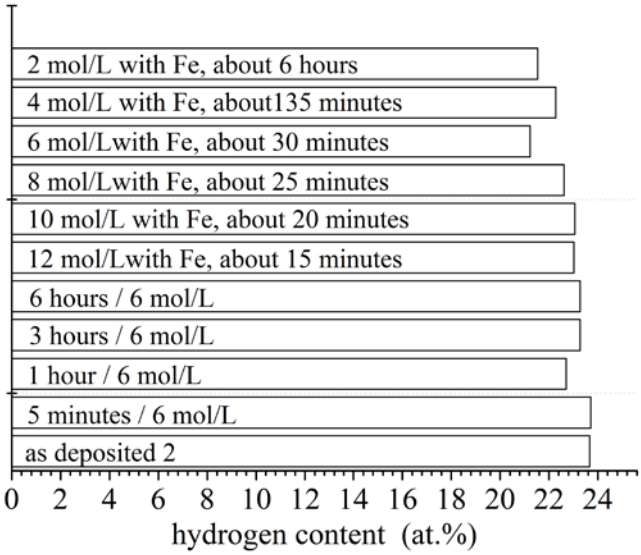

Figure 3.10 The average hydrogen concentration of a-C:H coatings within 6~30 nm in the direction of detection depth.

3.4 Conclusions

In this chapter, a-C:H fragments were prepared by dissolving iron substrates in HCl aqueous solutions, and the chemical inertness of the well-prepared a-C:H fragments were checked by using Raman spectroscopy and ERDA. According to the Raman characterization of as-deposited coating and acid-treated fragments under various aqueous conditions, it is confirmed that no detectable change of chemical structure occurred during this dissolution process, and the bonding structure of bulk coating

material can be well represented by the a-C:H fragments. On the other hand, the ERDA experiments showed that there was a slight loss of hydrogen content in a-C:H fragments which is possibly associated with a diffusion of trapped hydrogen molecular during dissolution process. However, such a few loss of hydrogen molecular has limited impacts on the dominant heteronuclear interactions between bonded ^{13}C and ^{1}H spins and thus can be reasonably neglected.

References

[1] K. M. McNamara, K. K. Gleason, D. J. Vestyck, J. E. Butler. Evaluation of diamond films by nuclear magnetic resonance and Raman spectroscopy. Diam. Rel. Mater. 1, 1145-1155 (1992)

[2] K. M. McNamara, K. K. Gleason. Selectively ^{13}C-enriched diamond films studied by nuclear magnetic resonance. J. .Appl. Phys. 71, 2884-2889 (1992)

[3] H. Lock, R. A. Wind, G. E. Maciel, C. E. Johnson. A study of ^{13}C-enriched chemical vapor deposited diamond film by means of ^{13}C nuclear magnetic resonance, electron paramagnetic resonance, and dynamic nuclear polarization. J. Chem. Phys. 99, 3363-3373 (1993)

[4] H. Lock, G. E. Maciel, C. E. Johnson. Natural-abundance ^{13}C dynamic nuclear polarization experiments on chemical vapor deposited diamond film. J. Mater. Res., 7, 2791-2797 (1992)

[6] Hongjun Pan, M. Pruski, B. C. Gerstein. Local coordination of carbon atoms in amorphous carbon. Phys. Rev. B. 44, 6741-6745 (1991)

[7] F. Demichelis, C. F. Pirri, A. Tagliaferro. Determination of sp^3/sp^2 ratio in diamond-like films of a-C:H. Diam. Rel. Mater. 1, 298-300 (1992)

[8] M. M. Golzan, P. B. Lukins, D. R. McKenzie, A. M. Vassallo, J. V. Hanna. NMR evidence for strained carbon bonding in tetrahedral amorphous carbon. Chem. Phys. 193, 167-172 (1995)

[9] K. R. Carduner, M. J. Rokosz, M. A. Tamor, W. C.Vassell. Solid State NMR study of carbon bonding in amorphous hydrogenated carbon films. Appl. Magn .Reson. 2, 647-653 (1991)

[10] J. Robertson. Diamond-like amorphous carbon. Mater. Sci. Eng., R. 37, 129-281 (2002)

[11] A. C. Ferrari, J. Robertson. Interpretation of Raman spectra of disordered and amorphous carbon. Phys. Rev. B. 61, 14095-14107 (2000)

[12] A. Erdemir. Genesis of superlow friction and wear in diamondlike carbon films. Tribol. Int. 37, 1005-1012 (2004)

[13] J. Fontaine, C. Donnet, A. Grill, T. Le. Mogne. Tribochemistry between hydrogen and diamond-like carbon films. Surf. Coat. Technol. 146-147, 286-291 (2001)

[14] J. Fontaine, M. Belin, T. Le. Mongne, A. Grill. How to restore superlow friction of DLC: the healing effect of hydrogen gas. Tribol. Int. 37, 869-877 (2004)

[15] J. Fontaine, T. Le. Mogne, J. L. Loubet. Achieving superlow friction with hydrogenated amorphous carbon: some key requirements. Thin Solid Films. 482, 99-108 (2005)

4 $sp^3/(sp^3+sp^2)$ ratio of a-C:H coating determined by solid state ^{13}C NMR

4.1 Introduction

As we mentioned above that to understand the wide range of properties of a-C:H coatings, basically there are three inevitable issues while evaluating the amount of sp^2 C and sp^3 C would be the first indispensable issue in recent study of a-C:H coatings. Numerous researches have demonstrated that the ratio of $sp^3/(sp^3+sp^2)$ plays a significant role in the mechanical [1-6], optical [7-9], electrical [6, 8, 10] and tribological [11, 12] properties of amorphous carbon coatings. For example, Tab. 4.1 concludes the widely-concerned properties of amorphous carbon coatings in comparison with diamond, graphite, C_{60} and polyethylene [1, 2]. Specifically compared with diamond and polymers, the hardness of a-C(:H) coatings is proportional to the fraction of sp^3 C-C bonds rather than the total amount of sp^3 C, since the presence of sp^3 $CH_{n(1\leqslant n\leqslant 3)}$ in chain-like structure may reduce the rigidity of amorphous carbon network. This argument has also been presented in the reports of Cho [3], Tamor and Carduner et al. [4, 5] by applying CPMAS and interrupted decoupling techniques to distinguish and quantify various types of carbon bonds in a-C:H coatings.

As regard to the effects of $sp^3/(sp^3+sp^2)$ ratio on tribology performance of a-C(:H) coatings, an earlier MD simulation of Gao and Mikulski et al. [11, 12] using Brenner's second-generation REBO potential [13] revealed that tribochemical reactions were both dependent on the $sp^3/(sp^3+sp^2)$ ratio and the degree of hydrogen-passivation on contact surfaces. In their study [11], a-C:H coatings with a similar $sp^3/(sp^3+sp^2)$ ratio were sheared against a hydrogen-terminated diamond surface under an average load of 300 nN. The results showed a remove of hydrogen atoms from counterface as the sliding movement started, and a dramatic bonding rearrangement and adhesion between tribopairs occurred due to the increased number of potential reaction sites. Also, the higher degree of hydrogen termination of diamond surface, the lower friction response were observed. Besides, the a-C:H coating with highest sp^3 fraction and least content of C-H bonding showed highest friction force when it was sheared against a hydrogen-free diamond tip or a rough amorphous tip due to potential

reactions of unsaturated carbons on counterface.

In this chapter, $sp^3/(sp^3+sp^2)$ ratio of ion-vapor deposited coatings was measured by applying ^{13}C MAS and CPMAS techniques, and their effects on the mechanical properties of studied coatings is also investigated. The ^{13}C MAS technique aims to detect all the bonded ^{13}C nuclei, while the CPMAS specifically focuses on ^{13}C nuclei hydrogenated or at least proximate to hydrogen atoms.

Table 4.1 Comparison of major properties of amorphous carbons with those of reference materials [1, 2].

	sp^3 fraction (at.%)	hydrogen fraction (at.%)	density (g/cm^3)	optical gap (eV)	hardness (GPa)
diamond	100	0	3.515	5.5	100
graphite	0	0	2.267	0	/
C_{60}	0	0	/	/	/
sputtered a-C	5	0	2.2	0.5	<18
ta-C	80~88	0	3.1	2.5	80
ta-C:H	70	30	2.4	2.0~2.5	50
a-C:H (hard)	40	30~40	1.6~2.2	1.1~1.7	10~20
a-C:H (soft)	60	40~50	1.2~1.6	1.7~4	<10
polyethylene	100	67	0.92	6	0.01

4.2 Experimental details

4.2.1 Mechanical property characterization of as-deposited coating

The hardness and Young's modulus of as-deposited coatings on Si substrate were measured by an Elionix ENT-2100 nanoindentation system. 1000 μN load was applied lineally on a well-profiled Berkovich pyramid diamond indenter (edge angle 115°, inclination angle 65.03°, tip defect ~10 nm) in 500 steps at a loading speed of 0.1 mN/sec. The maximum load was kept for 1000 msec and induced full plasticity on tested spots, and then unloaded at the same speed of 0.1 mN/sec. The elastic modulus of studied coatings E_S was determined by the equation [14~16]:

$$\frac{1}{E^*}=\frac{1-\nu_S{}^2}{E_S}+\frac{1-\nu_I{}^2}{E_I} \qquad (4.1)$$

in which

$$E^* = \frac{S\sqrt{\pi}}{2\sqrt{A}} \tag{4.2}$$

$$A(h_A) = 3\sqrt{3}\tan^2 65.03^\circ h_A^2 \tag{4.3}$$

$$h_A = h_{\max} - 0.75 F_{\max}/S \tag{4.4}$$

where E^* is the reduced elastic modulus, E_I the elastic modulus of diamond indenter, v_S and v_I the Poisson's ratio of tested coating and diamond indenter respectively, S the experimentally measured stiffness of upper portion of unloading curve equals to $|dF/dh|_{Fmax}$, A the projected area of elastic contact, h_{max} the maximum deformation at peak load, h_A the calibrated elastic deformation considering tip defect [16], F_{max} the peak load, as illustrated by Fig. 4.1. More than 30 points were tested on each coating for average evaluation. The indentation depth was generally 4~7 % of coating thickness to eliminate the deformation effects of silicon substrate.

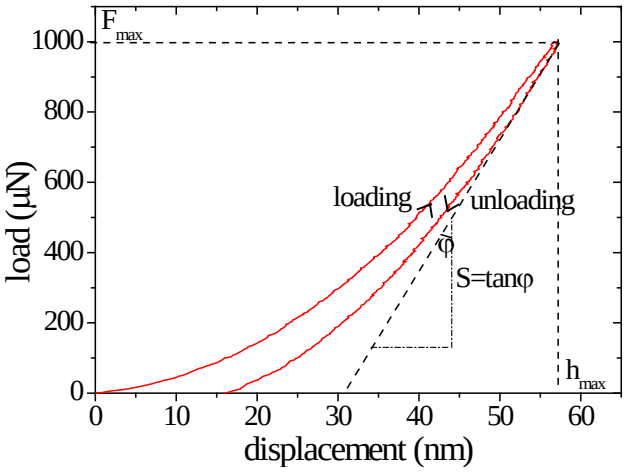

Figure 4.1 An example of load-displacement curve of nanoindentation experiments of studied a-C:H coatings.

Meanwhile, the residual stress was also determined based on the Stoney's equation [17, 18]:

$$\sigma = \frac{E_S D^2}{6dR(1-\nu_S)} \tag{4.5}$$

in which E_S is the Young's modulus of Si substrate, D the thickness of Si substrate, d the thickness of coating, v_s the Poisson's ratio of coating and R the curvature of coated Si substrates (in a square size of 25×5 mm^2) and can be approximately obtained by Eq. 4.6:

$$R \cong \frac{l^2}{8\delta} \qquad (4.6)$$

in which l is the length of Si substrate, δ the distance illustrated in Fig. 4.2 which was measured after deposition by a microstylus surface profilometer (Kosaka Laboratory Ltd., Surfcorder SE-30D).

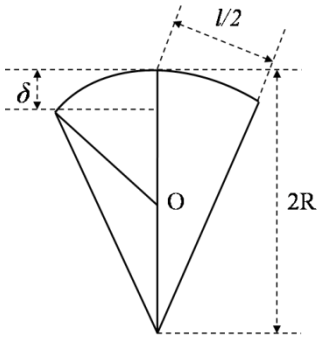

Figure 4.2 The approximate solution of the curvature of coated Si substrate by using microstylus surface profilometer.

4.2.2 ^{13}C MAS and ^{13}C CPMAS experiments

In high-resolution solid state NMR experiments, 10~15 mg dried fragments were uniformly packed into ZrO_2 tube rotor in diameter of 2.2 mm and length of 13 mm. Scanning number were varied within 20000~40000 from sample masses for expected *S/N* ratio of ^{13}C spectra. All the spectra were recorded by a JEOL ECA-600 spectrometer operating at 600 MHz for ^{1}H nuclei and 150 MHz for ^{13}C nuclei, using a standard double-resonance probe-head equipped with MAS facility allowing spinning frequency up to 22 kHz, and DEPTH2 sequence was applied to eliminate background signal. At first, ^{13}C MAS spectra of pristine C60 powder with 99.9 % pureness was tested to confirm that this NMR device and testing parameters were set appropriately. Figure 4.3 displays the obtained spectra which is well consistent with other previous reports [19].

To quantify $sp^3/(sp^3+sp^2)$ ratio of studied a-C:H coatings, high-power ^{1}H-decoupled single pulse sequence with MAS technique (illustrated in Fig. 2.3 and Fig. 2.4) was applied with 90° single pulse length of 2.2 μs and a relaxation delay of $5T_1$(C). Spinning frequency was controlled within 20~22 kHz to eliminate the spinning sidebands at utmost extent. In ^{1}H-decoupled ^{13}C MAS tests, all the ^{13}C nuclei except for those affected by paramagnetic impurities could be detected, while in ^{13}C MAS without ^{1}H-decoupling tests, only the non-protonated carbons remote from hydrogen

spins could be detected. Moreover, ^1H-decoupled cross polarization sequence with MAS technique (illustrated in Fig. 2.6 and Fig. 2.7) was applied with 90° single pulse length of 2.2 μs and a relaxation delay of 1 s. As the contact time increased from 0.1 ms to 20 ms, detectable peaks began to appear from 0.2 ms, indicating that the spin-locking relaxation time of ^1H and ^{13}C in rotating frame (i.e. $T_{1\rho}$) was approximately 0.1 ms. Thus, the CPMAS spectra obtained with 0.2 ms contact time were mainly derived from protonated carbons, while the spectra with moderate contact time but maximum peak intensity presented a maximum combined information of protonated carbon and proton-proximate carbons.

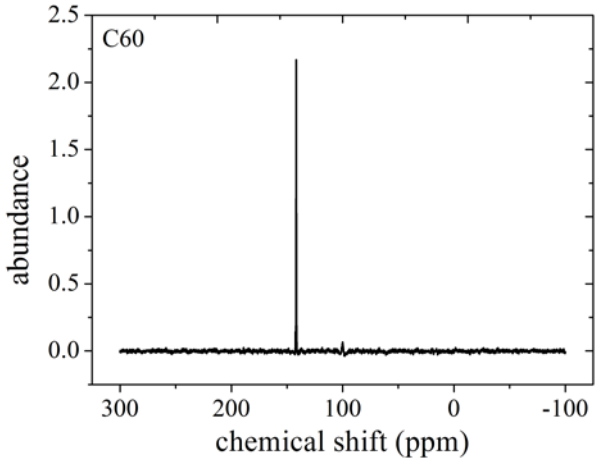

Figure 4.3 The ^{13}C MAS spectra of pristine C_{60} fragment.

Additionally, XPS C1s spectra of dried fragments were acquired by a PHI Quantera II system which used monochromatic Al (Kα) X-ray radiation with photon energy of 25 kV as the light source at a square area of 100×100 μm^2. The testing chamber was vacuumed less than 1.0×10^{-6} Pa. XPS spectra were collected by an analyzer with pass energy of 280 eV for surface composition survey spectra. The atomic content of each element was evaluated in terms of the area intensity under composition survey spectra, as displayed in Fig. 4.4. Detected fragments were firstly compressed onto a indium (elemental symbol: In) tablet, and then pasted on the sample stage of XPS device. Since the fragments exposed in open air can easily be contaminated by atmosphere air, a pre-sputtering cleaning was done for 1 minutes by applying a Ar^+ beam of 4 keV before XPS measurement. A XPS survey spectra of chemical composition showed that the atomic content of Fe atoms remained in dried fragments were below 0.1 at.%, representing its negligible effect on the magnetic field homogeneity of external static field B_0. The content of indium comes from the special tablet for the measurement of

powder specimens.

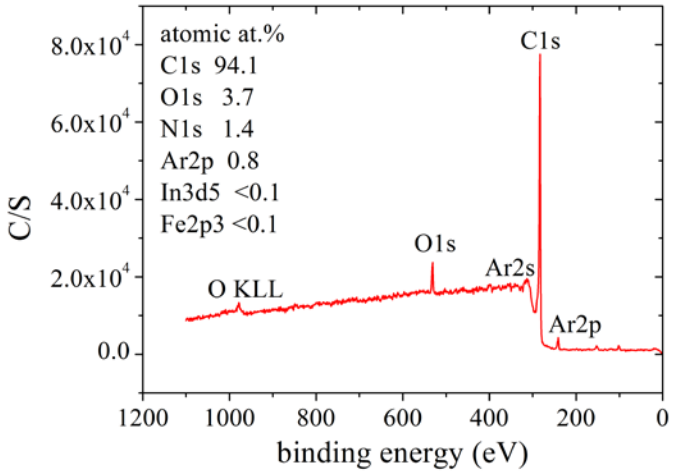

Figure 4.4 The surface composition survey spectra of B1.5 a-C:H fragment.

4.3 Results and discussions

4.3.1 $sp^3/(sp^3+sp^2)$ ratio determined by ^{13}C MAS

Technically, as the broadening effects of heteronuclear dipolar coupling and chemical shift anisotropy (CSA) were largely suppressed by MAS technique, all the ^{13}C nuclei except for those nearby paramagnetic impurities could be detected in ^{1}H-decoupled ^{13}C MAS measurements. Fig. 4.5 shows the ^{13}C MAS spectra of studied coatings, in which two isotropic peaks centered around 50 ppm and 137 ppm are attributed to sp^3 C and sp^2 C, respectively. Because of the disordering of bonding structure and distortion, the bandwidth of these two peaks reached to 4.5~7.5 kHz. Noticeably distinct from previous reports of a-C:H coatings [3-5], a shoulder peak (denoted as sp^2 C′ in this thesis) centering around 105 ppm was observed ppm in each spectra, which quite resembled the ^{13}C MAS spectra of nanodiamonds in particle size of 4~5 nm with a chemically-unlike shell at the outside surface [20]. The fraction of sp^2 C′ sites increased to its maximum value at 2 kV and then gradually decreased with further increase of substrate bias voltage to 3.5 kV. Clearly, the generation of sp^2 C′ sites are highly affected by the ion energy during deposition and thus associated with the nanoclustering of sp^2 C sites.

The $sp^3/(sp^3+sp^2)$ ratio was determined from Gaussian deconvolution analysis of ^{13}C MAS spectra in terms of peak area intensity, as shown in Fig. 4.6 and Fig. 4.7, together with the mechanical properties of studied coatings. Consistent with previous study of PECVD-deposited a-C:H coating [3-5], the mechanical properties of ion-vapor deposited a-C:H coating are not rigidly dependent on the total amount of sp^3 C:

while the hardness and residual stress of studied coatings reached the highest value at 2 kV and then gradually reduced with further increase of bias voltage, the content of sp^3 C decreased continuously in the whole range of 0.5~3.5 kV from 25 at.% to 13 at.%. Similarly, in ion-vapor deposited a-C:H coating, the mechanical properties of thin coatings were mainly determined by the content of diamond-like cross-linked sp^3 C rather than the total content of sp^3 C [3-5].

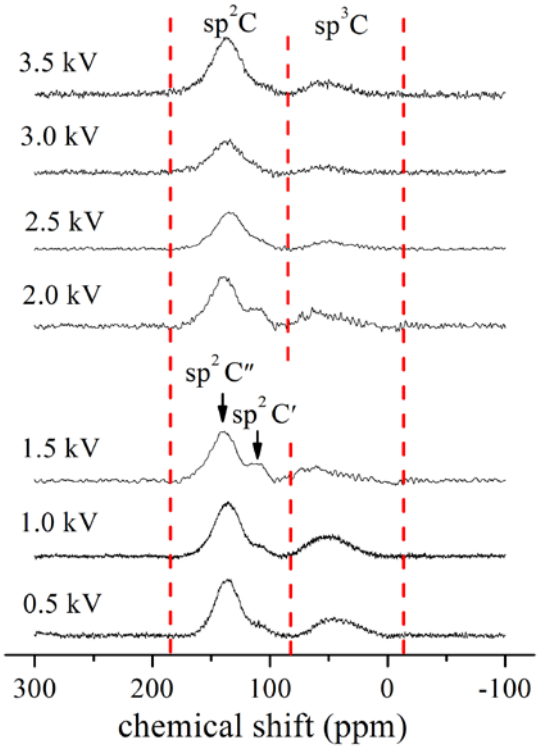

Figure 4.5 ^{13}C MAS spectra of B0.5~B3.5 fragments as the function of substrate bias voltage.

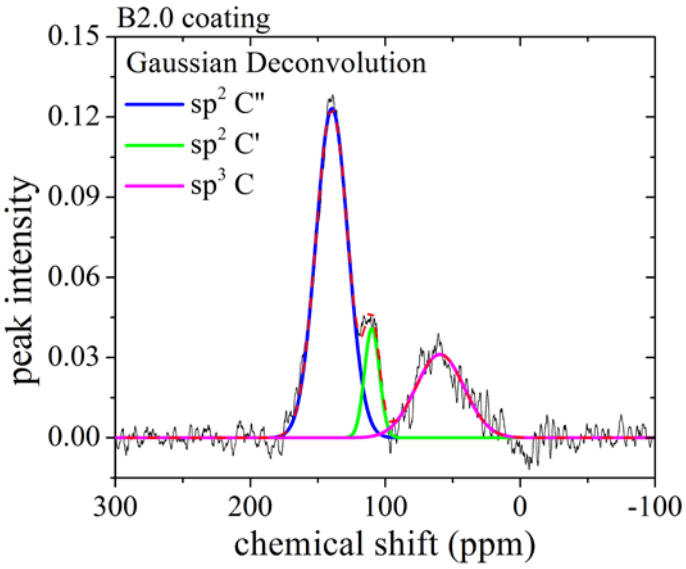

Figure 4.6 The deconvolution analysis of ^{13}C MAS spectra by Gaussian formula.

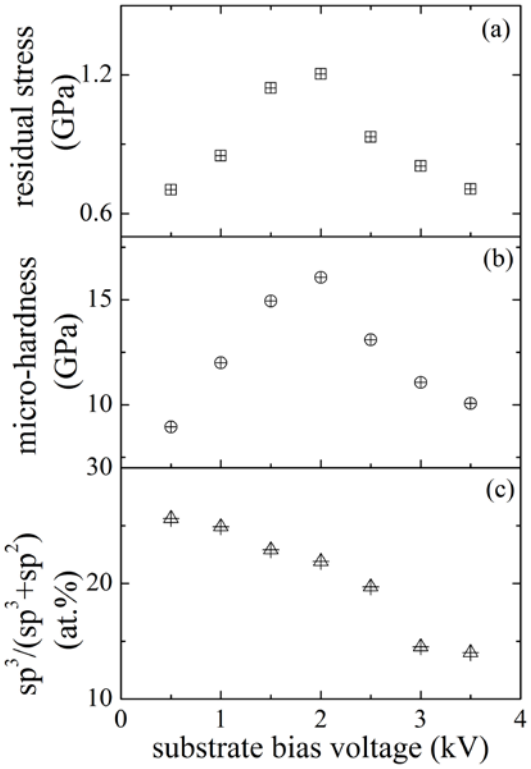

Figure 4.7 The $sp^3/(sp^3+sp^2)$ ratio and the mechanical properties of a-C:H coatings as the function of substrate bias voltage.

4.3.2 $sp^3/(sp^3+sp^2)$ ratio determined by CPMAS

In ^{1}H-decoupled CPMAS experiments, cross polarization contact time was varied from roughly-estimated spin-lock relaxation time $T_{1\rho}$ to various durations. In case of 0.2 ms contact time, initial magnetization transfer to ^{13}C nuclei only derived from carbon-bonded ^{1}H spins; as the contact time increased, the magnetization transfer can be enhanced by neighboring ^{1}H spins, so that CPMAS could be hardly used for quantification of $sp^3/(sp^3+sp^2)$ ratio [21, 22]. However, being sensitive to the protonated carbons and the inter-distance between ^{13}C and ^{1}H spins, CPMAS spectra usually provide rich information on C-H bonding structure in hydrogenated carbon coatings. Fig. 4.8 describes the CPMAS spectra of B1.5 fragment obtained after 10000 scans at a spinning rate of 17 kHz. Compared with ^{13}C MAS spectra, the CPMAS spectra obtained with 0.2 ms contact time exhibited relatively highest content of sp^3 C, indicating that most hydrogen atoms were coordinated with sp^3 C. Furthermore, such a preferential coordination of hydrogens with sp^3 C was proved by the development of signal amplitude of sp^2 C″ and sp^3 C peaks with an increase of contact time, as shown in Fig. 4.9. Previous research [22] have showed that the CPMAS spectra of organic compounds without molecular motion reach its maximum

signal amplitude at approximately 1~2 ms contact time for protonated carbons and 5 ms for non-protonated carbons, respectively. In case of studied a-C:H fragments, the maximum signal amplitude was achieved at 2 ms for sp^2 C″ peak and 5 ms for sp^3 C peak.

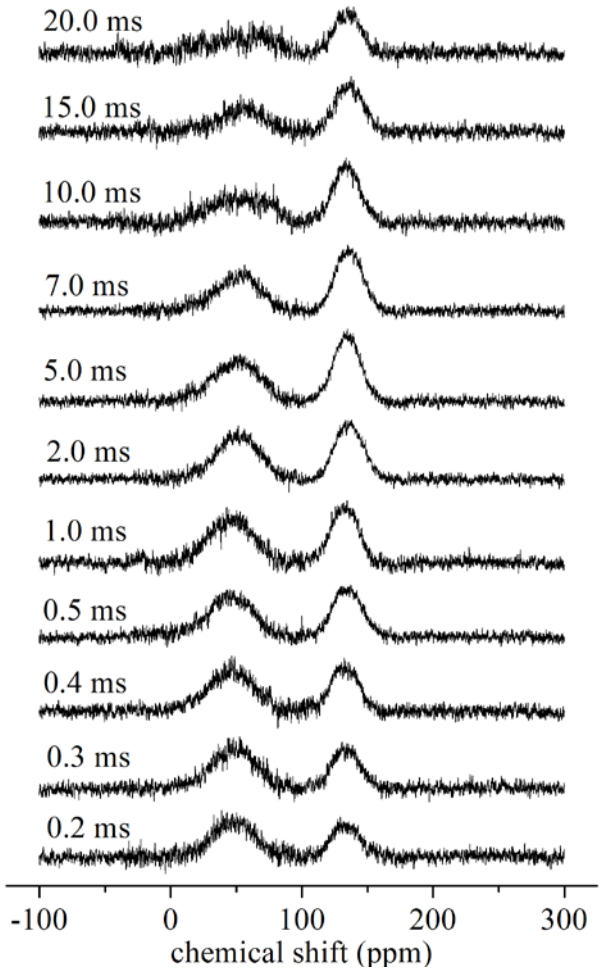

Figure 4.8 CPMAS spectra of B1.5 fragments as the function of contact time.

As a result, the $sp^3/(sp^3+sp^2)$ ratio determined by CPMAS spectra varied greatly with contact time, as shown in Fig. 4.10. The sp^3 C fraction decreased rapidly with the increase of contact time within 0.2~5 ms, during which the initial magnetization firstly transferred from ^1H spins to protonated carbons which were mostly in hybridization of sp^3 and then to non-protonated carbons; afterwards, the ratio kept relatively constant as 48 at.% within 5~20 ms. Because the signal intensity of CPMAS spectra is proportional to the number of C-H bonds, the preferential coordination of protons with sp^3 C and presence of non-protonated sp^2 C′ clusters would make the $sp^3/(sp^3+sp^2)$ ratio obtained by CPMAS spectra much higher than the ratio obtained by ^{13}C MAS spectra. Meanwhile, the *S/N* ratio of CPMAS spectra

shown in Fig. 4.8 developed to its optimal condition at 5 ms contact time and gradually weakened at longer contact time. This tendency is attributed to the quick relaxation of spin-locked ^{1}H magnetization during contact pulse within 0~$T_{1\rho}$. The spin-locking field is too weak to support the initial ^{1}H magnetization, and has a reducing effect on the degree of cross polarization transfer [22].

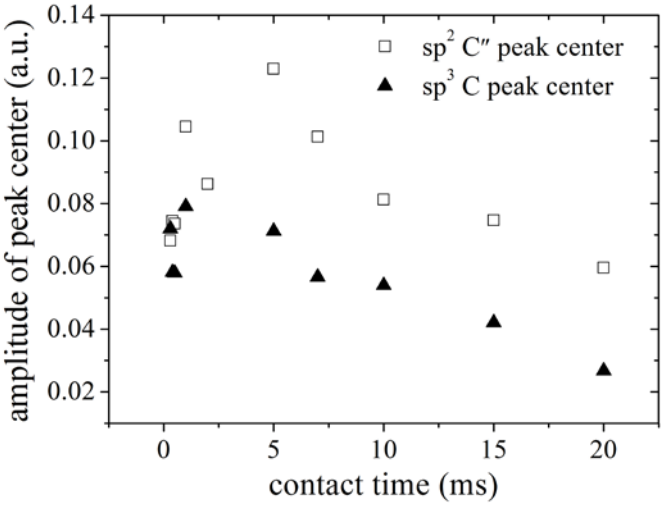

Figure 4.9 The peak height of sp^2 C″ and sp^3 C in CPMAS spectra of B1.5 fragments as the function of contact time.

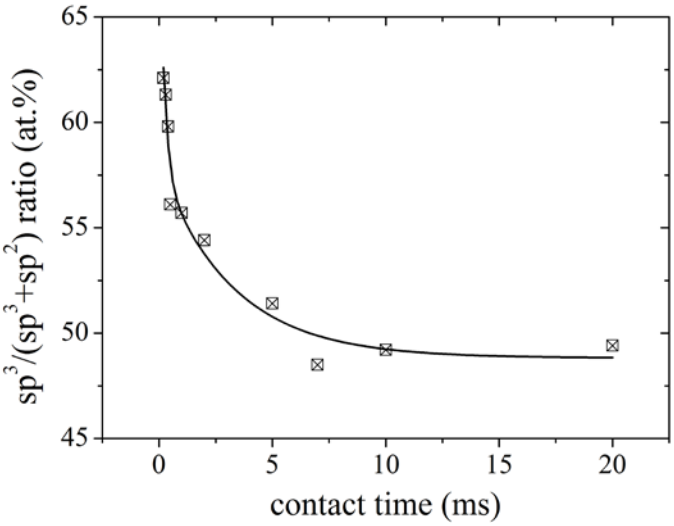

Figure 4.10 The $sp^3/(sp^3+sp^2)$ ratio determined by CPMAS spectra as the function of contact time of B1.5 fragment.

4.3.3 Comparison of $sp^3/(sp^2+sp^3)$ ratio determined by XPS, EELS and ^{13}C MAS

In this section, a comparison of $sp^3/(sp^2+sp^3)$ ratio obtained by XPS, EELS and NMR were presented. Taking B1.5 and B2.0 coating as an example, Figure 4.11 shows the deconvoluted XPS C1s spectra of B2.0 coating. The C1s spectra were

deconvoluted to four peaks in shape of combined Gaussian and Lorentzian formulas (GL) with a Shirley background by using "CasaXPS" software, and the shape of Lorentzian was fixed as 20% in GL combination. Charge-up calibration was performed by adjusting the position of C=C bond to 284.5 eV. According to Ref. [26-28], the binding energy of C=C peak was fixed at 284.5 eV and its full width at half maximum (FWHM) was constrained below 1.5 eV, whereas the C-C peak was fixed at 285.3 eV, and its FWHM was restricted below 2 eV. The remained part was attributed to C=O and C-O peaks with FWHM restricted below 3 eV.

Meanwhile, Figure 4.12 shows the EELS spectra of B2.0 coating, and technically the sp^2 fraction can be calculated on basis of Eq. (4.7). However, as the standard graphite sample was not measured at the same time for comparison, only a qualitative analysis of sp^2 fraction can be realized in this thesis. The higher $A_{\pi^*}/(A_{\pi^*}+A_{\sigma^*})$ ratio represents a higher fraction of sp^2 C in tested coatings.

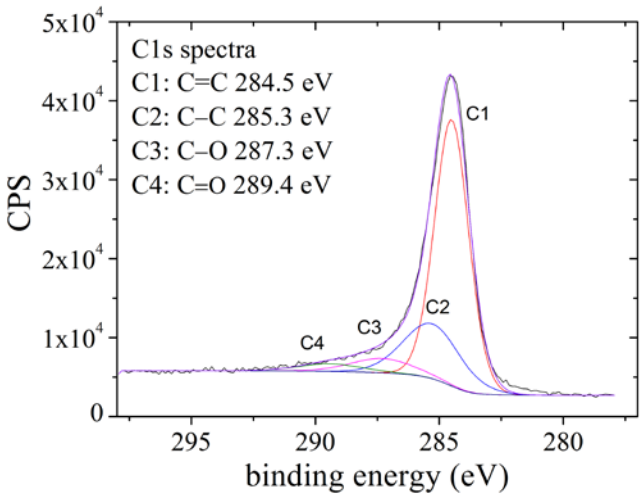

Figure 4.11 The XPS C1s spectra and deconvolution analysis of B2.0 coating.

Table 4.2 gives the $sp^3/(sp^3+sp^2)$ ratio obtained by NMR and XPS, in comparison with the $A_{\pi^*}/(A_{\pi^*}+A_{\sigma^*})$ ratio obtained by EELS. It seems that the value of $A_{\pi^*}/(A_{\pi^*}+A_{\sigma^*})$ ratio is well consistent with the $sp^3/(sp^2+sp^3)$ ratio obtained by NMR, but the $sp^3/(sp^3+sp^2)$ ratio obtained by XPS is quite different from NMR results, and shows a large range of error due to the undefined peak shift calibration before deconvolution analysis. To be specific, in XPS spectra analysis, a charge-up calibration is generally acquired to eliminate the effects from electrostatic adherence on top surface. Before deconvolution analysis, the peak position of C1s spectra is generally shifted to 284.5 eV. However, according to our knowledge, as the values of peak shift varied by ±0.02 eV, the calculated $sp^3/(sp^3+sp^2)$ ratio would change largely

by 0.1~0.15, even showed a similar residual STD below 5% at any time. Thus, a quantitative comparison of $sp^3/(sp^3+sp^2)$ ratio by XPS and NMR for few individual samples will make little sense and produce confusing results. However, from the perspective of comparative analysis, XPS can yet be applied as an convenient technique for structure characterization of a-C:H coating.

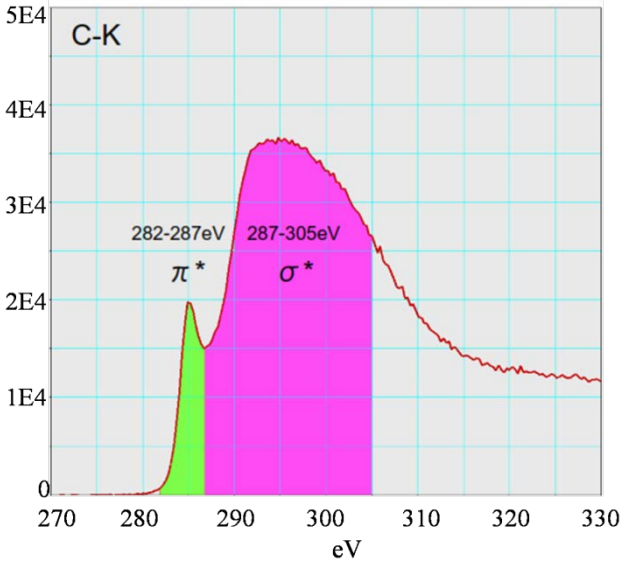

Figure 4.12 The EELS spectra of B2.0 coating.

$$sp^2\% = 100 \times \frac{\frac{A_{\pi^*}}{A_{\pi^*}+A_{\sigma^*}}}{\frac{G_{\pi^*}}{G_{\pi^*}+G_{\sigma^*}}} \qquad (4.7)$$

where G represents graphite and A represents tested sample.

Table 4.2 The comparison of sp^3 fraction obtained by XPS, EELS and NMR of B1.5 and B2.0 coatings.

	XPS $sp^3/(sp^3+sp^2)$ (at.%)	^{13}C NMR $sp^3/(sp^3+sp^2)$ (at.%)	EELS $A_{\pi^*}/(A_{\pi^*}+A_{\sigma^*})$ (%)
B1.5	49±15	23	9.4
B2.0	26±15	22	9.7

4.4 Conclusions

In this chapter, $sp^3/(sp^3+sp^2)$ ratio of ion-vapor deposited a-C:H coating was obtained by ^{13}C MAS. As bias voltage increased from 0.5 kV to 2 kV, both the

hardness and residual stress of studied a-C:H coating reached at its maximum value and then gradually reduced with further increase of bias voltage, while the $sp^3/(sp^3+sp^2)$ ratio continuously reduced with the increase of bias voltage in the whole range of 0.5~3.5 kV. It reveals that the mechanical property of studied a-C:H coating is proportional to the fraction of diamond-like cross-linked sp^3 C, rather than the total population of sp^3 C. Also, two distinct types of sp^2 sites were observed in ^{13}C MAS spectra: a dominant peak centered around 137 ppm and a shoulder peak centered around 105 ppm. The shoulder peak totally disappeared in CPMAS spectra with any contact time between 0.2~20 ms, suggesting that this minor type of sp^2 sites are completely hydrogen-free and also distant from hydrogen atoms. Meanwhile, the much higher $sp^3/(sp^3+sp^2)$ ratio given by CPMAS spectra than that of ^{13}C MAS spectra implied that in studied a-C:H coatings, there was a preferential coordination of hydrogen atoms to sp^3 C. Such kind of preferential coordination had further proved that the mechanical property of studied a-C:H coating is not simply proportional to the total population of sp^3 C.

References

[1] J. Robertson. Diamond-like amorphous carbon. Mater. Sci. Eng., R. 37, 129-281 (2002)

[2] A. Erdemir, C. Donnet. Tribology of diamond-like carbon films: recent progress and future prospects. J. Phys. D: Appl. Phys. 39, 311-327 (2006)

[3] Gyunggoo Cho, Bing K. Yen, Christopher A. Klug. Structural characterization of sputtered hydrogenated amorphous carbon films by solid state nuclear magnetic resonance. J. Appl. Phys. 104, 013531 (2008)

[4] K. R. Carduner, M. J. Rokosz, M. A. Tamor, W. C. Vassell. Solid State NMR Study of Carbon Bonding in Amorphous Hydrogenated Carbon Films. Appl. Meg. Res., 2, 647-653 (1991)

[5] M. A. Tamor, W. C. Vassell, K. R. Carduner. Atomic constraint in hydrogenated "diamondlike" carbon. Appl. Phys. Lett., 58, 592 (1991)

[6] Maksym Rybachuk, John M. Bell. The effect of sp^2 fraction and bonding disorder on micro-mechanical and electronic properties of a-C:H films. Thin Solid Films. 515, 7855-7860 (2007)

[7] M. A. Tamor, J. A. Haire, C. H. Wu, K. C. Hass. Correlation of the optical gaps and Raman spectra of hydrogenated amorphous carbon films. Appl. Phys. Lett. 54,

123-125 (1989)

[8] M. Chhowalla, J. Robertson, C. W. Chen, S. R. P. Silva, C. A. Davis, G. A. J. Amaratunga, W. I. Milne. Influence of ion energy and substrate temperature on the optical and electronic properties of tetrahedral amorphous carbon (ta-C) films. J. Appl. Phys. 81, 139-145 (1997)

[9] J. Robertson. Properties of diamond-like carbon. Surf. Coat. Tech. 50, 185-203 (1992)

[10] J. D. Carey, S. R. P. Silva. Disorder, clustering, and localization effects in amorphous carbon. Phys. Rev. B. 70, 235417 (2004)

[11] G. T. Gao, Paul T. Mikulski, Judith A. Harrison. Molecular-scale tribology of amorphous carbon coatings: effects of film thickness, adhesion, and long-range interaction. J. Am. Chem. Soc. 124, 7202-7209 (2002)

[12] G. T. Gao, Paul T. Mikulski, Ginger M. Chateauneuf, Judith A. Harrison. The effects of film structure and surface hydrogen on the properties of amorphous carbon films. J. Phys. Chem. b. 107, 11082-11090 (2003)

[13] Donald W. Brenner, Olga A. Shenderova, Judith A. Harrison, Steven J. Stuart, Boris Ni, Susan B. Sinnott. A second-generation reactive empirical bond order (REBO) potential energy expression for hydrocarbons. J. Phys.: Condens. Matter. 14, 783–802 (2002)

[14] K. D. Bouzakis, N. Michailidis. Indenter tip geometries and calibration procedures: deviations in determining coating “and other materials” mechanical properties. Proceedings of the 3rd International Conference on Manufacturing Engineering (ICMEN), 2008 October 1-3, Chalkidiki, Greece

[15] B. D. Beake, V. M. Vishnyakov, A. J. Harris. Relationship between mechanical properties of thin nitride-based films and their behaviour in nano-scratch tests. Tribol. Int. 44, 468-475 (2011)

[16] J. L. Loubet, M. Bauer, A. Tonck, S. Bec. Gauthier-Manuel B. in: M. Nastasi, D. M. Parker, H. Gleiter, editors. Mechanical Properties and Deformation Behavior of Materials Having Ultra-Fine Microstructures. Kluwer Academic Publishers; 1993, p. 429-448

[17] G. Stoney. The tension of thin metallic films deposited by electrolysis. Proc. R. Soc. Lond., Ser. A, 82 (1909), pp. 172

[18] X. L. Peng, T. W. Clyne. Mechanical stability of DLC films on metallic

substrates: Part I-Film structure and residual stress levels. Thin Solid Films. 312, 207-218 (1998)

[19] Y. Maniwa, M. Sato, K. Kume, M. E. Kozlov, M. Tokumoto. Comparative NMR study of new carbon forms. Carbon. 34, 1287 (1996)

[20] A. M. Panich. Nuclear Magnetic Resonance Studies of Nanodiamonds. Critical Reviews in Solid State and Materials Sciences. 37, 276-303 (2012)

[21] C. Donnet, J. Fontaine, F. Lefèbvre, A. Grill, V. Patel et al. Solid state ^{13}C and ^{1}H nuclear magnetic resonance investigations of hydrogenated amorphous carbon. J. Appl. Phys. 85, 3264-3270 (1999)

[22] M. J. Duer. Solid-State NMR Spectroscopy Principles and Applications. Cambridge: Blackwell Science Ltd, 2002, p. 73-103

[23] T. Y. Leung, W. F. Man, P. K. Lim, W. C. Chan, F. Gaspari, S. Zukotynski. Determination of the sp^3/sp^2 ratio of a-C by XPS and XAES. J. Non-Cryst. Solids. 254, 156–160 (1999)

[24] S. T. Jackson, R. G. Nuzzo. Determining hybridization differences for amorphous carbon from the XPS C 1s envelope. Appl. Surf. Sci. 90, 195–203 (1995)

[25] P. Merel, M. Tabbal, M. Chaker, S. Moisa, J. Margot. Direct evaluation of the sp^3 content in diamond-like-carbon films by XPS. Appl. Surf. Sci. 136, 105–110 (1998)

[26] T. Y. Leung, W. F. Man, P. K. Lim, W. C. Chan, F. Gaspari, S. Zukotynski. Determination of the sp^3/sp^2 ratio of a-C by XPS and XAES. J. Non-Cryst. Solids. 254, 156–160 (1999)

[27] S. T. Jackson, R. G. Nuzzo. Determining hybridization differences for amorphous carbon from the XPS C 1s envelope. Appl. Surf. Sci. 90, 195–203 (1995)

[28] P. Merel, M. Tabbal, M. Chaker, S. Moisa, J. Margot. Direct evaluation of the sp^3 content in diamond-like-carbon films by XPS. Appl. Surf. Sci. 136, 105–110 (1998)

5 The heterogeneous structure of ion-vapor deposited a-C:H coating on nanoscale

5.1 Introduction

Besides the aforementioned quantification of $sp^3/(sp^3+sp^2)$ ratio, another two inevitable issues in recent study of a-C:H coatings are the sp^2 C clustering structure and fabricated defects configuration in amorphous carbon network. Both of the play significant roles in the determination of electrical and optical properties of a-C:H coatings [1-5]. Early calculation of Robertson and O'Reilly [1] showed that in plasma-deposited amorphous carbon coatings, the most stable arrangement of sp^2 sites is in compacted clusters of fused six-fold rings with sp^3 hybridized boundary sites, and the width of optical band gap varied inversely with sp^2 cluster size. Khan and Carey [2] controlled the sp^2 C cluster size and hopping distance by varying the ion dose of B^+ implantation for r.f. PECVD-deposited a-C:H coatings, and thus governed the Tauc gap and resistivity of a-C:H coating. Carey and Silva [3] concluded two types of disorder in carbon network: one is the structural disorder associated with sp^2 clusters in the same size but different degree of distortion and the other is topological disorder assigned with undistorted sp^2 C clusters but in different size. Also, the close correlations between Urbach energy, Raman G peak bandwidth and spin density (i.e., density of unpaired electron determined by electron paramagnetic resonance) of a-C:H coatings were discussed [3].

From the perspective of NMR experimental research of a-C:H coatings, the features of network disorder and fabricated defects can be effectively reflected by the spin-lattice relaxation time (T_1), which is ruled by the energy exchange between excited nuclear spins and surround "lattice". Previous research by A. M. Panich et al [6, 7] revealed that both the anomalous reduction of T_1 and stretched-exponential feature of longitudinal magnetization recovery curve are attributed to the interaction of nuclear spins with nearby paramagnetic impurities consisting of fabricated dangling bonds. By performing T_1(H) measurements and multiple quantum (MQ) experiments, C. Jäger et al [8, 9] discovered structural heterogeneity of PECVD-deposited a-C:H coating on basis of the bi-exponential relaxing behavior of protons, and proposed a nano-metric heterogeneous structural model consisting of short chains of sp^3 CH_2 and

amorphous matrix separated by a layer of chain-like sp^2 C. However, some researchers held reservations on this model since the short T_1(H) as 14 ms was impossibly originated from nuclear-nuclear dipolar interaction without molecular motion in a-C:H fragments [10, 11]. Also, no significant difference was discovered in their CPMAS and ^{13}C MAS spectra when a layer of non-protonated sp^2 C embedded between short chains of sp^3 CH_2 and amorphous matrix. This experimental result was inconsistent with their structural model and obviously different from our experimental results as well.

Considering the impressed differences between ^{13}C MAS spectra and CPMAS spectra of ion-vapor deposited a-C:H coatings as mentioned in chapter 4, we investigated the spin-lattice relaxation behavior of ^{13}C and ^{1}H spins in this chapter, and discussed the unique structural heterogeneity and sp^2 clustering structure of studied a-C:H coatings.

5.2 Experimental details

For the measurement of spin relaxation time (T_1) of ^{1}H and ^{13}C spins, the saturation recovery technique (illustrated in Fig. 2.8 and Fig. 2.9) were applied and the relaxing interval between saturation sequence and 90° single pulse was set as {1 ms, 5 ms, 10 ms, 50 ms, 70 ms, 100 ms, 150 ms, 200 ms, 250 ms, 300 ms, 350 ms, 400 ms, 500 ms, 700 ms, 900 ms} and {0.5 s, 1 s, 2.5 s, 5 s, 10 s, 15 s, 30 s} for ^{1}H and ^{13}C spins, respectively. Also, the number of scanning cycles for ^{1}H and ^{13}C nuclei were set as 32 and 20000, respectively, to achieve a desired signal-to-noise ratio of each spectra.

Additionally, in order to give deeper insights into the sp^2 clustering configurations, the optical gap of studied a-C:H coatings including Tauc gap and E_{04} gap were measured by applying JASCO ARSN-733 UV/VIS/NIR spectrophotometer, and tested coatings were deposited on ultrasonically cleaned quartz substrates for 1 hour to reach a thickness around 300 nm. The optical gap was determined from the Tauc point E_g of absorption spectra using Eq. (5.1):

$$(\alpha h\nu)^{1/2} = B(E_g - h\nu) \qquad (5.1)$$

where B is the density of the localized state constant, and α is the absorption coefficient which can be calculated with known data of transmission (i.e. T), reflection (i.e. R) and coating thickness (i.e. d determined by SEM cross-sectional observation) as described by Eq. (5.2):

$$T = (1-R)^2 e^{-\alpha d} \qquad (5.2)$$

As a absorption spectra is plotted by Tauc equation [12-14], and the Tauc optical gap E_g can be acquired from an extrapolation of the linear part of absorption spectra when α equals 0.

5.3 Results and discussions

As we mentioned in Chap. 4, a noticeable shoulder peak denoted as sp^2 C′ centering around 105 ppm is observed at the right side of dominant sp^2 peak in each ^{13}C MAS spectra, which is quite distinct from previous reports of a-C:H coatings [8-12] yet resembles the ^{13}C MAS spectra of nanodiamonds in particle size of 4~5 nm with a chemically-unlike shell at the outside surface [6, 7]. Fig. 5.1 describes the atomic fraction of sp^2 C′ sites as a function of bias voltage. Consistent with the tendency of Raman FWHM(G) with an increase of bias voltage as shown in Fig. 3.8, the fraction of sp^2 C′ sites increased from 3 at.% to its maximum value at 2 kV as the coating structure transformed from polymer-like carbon to diamond-like carbon (PLC→DLC) and then reduced quickly from the maximum value to 4 at.% as the coating structure transformed from diamond-like carbon to graphite-like carbon (DLC→GLC). It seems that the generation of sp^2 C′ sites are strongly related to the nanoclustering of sp^2 C sites and the network disordering of studied coatings.

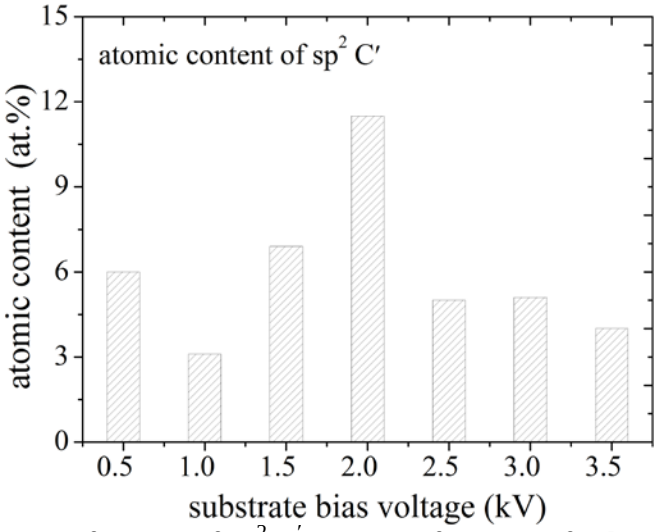

Figure 5.1 The atomic fraction of sp^2 C′ sites as a function of substrate bias voltage.

5.3.1 Clustering model of sp^2 C sites

In previous researches of amorphous carbon coatings [1-5, 15, 16], Raman FWHM(G) is an effective indicator of sp^2 C clustering and clearly related to the optical band gap and electrical properties of a-C:H coatings. Also, it has been argued

that in plasma deposited a-C:H coatings, sp^2 C sites tend to be stabilized as π bonded clusters of certain size embedded in sp^3 bonded matrix [1-3]. In this study, the consistence tendency of Raman FWHM(G) and sp^2 C′ fractions with an increase of bias voltage (shown in Fig. 3.8 and Fig. 5.1, respectively) also suggests a strong correlation between the generation of sp^2 C′ sites and the disordering of carbon network. The fraction of sp^2 C′ sites, merely occupying 3~12 at.% and reaching at the maximum value at 2 kV rather than continuously with higher bias voltage, reveals that sp^2 C′ sites are not the dominant component of carbon network. Especially as the bias voltage was higher than 2 kV, the Raman FWHM(G) reduced rapidly with bias voltage due to the enhanced formation of graphite-like sp^2 C clusters and integration of neighboring sp^2 C clusters, whereas the content of sp^2 C′ fell down to 4~5 at.%. An possible explanation on this phenomenon is that sp^2 C′ sites are specifically embedded between dominant sp^2 C″ clusters and sp^3 matrix as trapped interfaces or boundaries where sp^2 carbon bonding are highly distorted, as demonstrated in Fig. 5.2. And thus, the tendency of sp^2 C′ fraction with an increase of bias voltage shown in Fig. 5.1 can be well understood, as shown in Fig. 5.3. At first, as the bias voltage is below 1.0 kV (see in Fig. 5.3a), the clustering tendency of sp^2 C″ sites is likely to be low, and the interspace between individual sp^2 C″ clusters is also large; as a result, the fraction of boundary sp^2 C′ sites is also few. And next, when the bias voltage increases to 1.0~2.5 kV (see in Fig. 5.3b), more localized sp^2 C″ clusters in larger size are formed, yet, below the nano-crystalline graphite in disordering phase, so that more boundary sp^2 C′ sites are produced and the interspaces between individual sp^2 C″ clusters becomes smaller. Consistently, the a-C:H coatings deposited under this condition exhibit higher

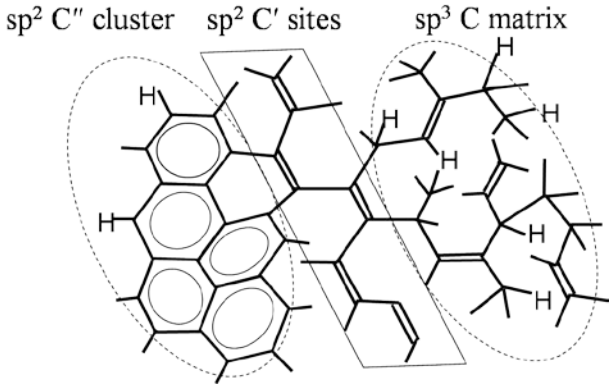

Figure 5.2 Schematic illustration on the sp^2 C′ clusters as trapped interface or boundary between the dominantsp^2 C″ clusters in aromatic ring structure and the amorphous sp^3 C matrix.

micro-hardness and residual stress (see in Fig. 4.5) due to the decreasing content of hydrogens and maximizing content of diamond-like sp^3 C bonding. Finally, as the bias voltage further increases above 2.5 kV (see in Fig. 5.3c), the graphite-like structural transformation of coating is highly enhanced [15-17] through the integration and re-ordering of individual sp^2 C″ clusters, so that the fraction of boundary sp^2 C′ site turns into lower [2].

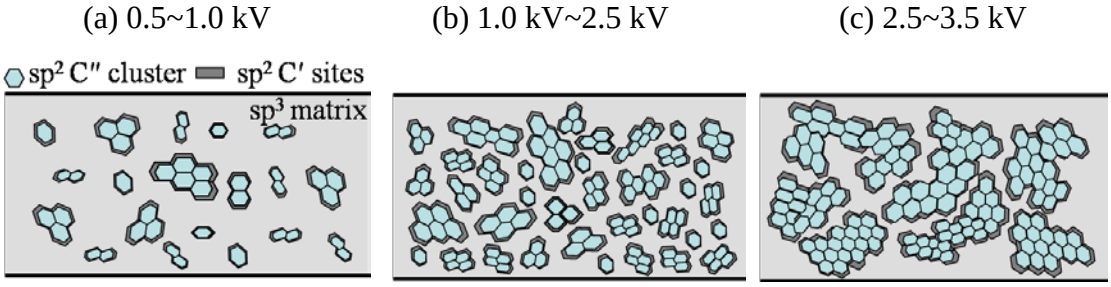

Figure 5.3 Schematic illustration on the generation mechanism of sp^2 C′ sites in ion-vapor deposited a-C:H coatings as a function of bias voltage and sp^2 C" cluster size.

5.3.2 Spin-lattice relaxation behavior of ^{13}C spins

Actually, heterogeneous structure model of a-C:H coating was firstly presented by Jäger [8, 9] on basis of the bi-exponential spin-lattice relaxation behavior of ^1H spins. They proposed that in PECVD-deposited a-C:H coating, there is a cluster of "chain-like" non-protonated sp^2 C which restrains the magnetization transfer from short chains of sp^3 CH_2 clusters with T_1(H) of 14 ms to amorphous carbon network with T_1(H) of 120 ms. However, at the same time they reported a single-exponential relaxation of sp^2 C (expressed as Eq.(5.3)) and bi-exponential relaxation of sp^3 C (expressed as Eq.(5.4)) [10, 11], which was obviously contradictory to their heterogeneous structure model, i.e. the presence of non-protonated sp^2 C. Also, some researchers held other reservations on this model since the short T_1(H) as 14 ms was impossibly caused by direct nuclear-nuclear dipolar interaction without molecular motion but only possible caused by the electron-nuclear interaction from localized unpaired electron to neighboring nuclear spins [10, 11]. Meanwhile, both the

temperature independence of ^{13}C and ^{1}H magnetization relaxation and high density of unpaired electrons as 10^{17}~10^{21} e/cm^{-3} regardless of deposition methods prove with certainty that in a-C:H coatings [18], the nuclear magnetization relaxation behavior is strongly affected by unpaired electrons and typically exhibited stretched-exponential approximation (expressed as Eq.(5.5)) for a continuous distribution of paramagnetic centers with different number of unpaired electrons [6, 7, 10, 11, 19].

$$M(t)/M(0) = 1 - Ce^{-(t/T_1)} \tag{5.3}$$

$$M(t)/M(0) = M_a\left(1 - Ce^{-\left(t/T_1^{\,a}\right)}\right) + M_b\left(1 - Ce^{-\left(t/T_1^{\,b}\right)}\right) \tag{5.4}$$

$$M(t)/M(0) = 1 - Ce^{-(t/T_1)^{\alpha}} \tag{5.5}$$

where $M(t)$ is the magnetization at time t, M_0 the equilibrium magnetization, C equals 2 for inversion recovery measurement and 1 for saturation recovery measurement, M_a and M_b the fraction associated with two components $T_1^{\,a}$ and $T_1^{\,b}$, respectively, and $M_a + M_b$=100%, α the stretched index typically within 0.5~1 which specifically represents the presence of paramagnetic centers. As α equals 1, the stretched exponential turns into single-exponential fitting, implying no presence of paramagnetic centers. Generally, as the spin density (i.e. the density of un-bonded electrons) of DLC coating reduced from 10^{21} to 10^{17} N/cm^{-3} [6], the value of stretched index α increased correspondingly from 0.5 to 1, so that the value of α approaching to 0.5 is a strong indicator on large presence of paramagnetic center near studied nuclei.

In this study, spin-lattice relaxation time of ^{13}C and ^{1}H were measured by applying saturation recovery sequence with a relaxation delay of 1 s. Taking B2.5 fragments as an example, the ^{13}C spectra acquired after various interval within 0.5~30 s are displayed in Fig. 5.4. Clearly, it can be seen that as the interval is longer than 5 s, the intensity of acquired ^{13}C spectra is tend to resembles the ^{13}C MAS spectra (see in Fig. 4.5), which indicates that most of ^{13}C spins can relax to its equilibrium state after 5 s relaxation delay. Accordingly, the magnetization recovery curves of sp^2 C″, sp^2 C′, sp^3 C were tried to be fitted by Eq.(5.3)~ Eq.(5.5) using *least squares approximation* in which the stretched power α and component fraction M_a and M_b were variables, and fine-converged fitting results of these three types of spins are listed in Table 5.1, together with the values of mean square of error (i.e. MSE) and coefficient of determination (i.e. R-sq(adj)). The fitting curves of sp^2 C″, sp^2 C′, sp^3 C are displayed in Fig. 5.5~5.7, respectively. For sp^2 C″ and sp^3 C spins, their relaxation curves can be

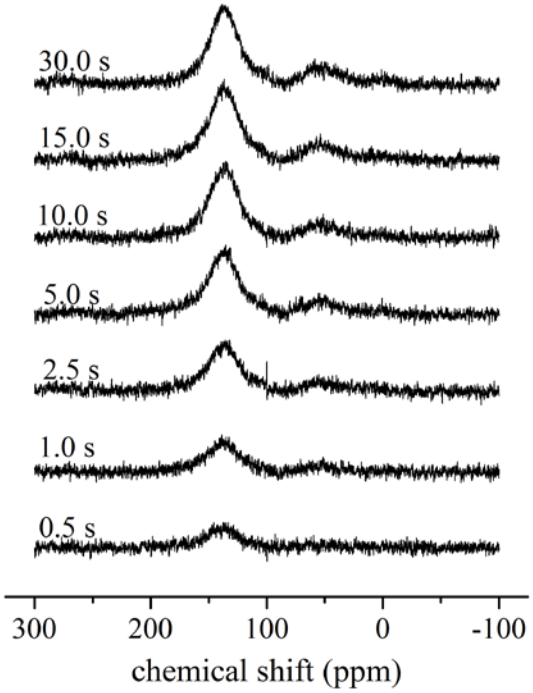

Figure 5.4 The ^{13}C spectra acquired after various intervals within 0.5~30 s before the 90° single pulse.

Table 5.1 The exponential fitting results of sp^2 C'', sp^2 C' and sp^3 C.

exponential formula	sp^2 C''	sp^2 C'	sp^3 C
single-	T_1=2.71 s±0.05 s MSE=1.7E-3 R-sq(adj)=98.2%	T_1=5.09 s±0.05 s MSE=6.3E-4 R-sq(adj)=99.5%	T_1=3.75 s±0.05 s MSE=7.6E-4 R-sq(adj)=99.4%
binary-	/	/	/
stretched-	T_1=2.83 s±0.05 s α =0.791±0.005 MSE=1.1E-4 R-sq(adj)=99.9%	/	T_1=3.78 s±0.05 s α=0.965±0.005 MSE=8.6E-4 R-sq(adj)=99.3%

both fitted well by single and stretched exponential formula with T_1 approximately equal 2.7 s and 3.8 s, respectively, while the two exponential formulas give almost the same value of T_1. For sp^2 C′ spins, their recovery curve can only converge in single-exponential fitting with T_1 equal 5.1 s. Technically, compared with the shorter T_1 of sp^2 C″ and sp^3 C spins, the longer T_1 of sp^2 C′ spins are attributed to the preferential distribution of hydrogen atoms near sp^2 C″ and sp^3 C. As long as the distance from sp^2

C′ clusters to ^{1}H spins is large enough, their heteronuclear dipolar-dipolar interactions can be largely prohibited, whereas the hydrogen-bonded and hydrogen-proximate ^{13}C nuclei can relax more quickly.

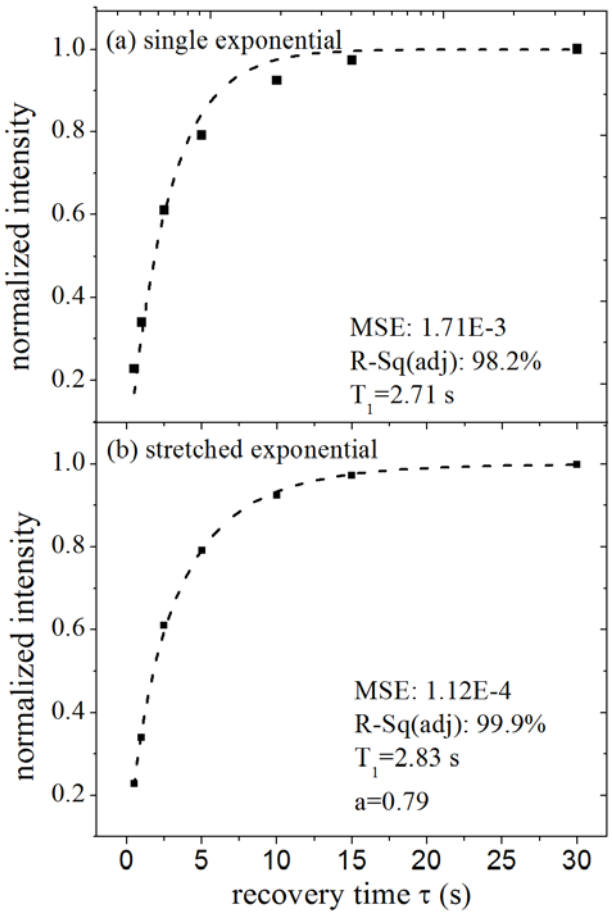

Figure 5.5 Fitting results of the magnetization recovery curve of sp^2 C'' clusters by single and stretched exponential functions for B2.5 fragment.

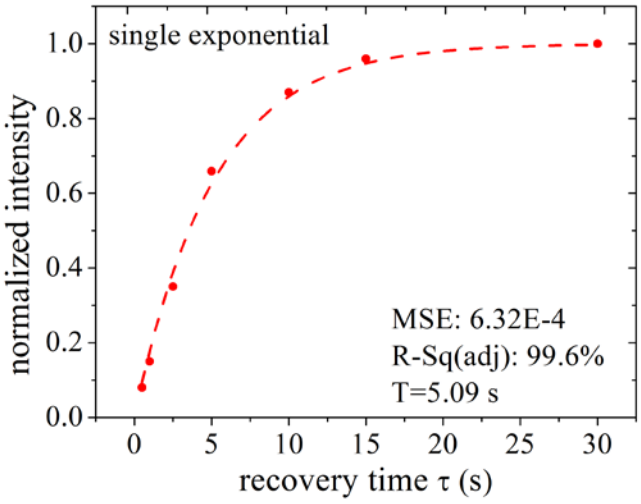

Figure 5.6 Fitting results of the magnetization recovery curve of sp^2 C' sites by single exponential functions for B2.5 fragment.

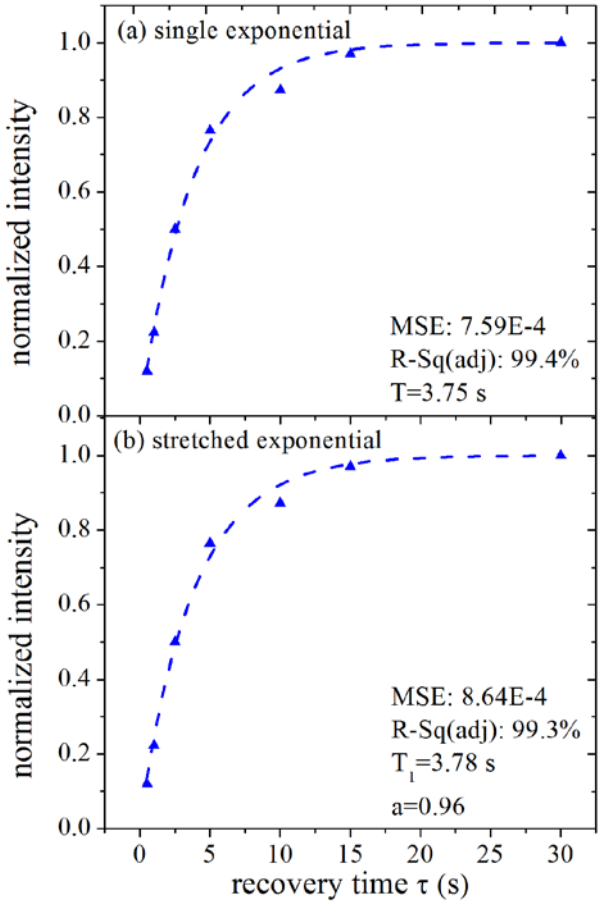

Figure 5.7 Fitting results of the magnetization recovery curve of sp^3 C by three types of exponential functions for B2.5 fragment.

However, as additionally attention is paid on the effect of experimental error [21], imperfect spectra resolution and defects configuration, it is hardly possible to classify relaxation mechanisms accurately for distinct types of clusters only on basis of the aforementioned experimental data. Although the optimal approximation of sp^2 C″ clusters was different from that of sp^2 C′ and sp^3 C, their magnetization recovery curves showed no significant difference. More adequate analysis on the unpaired electron distribution and correlated relaxation mechanisms can be attempted by further investigation on ESR spectra, spin counting, temperature dependence and the static magnetic properties [10, 11, 22] of a-C:H coatings.

Actually, not simply focusing on the specific values of MSE and R-sq(adj) obtained by using distinct fitting formulas, we thought that the similar value of T_1(sp^2 C") given by single and stretched exponential formula with α equal 0.79 suggest a strong stretched relaxing behavior, whereas the similar value of T_1(sp^3 C) given by single and exponential formula with α equal 0.96 proving a very weak stretched relaxing

behavior. And more importantly, it suggests that the paramagnetic centers tend to be preferentially closet to dominant sp^2 C" clusters.

5.3.3 Spin-lattice Relaxation behavior of ^{1}H spins

Similarly, the spin-lattice relaxation time of ^{1}H spins was measured by applying saturation recovery sequence with a relaxation delay of 1 s, and for example, Fig. 5.8 displays the ^{1}H spectra of B2.5 fragment acquired after various interval within 1~900 ms. As the interval is longer than 50 ms, the intensity of ^{1}H spectra is tend to stable, which indicates that almost all the ^{1}H spins can relax to its equilibrium state after 50 ms delay. For fragments B1.5~B3.5, all their ^{1}H recovery curves can be fine fitted by Eq.(5.4) and Eq.(5.5), as displayed in Fig. 5.9~5.13. Generally, by using bi-exponential formula, we obtained a major component of longer T_1^a(H) as 25~55 ms occupying 70~80% and a minor component of shorter T_1^b(H) as 0.1~0.3 ms occupying 20~30%, while by using stretched exponential formula, we obtained a medium value of T_1(H) as 17~40 ms with a stretched index as 0.5~0.6. As the contents of Fe ions in well-prepared a-C:H fragments are lower than 0.1 at.%, such an ultra short T_1^b(H) is only possibly attributed to the presence of fabricated defects such as unpaired electrons in carbon network [6].

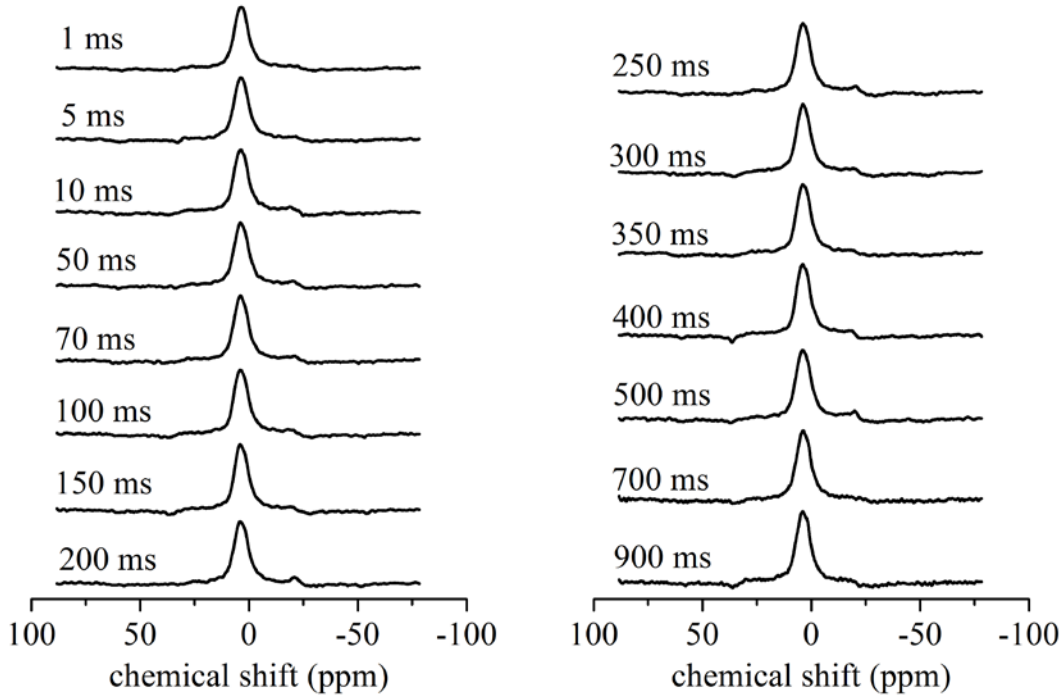

Figure 5.8 The ^{1}H spectra acquired after various intervals within 1~900 ms before the 90° single pulse of B2.5 fragment.

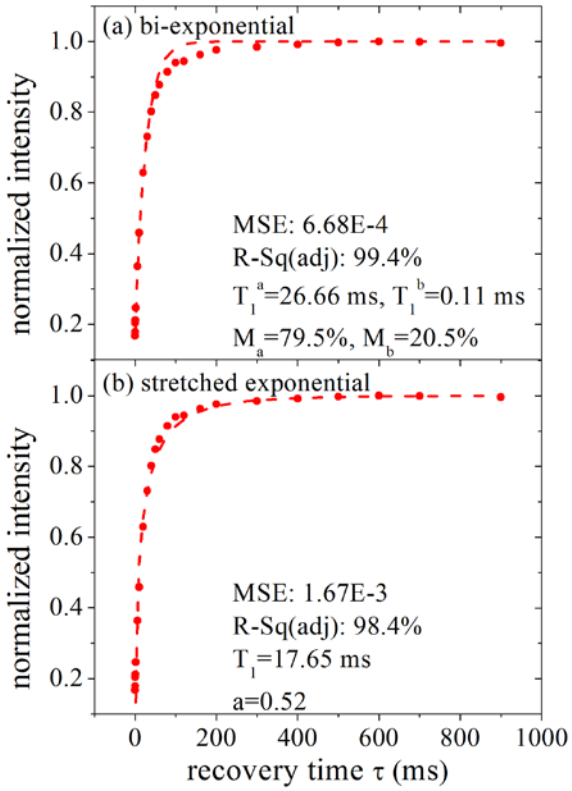

Figure 5.9 Fitting results of the magnetization recovery curve of ^{1}H spins by bi- and stretched exponential functions for B1.5 fragment.

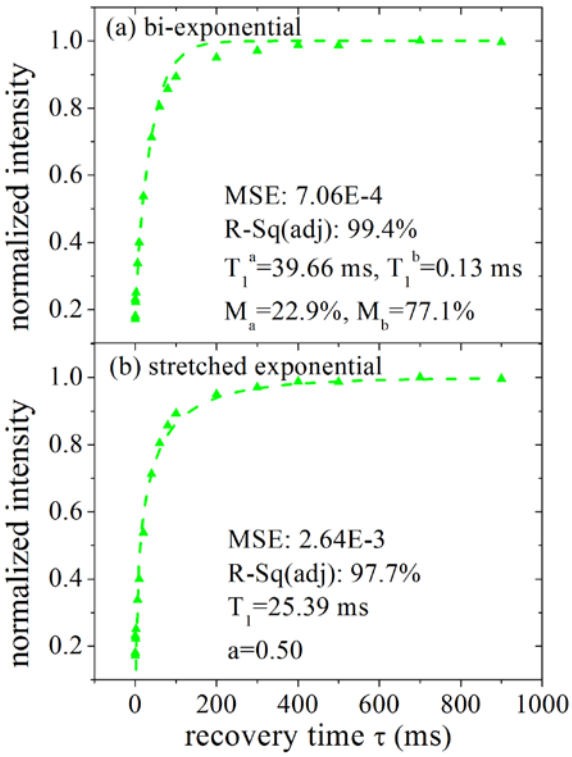

Figure 5.10 Fitting results of the magnetization recovery curve of ^{1}H spins by bi- and stretched exponential functions for B2.0 fragment.

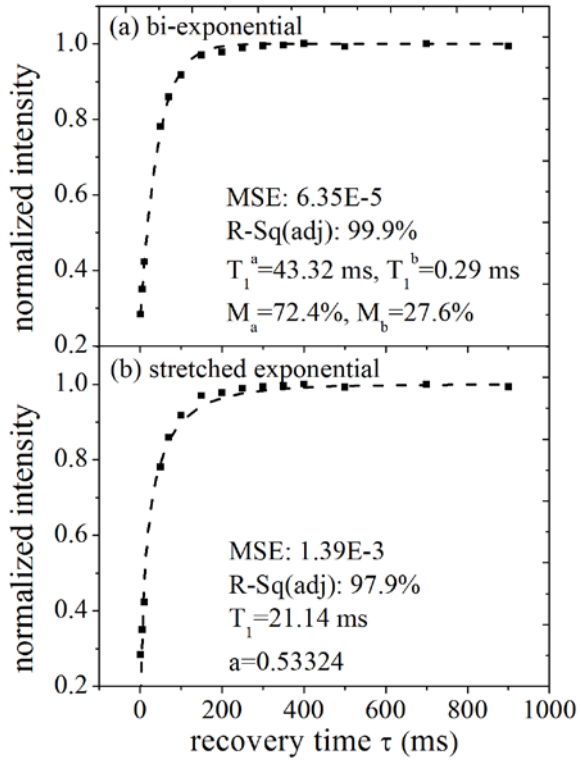

Figure 5.11 Fitting results of the magnetization recovery curve of ^{1}H spins by bi- and stretched exponential functions for B2.5 fragment.

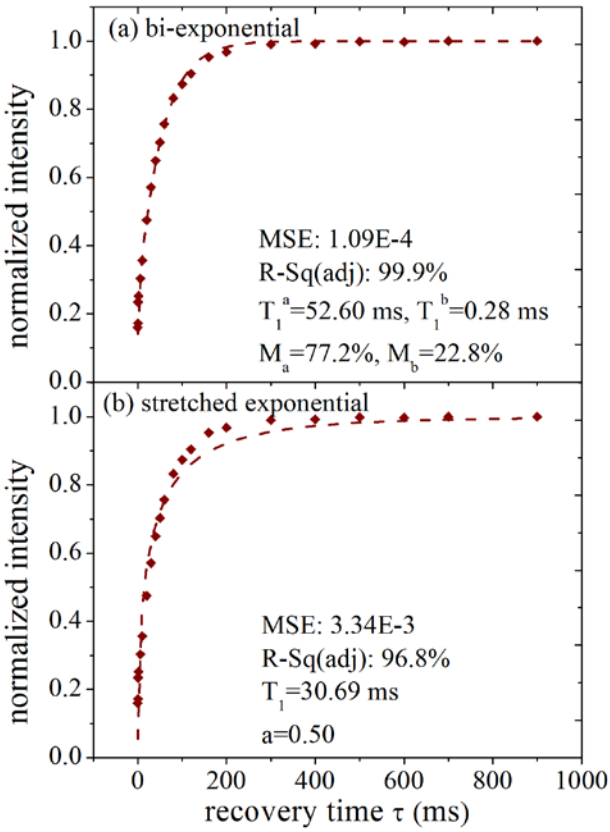

Figure 5.12 Fitting results of the magnetization recovery curve of ^{1}H spins by bi- and stretched exponential functions for B3.0 fragment.

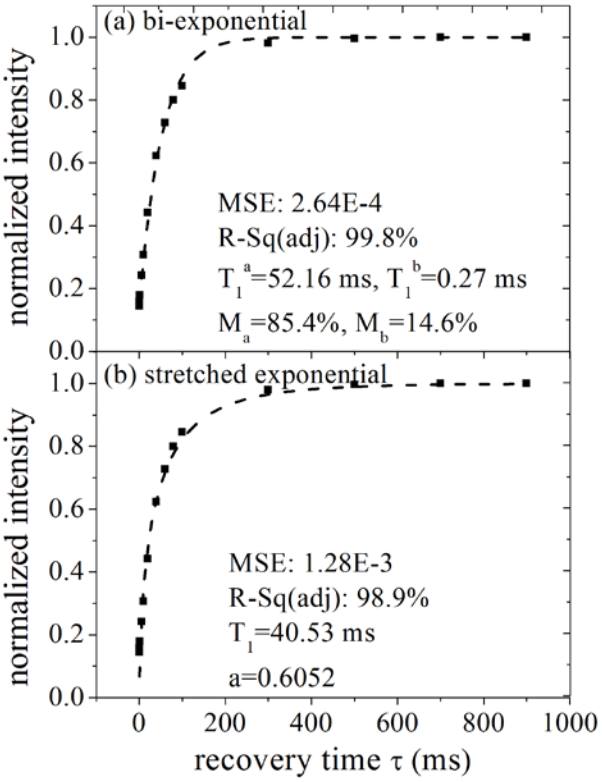

Figure 5.13 Fitting results of the magnetization recovery curve of ^{1}H spins by bi- and stretched exponential functions for B3.5 fragment.

Meanwhile, it is noticed that no matter the T_1 is determined by bi- or stretched exponential formula, it always shows a continuously increasing tendency as the bias voltage rises up from 1.5 kV to 3.5 kV, as shown in Fig. 5.13. In fact, as regard to the relaxation behavior of ^{1}H spins in a-C:H coating with natural abundance of ^{13}C nuclei, generally there are four types of relaxation mechanism as illustrated in Fig. 5.14. The first and dominant mechanism is homonuclear dipolar interactions between ^{1}H spins, while the heteronuclear interaction between ^{1}H and dilute ^{13}C spins is comparatively weaker; the third mechanism is spin diffusion from un-bonded electrons to nearby ^{1}H spins, and the fourth one is homonuclear interactions between two ^{1}H spins in a hydrogen molecular. In case of the T_1(H) determined by stretched-exponential fitting and the T_1^{a}(H) component determined by bi-exponential fitting, the value of T_1 grew up to 2~3 times than that of B0.5 coating, and such a great increase should be mainly attributed to a gradual decrease of hydrogen content in a-C:H coating, so that the effect of first relaxation mechanism is greatly weaken. By comparison, the value of T_1^{b}(H) component determined by bi-exponential fitting kept constant in the range of DLC and GLC structure as 0.1 ms and 0.3, respectively, and such a ultra-short

component is probably attributed to the third and fourth mechanism as mentioned above.

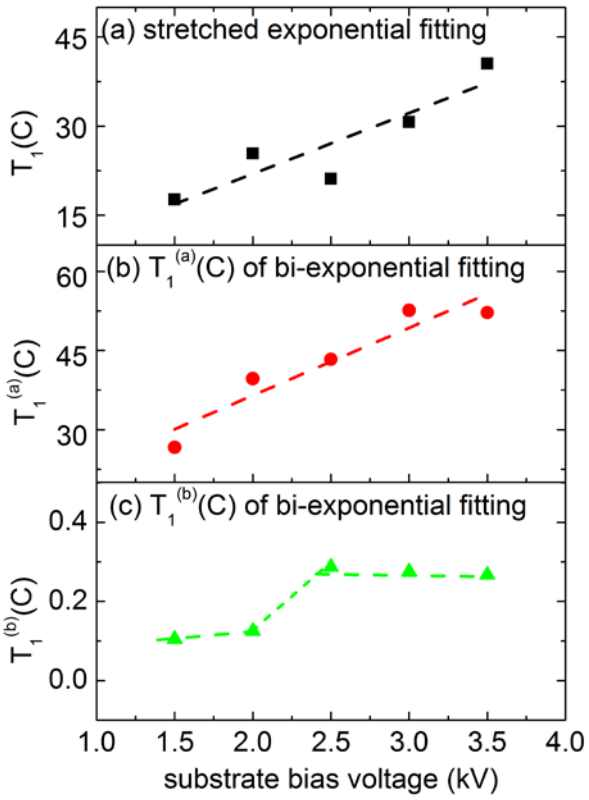

Figure 5.13 The spin-lattice relation time of ^{1}H determined by bi- and stretched exponential fitting as a function of substrate bias voltage.

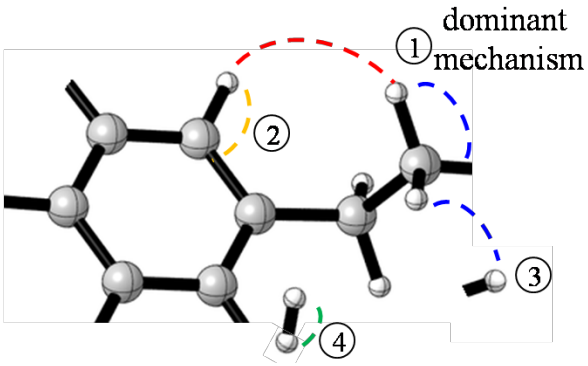

Figure 5.14 The illustration of possible relaxation mechanisms of ^{1}H spins in a-C:H coating.

In like manner not simply focusing on the specific values of MSE and R-sq(adj) obtained by using distinct fitting formulas, both the ultra short component T_1^b(H) given by bi- exponential formula and the small value of α approaching 0.5 given by stretched exponential formula suggest a very strong stretched relaxing behavior of some part of ^{1}H spins. To throw additional light on the ultra quick-relaxing ^{1}H spins,

a ^{13}C saturation recovery sequence followed by CPMAS after an interval of T_1^a(H) and T_1^b(H) (i.e. saturation recovery sequence – relaxing interval – 90° single pulse – CP with contact time of 5 ms – proton-decoupled acquisition, short for "interrupted saturation recovery") was designed. Particularly, as the relaxing interval is T_1^b(H), only the ^{13}C spins in interaction with ultra-fast relaxing ^1H spins can be detected. In Fig. 5.14, ^{13}C spectra (5) and (6) describe the interrupted saturation recovery spectra with relaxing interval as T_1^a(H) and T_1^b(H), respectively, in comparison with (1) the ^{13}C MAS spectra without ^1H decoupling, (2) CPMAS spectra with a contact time of 5 ms, (3) and (4) interrupted saturation recovery spectra with an relaxing interval of 300 ms and 150 ms, respectively. All these spectra were obtained after 10000 acquisition scans. Specifically in spectra (1), the sp^3 C peak center shifted to 57 ppm due to the un-decoupled heteronuclear interaction between ^{13}C and ^1H spins, while the shoulder peak of sp^2 C′ sites still appeared around 105 ppm. By comparison, in spectra (2)~(6), the shoulder peak disappeared because of the application of CP technique with moderate duration of contact time. More importantly, in spectra (6) the peak intensity of ^{13}C spins in coordination with ultra-quick relaxing ^1H spins were quite weak due to

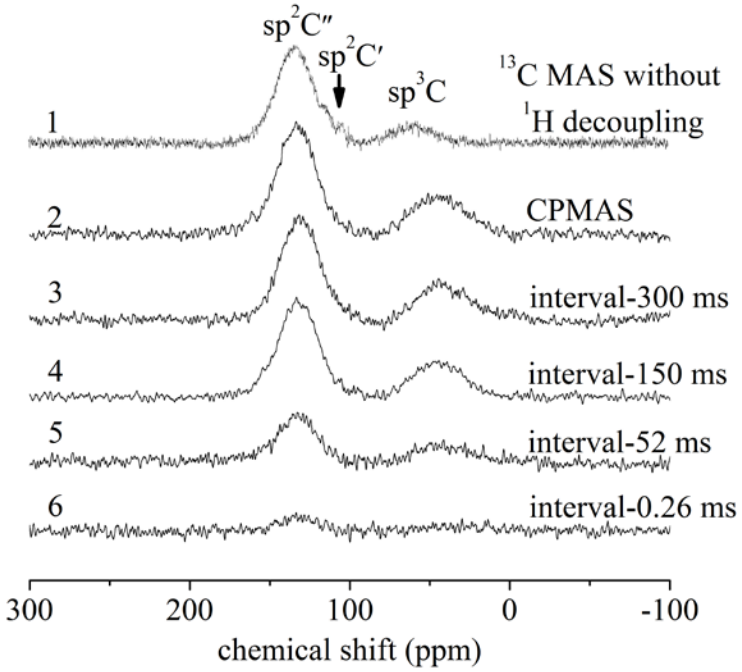

Figure 5.15 The ^{13}C spectra of B3.5 fragment: (1) ^{13}C MAS spectra without ^1H decoupling, (2) CPMAS spectra with a contact time of 5 ms, (3) saturation recovery spectra with an interval of 300 ms, (4) saturation recovery spectra with an interval of 150 ms, (5) saturation recovery spectra with an interval of 52 ms, (6) saturation

recovery spectra with an interval of 0.26 ms.

their low fractions, and obviously exhibited a preferential distribution in regions of sp^2 C″ clusters. As the relaxing interval was larger than T_1^a(H), the spectra (3)~(5) showed a similar peak shape and $sp^3/(sp^3+sp^2)$ ratio, suggesting that almost all the ^{1}H spins could fully relax during T_1^a(H) interval, and the normal relaxing ^{1}H spins distributed relatively homogeneously in studied coatings.

5.3.4 Cluster size of sp^2 C a-C:H coating

To classify the development of sp^2 C cluster size with an increase of bias voltage, two effective indicators, i.e. Raman spectra and optical band gap have been highlighted in this section [15-26]. As we know, the optical gap of perfectly sp^3 hybridized carbon like diamond and sp^2 hybridized carbon like graphite is 5.5 eV and 0 eV, respectively; consistently, the Raman spectra of diamond and graphite are obviously different, showing a confined peak center around 1580 cm^{-1} and 1332 cm^{-1}, respectively. By comparison, the a-C:H coatings hybridized by a combination of sp^2 and sp^3 C in amorphous manner generally exhibit a optical gap within 0.5 eV~5.5 eV and Raman spectra composed of G and D peaks centering around 1580 cm^{-1} and 1350 cm^{-1}, respectively [15]. In previous reports typically presented by Robertson and Ferrari [15, 16], the close correlations between optical gap and Raman *I(D)/I(G)*, as well as Raman G peak position has been intimately investigated, and a threshold value of grain size for these correlations was proposed [15, 16]. Specifically, as the grain size of graphite is smaller than 2 nm, the Raman *I(D)/I(G)* is proportional to the increase of L_a in description of Eq. (5.6), while as the grain size exceeds 2 nm, the Raman *I(D)/I(G)* is inversely proportional to the further increase of L_a as described by Tuinstra-Koenig relationship (Eq. (5.7)) [15]. In fact, for plasma-deposited a-C:H coatings, the Raman *I(D)/I(G)* is proportional to L_a, i.e. the average grain size of graphitic clusters in amorphous carbon network is generally below 2 nm. Meanwhile, when the grain size is below the threshold value, the Raman G peak positions generally shifts to higher wavenumber with an increase of L_a, which is similar to the increasing tendency of Raman G peak position and *I(D)/I(G)* of studied a-C:H coating as the bias voltage increases from 0.5 kV to 3.5 kV (see in Figure 3.8). Thus, we may infer that in the whole range of bias voltage within 0.5~3.5 kV, the average size of sp^2 clusters grows continuously with an increase of ion energy, yet below the threshold size and can hardly be observed by SEM and TEM.

$$I(D)/I(G) = C(\lambda)L_a{}^2 \qquad (5.6)$$

$$I(D)/I(G) = C(\lambda)/L_a \qquad (5.7)$$

Particularly as regard to the strong dependence of optical gap on sp^2 cluster size, Figure 5.16 explains the mechanism in view of the configuration of π states in a-C:H coating. The σ bonds of all the carbon bonds and C-H bonds form occupied σ states in valence band and empty σ* states in conduction band, separated by a wide σ-σ* gap, while the localized π bonds of sp^2 sites form filled π states and empty π* states with a narrow π-π* gap [1-5], so that the value of Tauc gap is roughly equal to the half of $2E_\pi$. While the optical gap of crystal is defined as the minimum energy gap between occupied and empty states, the optical gap of amorphous carbon is arbitrarily determined as the photon energy under which the optical absorption coefficient α reaches 10^4 cm^{-1} (i.e. E_{04} gap), or determined by the extrapolation of $(\alpha E)^{1/2}$ curve in relation with photon energy as α=0 (i.e. Tauc gap). As a result, the optical gap of a-C:H coating is determined by the average band gap of localized π and π* bands in sp^3 matrix.

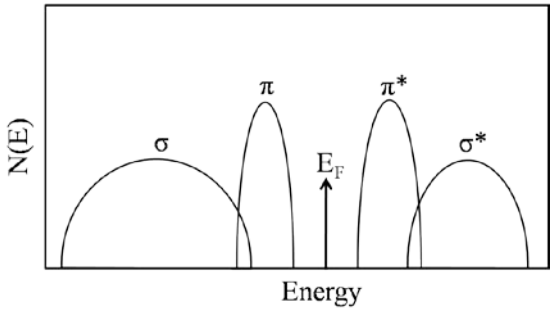

Figure 5.16 The schematic DOS of a carbon at σ and π state.

According to Robertson and O'Reilly's calculation [1], amorphous carbon coating consists of small planar network of fused 6-fold graphitic clusters containing only sp^2 C, and the crosslink between these clusters by sp^2 or sp^3 bonding allow the formation of extended carbon network. Maximizing the π bond energy tends to cause a segregation between sp^2 and sp^3 sites, so that sp^2 sites form localized π bonded clusters in sp^3 bonded matrix [23, 24]. Then, the optical gap of individual sp^2 cluster is inversely proportional to the number of aromatic rings contained in one cluster, as described by Eq.(5.8):

$$E_g = 2\gamma / N^{1/2} = 2\gamma(a/L_a) \qquad (5.8)$$

in which γ is the $pp\pi$ interaction, N the number of aromatic rings in individual cluster,

a the lattice spacing, L_a the in-plane correlation length, i.e. the grain size of graphite. Assuming that the optical gap of sp^2 clusters is a function of inter-distance and width of π-π* band gap, as shown in Figure 5.22 [15, 25, 26], Robertson presented a model of optical transition in which sp^2 sites have variable gap depending on the configuration of each sp^2 cluster, and sp^3 matrix acts as tunnel barriers between each sp^2 cluster. The difference between band gaps of sp^2- and sp^3- bonded regions causes large fluctuations in local band gap, thus produces mobility gap E_μ. The local gap of π states varies inversely with cluster size, while the band gap of σ states is roughly about 5.5 eV. The optical band edges E_{opt} is just determined by the density of states $N(E)$ and primarily varies with cluster size distribution, while the mobility edges is additionally dependent on the width of sp^3 barriers. Widening sp^3 barriers will force mobility edges further into the bands beyond optical band edges.

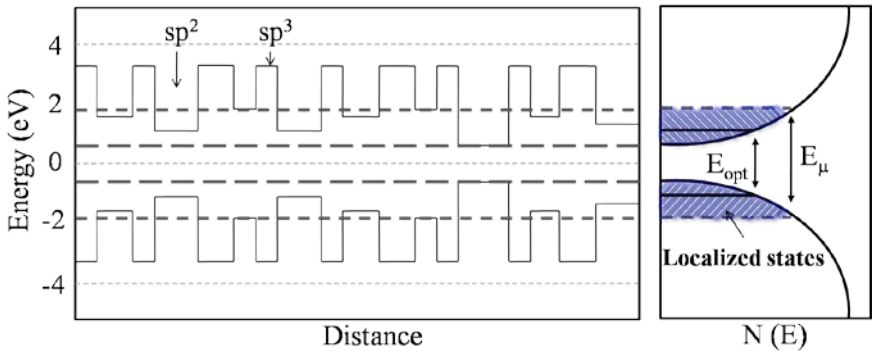

Figure 5.17 The variation of local band gap with distance in cluster model [15].

However, other researchers [27] pointed out that Eq.(5.8) may make an overestimation on the size of single-planar sp^2 cluster, because as the increase of deposition bias voltage, the coming ion species with higher energy can easily remove one carbon atom from 6-fold rings and significantly reduce the effective size of planar clusters. M. A. Tamor et al. [12] argued that the electronic and optical properties of highly imperfect-ordered amorphous carbon coating are dominated by the property of individual clusters, and the optical gap of an individual cluster is determined by the lowest π-π* transitions primarily associated with cluster edges. Also, M. Chhowalla et al. [13] presented that optical gap is both determined by the cluster size and local distortions of sp^2 bonding, rather than the nature of surrounding matrix or hydrogen content.

In this thesis, the E_{04} gap and Tauc gap of ion-vapor deposited a-C:H coatings were determined on basis of Tauc equation in Eq.(5.1), and Fig. 5.18 describes the

UV/VIS/NIR transmission spectra of studied coatings deposited at various bias voltages. Also, Fig. 5.19 plots the absorption coefficient curve as a function of photon

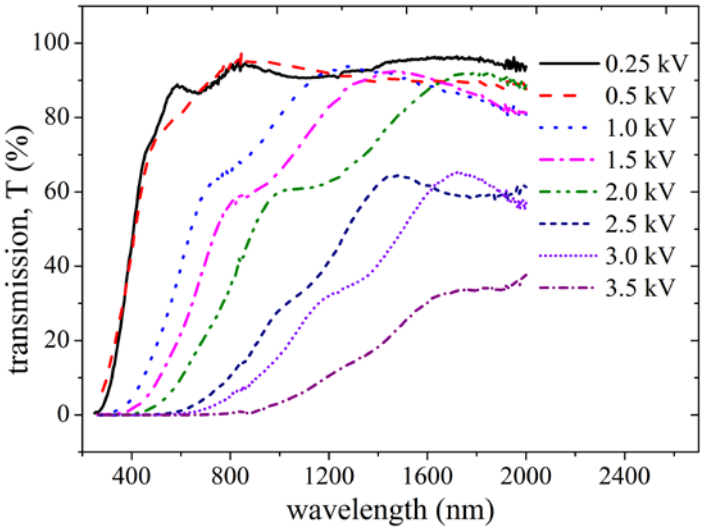

Figure 5.18 The transmission of a-C:H coatings deposited under various bias voltages.

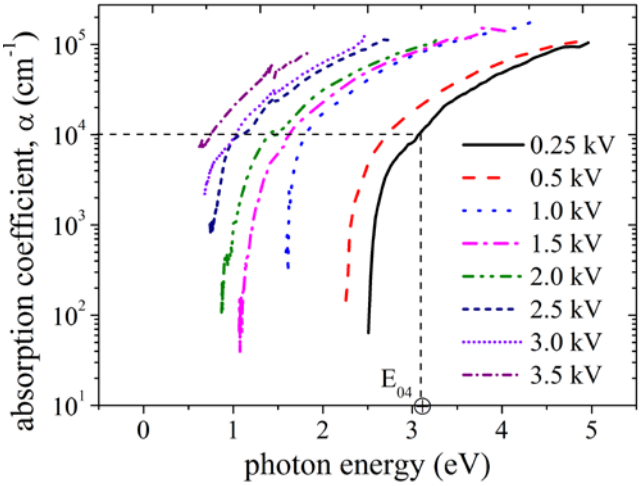

Figure 5.19 The absorption coefficient α of a-C:H coatings deposited under various bias voltages.

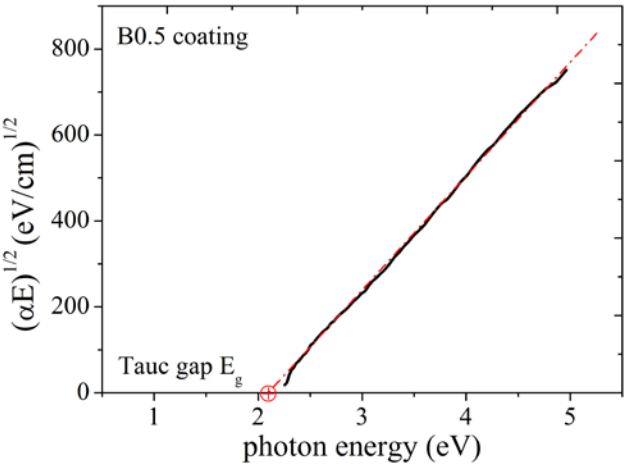

Figure 5.20 The acquisition of Tauc gap E_g through the extrapolation of linear part of $(\alpha E)^{1/2}$ curve at α=0 by using Tauc equation.

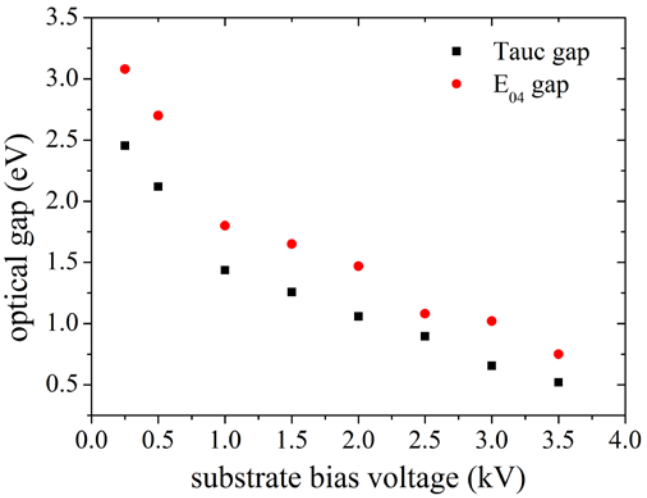

Figure 5.1 The Tauc gap E_g and E_{04} gap (as α=10^4 cm^{-1}) of a-C:H coatings deposited under various bias voltages.

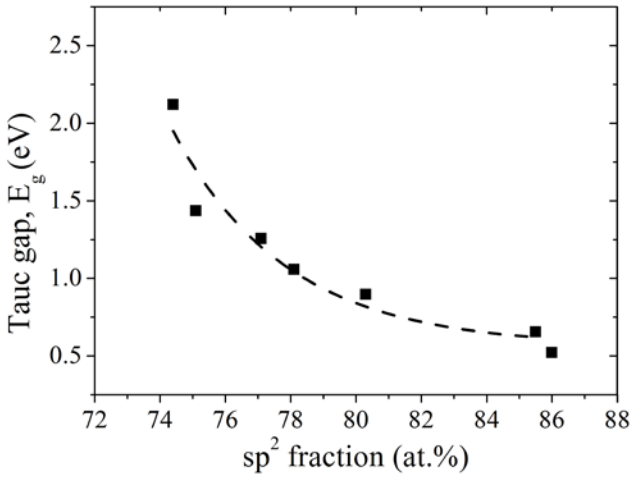

Figure 5.22 The Tauc gap E_g of a-C:H coatings as a function of sp^2 fraction.

energy, so that the E_{04} gap of each coating could be obtained. Taking B0.5 coating as an example, Fig. 5.20 shows the determination of Tauc gap E_g as the extrapolated intercept of the liner part of $(\alpha E)^{1/2}$ curve, and Fig. 5.21~Fig. 5.22 display the determined Tauc gap as a function of substrate bias voltage and the total fractions of sp^2 sites, respectively. Consistent with the reports of plasma-deposited a-C:H coating [12-15], the optical gap of ion-vapor deposited coating reduces monotonically with an increase of bias voltage and the sp^2 fraction [15], but shows no clear correlations with the presence of boundary sp^2 C' sites around sp^2 C" clusters. Thus, this tendency of optical gap is primarily attribute to the medium range order of sp^2 clusters in

amorphous carbon network. The growth of bias voltage has continuously shortened the inter-distance of sp^2 clusters for larger cluster size and narrower sp^3 barriers, so that the density of states *N(E)* around Fermi level E_F is continuously increasing for the shortening width of π-π* band gap, and both the band gap edges E_{opt} and mobility gap E_μ are approaching to the band gap of π states.

5.4 Conclusions

In this chapter, heterogeneous structure of ion-vapor deposited a-C:H coating is deeply discussed. In light of the shoulder peak centering around 105 ppm in ^{13}C MAS spectra and its absence in CPMAS spectra, we found that there are two distinct types of sp^2 sites in studied coating: one type of them denoted as sp^2 C′ in fraction of 3~12 at.% is non-protonated and specifically localized in hydrogen-absent regions, while the other dominant type denoted as sp^2 C″ was hydrogenated or at least proximate to ^1H spins. On basis of the consistent tendency of sp^2 C′ fraction and Raman parameters as a function of bias voltage within 0.5 kV~3.5 kV, one model of sp^2 C clustering configurations is proposed that sp^2 C′ sites are specifically embedded between graphite-like sp^2 C″ clusters and amorphous sp^3 C matrix as trapped interfaces or boundaries where the sp^2 carbon bonds were highly distorted. A continuous increase of bias voltage above 2 kV would promote the integration and re-ordering of graphite-like sp^2 C″ clusters, and thus results in a marked decrease of boundary sp^2 C′ sites.

Further exponential fitting analysis on the magnetization relaxation behavior of sp^2 C″, sp^2 C′ and sp^3 C revealed that the magnetization recovery of sp^2 C″ exhibited a typical stretched-exponential approximation with stretched power α equal 0.8 and T_1 equal 2.8 s, while the sp^2 C′ showed a single-exponential approximation with T_1 equal 5 s for its hydrogen-free characters, and sp^3 C showed a weaker single-exponential approximation with T_1 equal 3.7 s. The difference of T_1 value among sp^2 C″, sp^2 C′ and sp^3 C proved the existence of distinct sp^2 clusters in studied a-C:H coatings, and the stretched-exponential approximation of sp^2 C″ indicated a prominent presence of paramagnetic centers. For ^1H spins, their magnetization recovery showed a better bi-exponential approximation, giving a long T_1(H) component fluctuating within 25~55 ms in content of 70%~80% and a short T_1(H) component fluctuating within 0.1~0.3 ms in content of 30%~20% for various bias voltages. The interrupted ^{13}C saturation recovery with an interval of short T_1(H) component showed that most of quick-

relaxing protons were localized nearby sp^2 C″ clusters. Such a short T_1(H) was only possibly resulted from a relaxation mechanism associated with electron-nuclear interactions, and its partial distribution in sp^2 C″ clusters may imply more complex configurations of unpaired electrons in studied a-C:H coatings.

Besides, the development of sp^2 cluster size with an increase of bias voltage was studied through the investigation on optical property of studied coating, and the results showed a monotonic decreasing tendency of E_g and E_{04} with the increase of bias voltage and sp^2 fraction. Such a tendency of optical gap is primarily attribute to the continuously growing size of sp^2 clusters, while the presence of boundary sp^2 C' sites around sp^2 C" clusters imposed weak influence on this correlation.

References

[1] J. Robertson, E.P. O'Reilly. Electronic and atomic structure of amorphous carbon. Phys. Rev. B. 35, 2946-2957 (1987)

[2] R. U. A. Khan, J. D. Carey, S. R. P. Silva, B. J. Jones, R. C. Barklie. Electron delocalization in amorphous carbon by ion implantation. Phys. Rev. B. 63, 121201(R)

[3] J. D. Carey, S. R. P. Silva. Disorder, clustering, and localization effects in amorphous carbon. Phys. Rev. B. 70, 235417 (2004)

[4] G. Fanchini and A. Tagliaferro. Disorder and Urbach energy in hydrogenated amorphous carbon: a phenomenological model. Appl. Phys. Lett. 85, 730-732 (2004)

[5] A. Ilie, A. C. Ferrari, T. Yagi, J. Robertson. Effect of sp^2-phase nanostructure on field emission from amorphous carbons. 76, 2627-2629 (2000)

[6] A. M. Panich. Nuclear Magnetic Resonance Studies of Nanodiamonds. Critical Reviews in Solid State and Materials Sciences. 37, 276 - 303 (2012)

[7] A. M. Panich, G. B. Furman. Nuclear spin-lattice relaxation and paramagnetic defects in carbon nanomaterials. Diam. Rel. Mater. 23, 157-161 (2012)

[8] C. Jäger, J. J. Titman, R. J. Newport. Detection of structural heterogeneity in amorphous-C:H films by NMR. Thin Solid Films. 227, 3-6 (1993)

[9] C. Jäger, J. Gottwald, H. W. Spiess, R. J. Newport. Structural properties of amorphous hydrogenated carbon. III. NMR investigations. Phys. Rev. B. 50, 846-852 (1994)

[10] Gyunggoo Cho, Bing K. Yen, Christopher A. Klug. Structural characterization of sputtered hydrogenated amorphous carbon films by solid state nuclear magnetic resonance. J. Appl. Phys. 104, 013531 (2008)

[11] R. Blinc, D. Arčon, P. Cevcy, I. Pocsikz, M. Koos, Z. Trontelj, Z. Jagličič. ^{13}C nuclear magnetic resonance and electron spin resonance of amorphous hydrogenated carbon. J. Phys.: Condens. Matter. 10, 6813–6824 (1998)

[12] M. A. Tamor, J. A. Haire, C. H. Wu, K. C. Hass. Correlation of the optical gaps and Raman spectra of hydrogenated amorphous carbon films. Citation: Appl. Phys. Lett. 54, 123-125 (1989)

[13] M. Chhowalla, J. Robertson, C. W. Chen, S. R. P. Silva, C. A. Davis, G. A. J. Amaratunga, W. I. Milne. Influence of ion energy and substrate temperature on the optical and electronic properties of tetrahedral amorphous carbon (ta-C) films. J. Appl. Phys. 81, 139-145 (1997)

[14] Debabrata Pradhan, Maheshwar Sharon. Opto-electrical properties of amorphous carbon thin film deposited from natural precursor camphor. Appl. Surf. Sci. 253, 7004-7010 (2007)

[15] J. Robertson. Diamond-like amorphous carbon. Mater. Sci. Eng., R. 37, 129-281 (2002)

[16] A. C. Ferrari, J. Robertson. Interpretation of Raman spectra of disordered and amorphous carbon. Phys. Rev. B. 61, 14095-14107 (2000)

[17] J. Choi, K. Ishii, T. Kato, M. Kawaguchi, W. Lee. Structural and mechanical properties of DLC films prepared by bipolar PBII&D. Diam. Rel. Mater. 20, 845–848 (2011)

[18] R. C. Barklie. Characterisation of defects in amorphous carbon by electron paramagnetic resonance. Diam. Rel. Mater. 12, 1427-1434 (2003)

[19] A. Abragam. The Principles of Nuclear Magnetism. Oxiford: Oxiford University Press, 1960, p. 378-389

[20] F. Rabbani, B. M. Vogelaar. The importance of unbound hydrogen and increased aromatic structure on the friction and wear behavior of amorphous hydrogenated carbon (a-C:H) coatings. Diam. Rel. Mater. 13, 170–179 (2004)

[21] X. A. Mao. An empirical criterion for estimating T_1 error. Appl. Magn. Reson. 4, 261-264(1993)

[22] A. Abragam. The Principles of Nuclear Magnetism. Oxiford: Oxiford University Press, 1960, p. 378-389

[23] J. Robertson. Structural models of a-C and a-C:H. Diam. Rel. Mater. 4, 297-301 (1995)

[24] J. Robertson. Recombination and photoluminescence mechanism in hydrogenated amorphous carbon. Phys. Rev. B. 53, 16302 (1996)

[25] J. Robertson. π-bonded clusters in amorphous carbon materials. Philos. Mag. B. 66, 199 (1992)

[26] C. W. Chen, J. Robertson. Nature of disorder and localization in amorphous carbon. J. Non-Ctys. Solids. 227-23-, 602-606 (1998)

[27] A. Erdemir. Genesis of superlow friction and wear in diamondlike carbon films. Tribo. Inter. 37, 1005-1012 (2004)

[28] R. A. Street. Hydrogenated Amorphous Silicon. Cambridge University Press. Cambridge, 1991

6 Tribological property and wear mechanism of a-C:H coating

6.1 Introduction

In addition to the optical property, the tribological property of a-C:H coating has also attached intensive research interesting due to their promising potential as alternative solid lubricants in various industrial applications [1-3]. As regard to the wear mechanism of a-C:H coatings, the work groups of Erdemire [4-7] and Donnet [8-12] had investigated the significant role of hydrogen atoms in super-low friction performance by controlling the hydrogen fraction in coating composition and sliding atmosphere, and presented a low-friction model on basis of the "hydrogen passivation" effects on contact surfaces. Meanwhile, the work group of Scharf and Singer [13-18] had made progress on the investigation of transfer layer by developing an *in-situ* Raman spectroscopy detection system, and analyzed the tribochemical generation of the friction-induced interfacial layers during sliding. Besides, some other wear mechanisms were discovered by varying the atmosphere humidity [19-21], loading conditions, sliding velocity and vacuum pressure [22, 23].

Actually, the wear mechanism of a-C:H coating varies sensitively from deposition techniques and sliding conditions, so that none of the well-known mechanism can explain the complex friction behavior of all types of a-C:H coatings perfectly. Specifically, the "hydrogen passivation" mechanism tends to favor the PECVD a-C:H coating with hydrogen content higher than 30 at.% and sliding in dry hydrogen atmosphere [4-12]. In this case, the contact surfaces are fully bonded by hydrogens diffused from inner side of coating or from external hydrogen atmosphere. However, for a-C:H coatings with medium or lower content of hydrogen and sliding in humid atmosphere or with presence of oxygen molecular, the tribochemical reactions between tribopairs and surrounding atmosphere becomes more complicated. In this case, both the graphitization and oxidation of contact surface should be carefully concerned, together with the important role of transfer layer produced between the tribopairs.

In this chapter, the wear mechanism of ion-vapor deposited coating were investigated by sliding in ambient air and artificial atmospheres such as dry N_2 and H_2. and both the role of friction-induced transfer layer and hydrogen passivation are discussed.

6.2 Experimental details

6.2.1 Friction performance in N_2 atmosphere and ambient air

At first, the friction performance of B0.5~B3.5 a-C:H coatings in ambient air and N_2 atmosphere at room temperature was investigated by applying a standard CSM ball-on-plate tribometer with two opened testing chambers, including an outer chamber and an inner chamber as illustrated by Fig. 6.1. During the sliding tests in N_2 atmosphere, the partial pressure of N_2 in inner chamber was effectively controlled by varying the exhaust durations of the inner chamber within 10~20 minutes before sliding and the gas flow rate within 2~6 NL/min during sliding tests. Well polished ISO 4957 100Cr2 (JIS SUJ-2, hardness 8 GPa, Young's modulus 210 GPa, *Ra*=10 nm) steel balls in diameter of 6 mm was used as stationary counterparts, and approximately made a Hertz contact pressure of 0.6 GPa under 5 N normal load. Detailed chemical composition of 100Cr2 steel is shown in Tab. 6. 1. Circle tracks in radius of 3.5 mm were generated on studied coatings at a sliding velocity of 15 cm/s always in one direction. After tribotests, tribopairs were separated and the wear marks formed on steel balls and a-C:H coatings were probed by an optical spectroscopy separately. Assuming that the wear scars formed on steel balls are flat and circular, the wear rate of ball was geometrically evaluated on basis of the radius data of wear scar.

Also, in order to confirm the chemical transformation of contact surfaces after sliding tests, both the wear marks formed on coating and ball sides were characterized by visible Raman spectroscopy with 0.5 mW laser power of 532-nm wavelength (doubling-Nd-YAG). Due to the rough surface of worn surfaces on counterparts, the diameter of laser spot was reduced less than 10 μm to focus on rough surface during acquisitions well.

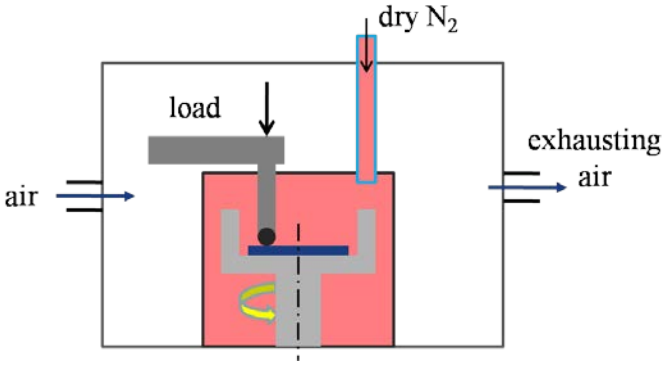

Figure 6.1 An illustration of standard CSM ball-on-plate tribometer.

Table 6.1 Chemical composition of bearing steel 100Cr2 (except for Fe)

C	Si	Mn	Cr	P	S	Mo	Ni	Cu
0.95-1.10	0.15-0.35	≤0.50	1.30-1.60	≤0.025	≤0.025	≤0.08	≤0.25	≤0.25

6.2.2 Overlapping tribo-tests in ambient air

Particularly, in order to investigate the effects of transfer layer on tribological performance of studied coatings in ambient air, tribo-tests were performed in an overlapping pattern, namely all the sliding tests were started from the first cycle by using a new ball and new a-C:H coated plate and continued for various number of sliding cycles, i.e. N={1, 5, 45, 681, …, 2274, 4547, 11368, 45473, 68209}, correspondingly d={0.022 m, 0.044 m, 0.11 m, 5 m, …, 50 m, 100 m, 250 m, 1000 m, 1500 m} under the same sliding condition, where N was the number of sliding cycles, d the sliding distance. The CoF curve (as a function of sliding cycles expressed as $f(N)$) of the longest duration test, i.e. $f(N=68209)$ was compared with { $f(N=1)$, $f(N=5)$,…, $f(N<68209)$} for the confirmation of data repeatability. Additionally, except for the afore-concerned samples B1.5 and B2.0 coatings, another two coatings deposited under 0.4 Pa with a bias voltage of 1.5 kV and 2.5 kV (denoted as C1.5 and C2.5) were tested for comparison. More detailed parameters on the mechanical property and Hertz contact pressure of these four tribo-tested samples are provided in Tab. 6.2 and Tab. 6.3. At least 9 couples of coating/steel tribopairs were used in the overlapping tribotests for one coating. After tribotests, tribopairs were separated and the wear marks formed on steel balls and a-C:H coatings were probed separately, and the wear rate of ball was geometrically evaluated as before. Additionally, white light interferometer (WLI) and atomic force microscopy (AFM) were also employed to observe the wear marks in the scale of nanometer.

Table 6.2 Deposition parameters and properties of a-C:H coatings.

tested coatings	thickness (nm)	hardness (GPa)	Young's modulus (GPa)	roughness Ra (nm)	hydrogen (at.%)
B2.0	945	16.30	160.60	0.245	20
B1.5	810	14.40	189.76	0.138	22
C1.5	1760	18.06	180.54	0.247	21
C2.5	2400	16.93	176.58	0.135	19

Table 6.3 Hertz-contact parameters of a-C:H coating /steel ball counterparts.

tested coatings	theoretical radius of contact (μm)	P_{max} (MPa)
B2.0	53.41	634.7
B1.5	51.79	674.7
C1.5	52.26	662.8
C2.5	52.49	657.5

6.2.3 Chemical characterization of transfer layer produced in ambient air

To make a comparative investigation on the chemical structure of transfer layers produced in ambient air, the XPS C 1s, O 1s and Fe 2p3/2 spectra of transfer layers were acquired by a PHI Quantera II system which used monochromatic Al (Kα) X-ray radiation with photon energy of 25 KV as the light source at a square area of 100×100 μm^2. The XPS testing chamber was vacuumed less than 1.0×10^{-6} Pa. Since the worn balls exposed in ambient air can easily be contaminated by physisorbed moistures after tribotests [18, 20], a chemically layered-structure model of transfer layer formed in ambient air is presented in Fig. 6.2. According to the depth distribution of oxygen content by increasing the duration of Ar^+ pre-sputtering before XPS spectra acquisition, the physisorption layer with highest and stable content of oxygen as 50~55 at.% could be removed by one-minute pre-sputtering, revealing its thickness just as few atomic layers. By comparison, the second layer denoted as “chemisorption” with moderate content of oxygen as 30~45 at.% is produced as a result of tribochemical interaction in humid air, and strongly affects the friction behavior of carbon coatings [14, 19, 24, 25]. The second layer could be removed by three-minute pre-sputtering, revealing its thickness below 6 nm, while further sputtering would reduce the C/O content sharply down to the level as as-deposited coating, i.e. 1~3 at.%Thus, the third layer was noted as “carbon base” in Fig. 6.2, and the real detection depth of this XPS measurement was about 10 nm. Additionally, in order to clarify the effect of natural oxidation of steel ball in ambient air, an organic-solvent cleaned blank ball (labeled as N=0) previously exposed in the same ambient air atmosphere (relative humidity 25%) was also measured at the same time for comparison.

To avoid a chemical variation of meta-stable structure in transfer layer, the energy of pre-sputtering Ar^+ beam was 4 keV. While the top physisorption layer was cleaned

up, both the chemisorption layer and carbon-based layer of transfer layer were detected. The obtained XPS spectra represented the combined information on these two layers.

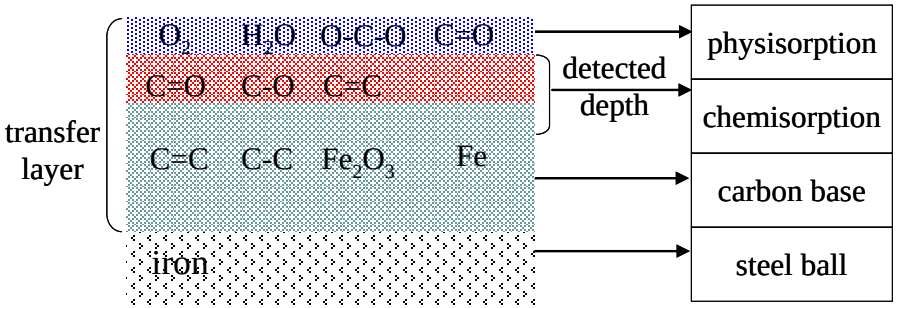

Figure 6.2 Schematic representation of the chemically layer-structured model of transfer film derived from a-C:H coating/steel ball tribopairs in ambient air.

XPS spectra were collected by an analyzer with pass energy of 140 eV for the C 1s, O 1s, Fe 2p3/2 spectra and 280 eV for surface composition survey spectra. The atomic content of each element was evaluated in terms of the area intensity under composition survey spectra. Charge-up calibration was performed by adjusting the position of C=C bond to 284.5 eV. C 1s spectra were deconvoluted to four peaks in shape of combined Gaussian and Lorentzian formulas (GL) with a Shirley background by using CasaXPS software, and the shape of Lorentzian was fixed as 20% in GL combination. According to Ref. [26-28], the binding energy of C=C peak was fixed at 284.5 eV and its full width at half maximum (FWHM) was constrained below 1.5 eV, whereas the C–C peak was fixed at 285.3 eV, and its FWHM was restricted below 2 eV. The remained part was attributed to C=O and C–O peaks with FWHM restricted below 3 eV.

6.3 Results

6.3.1 Friction behavior in N_2 atmosphere

During the sliding tests in N_2 atmospheres, the partial pressure of N_2 in inner chamber were controlled by varying the gas flow rate within 2~6 NL/min during sliding tests, and the exhaust duration before sliding was also changed within 10~20 minutes as listed in Tab. 6.4. Fig. 6.3 compares the CoF curves under six types of gaseous conditions with an increase of sliding distance, from which an optimal gaseous condition was found for lowest and steady friction coefficient (CoF) as the exhaust duration was 10 minutes at a flow rate of 2 NL/min and the testing flow rate was 2 NL/min, i.e. the 5th condition in Tab. 6.4. The spikes of CoF curves in 1st, 3th

and 6th test were attributed to the breakup of interfacial transfer layer and serious failure of underneath coating, as proved by Fig. 6.4a. In Fig. 6.4, the wear of steel balls and tested coating surfaces under 1st are obviously more serious than that of 5th condition. Clearly, it can be seen that when the exhaust duration is longer than 10 minutes, or the testing flow rate is higher than 2 NL/min (or gradually increases from 2 NL/min to 6 NL/min, i.e. 1st condition), the wear rate of tribopairs is quite high so that a-C:H coatings will be worn out quickly during the first 10 m sliding. Consistently, the CoF will increase sharply from 0.03 to 0.6 due to a complete failure of coating surface and a direct contact between steel ball and silicon substrate. It seems that both the high partial pressure and flow rate of N_2 in testing chamber, i.e. dry N_2 atmosphere, are unfavorable for the steady contact between SUJ2 sliders and ion-vapor deposited a-C:H coatings. And in this case, the quick buildup of durable transfer layer which favors the low friction and wear of tribopairs cannot be achieved without a few presence of oxygen and water molecular.

To confirm the role of few oxygen and water molecular in N_2 atmosphere for the buildup of durable transfer layer under the optimal exhausting condition, one sliding test starting under the 5th gaseous condition and continued with gradually increasing testing flow rate was conducted, and its CoF curve is described in Fig. 6.5. Interestingly, it can be found that as long as the durable transfer layer was produced at the beginning of sliding, the CoF in further sliding would be insensitive to testing flow rate, and the low-friction behavior can be maintained in dry N_2.

By applying the optimal conditions aforementioned, the CoFs of B0.5~B3.5 coatings were obtained as shown in Fig. 6.6~Fig. 6.8. In Fig. 6.6, all the CoF can be stabilized quickly within the range of 0.01~0.1 after a short running-in period, except for the spikes in B1.5~2.5 coatings which were caused by a breakup of transfer layer. After the spikes, the CoF could fall back to steady state level again due to a re-buildup of a brand-new transfer layer as seen in Fig. 6.7c~Fig. 6.7e, however, with large amount of wear debris around contact surfaces. Specifically, the inset graph of Fig. 6.6 describes the steady state CoF during 50~70 m, and the average value of CoF in this range of sliding distance is shown in Fig. 6.8 as a function of deposition bias voltage. Interestingly, it is found that B2.0 coating with highest content of sp^2 C' sites and diamond-like network shows highest steady-state CoF, and the tendency of steady-state CoF with increasing bias voltage is well consistent with the tendency of

the sp^2 C' fraction and Raman FWHM(G) as previously discussed in Sec. 5.3.1. Meanwhile, in Fig. 6.7d the wear rate of steel sliders reached to its highest level at 2.0 kV with largest radius of wear scar.

Table 6.4 Gaseous conditions of sliding tests in N_2 atmosphere.

	exhaust duration (minute)	exhaust flow (NL/min)	testing flow rate (NL/min)
1	5	6	2→4→6
2	20	2	6
3	20	2	2
4	5	2	2
5	10	2	2
6	10	2	4

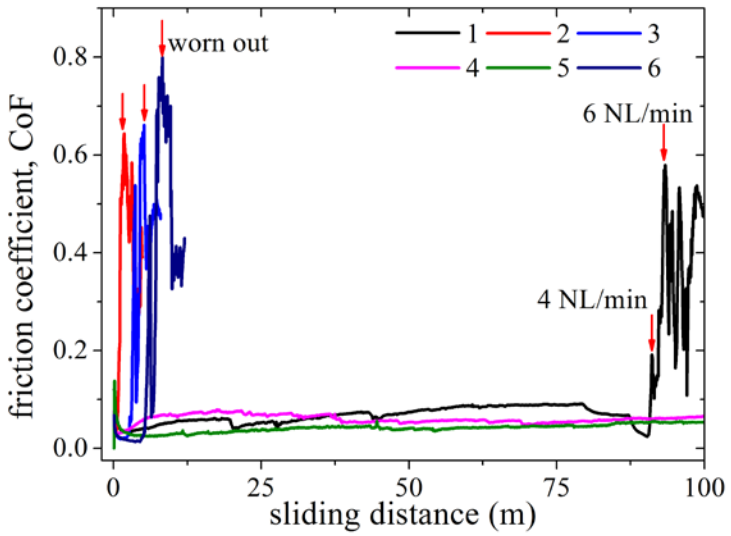

Figure 6.3 Friction coefficient of B1.0 coating in dry N_2 under various gaseous conditions.

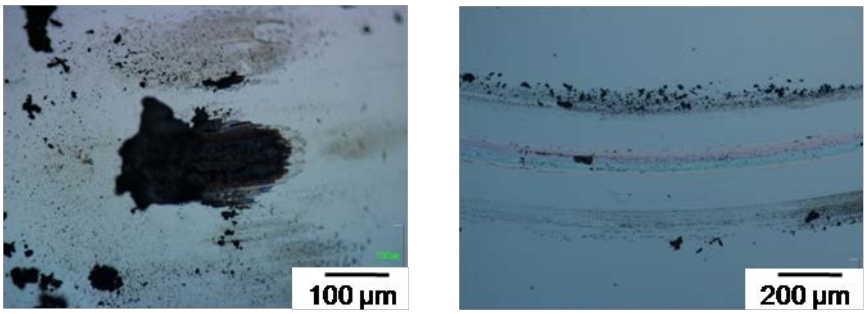

(a) under 1st gaseous condition

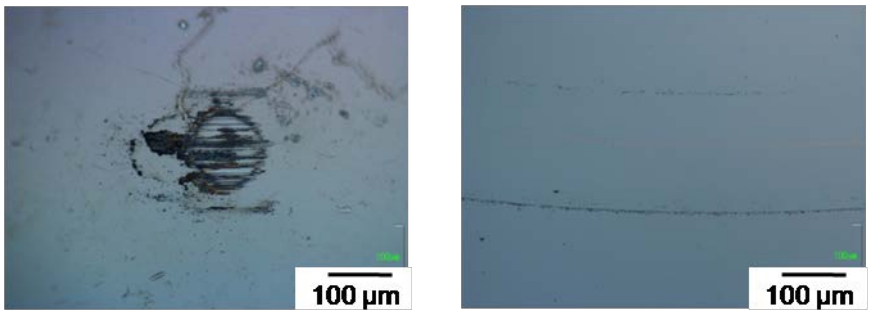

(c) under 5th gaseous condition

Figure 6.4 Optical microscopy observation of wear scars on balls and wear tracks on B1.0 coating sliding under 1st and 4th gaseous conditions.

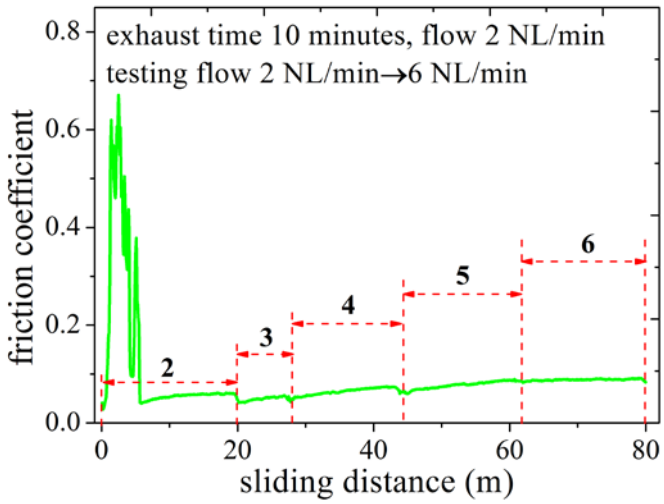

Figure 6.5 Friction coefficient of B1.0 coating in dry N_2 under the optimal exhausting condition and gradually increased testing flow rate.

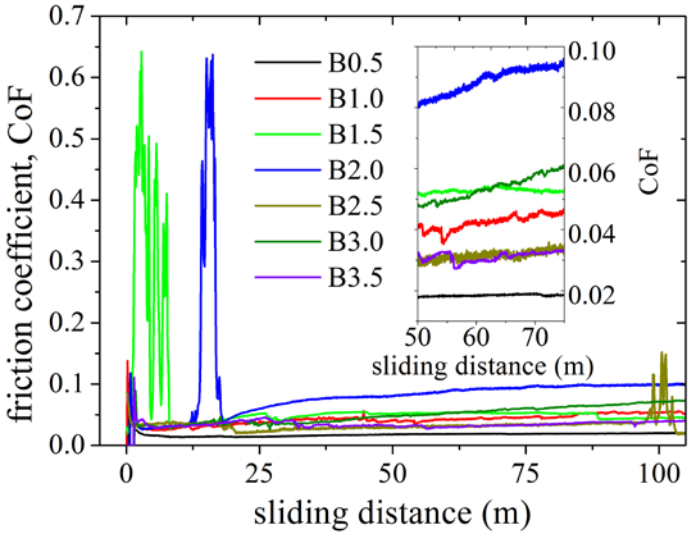

Figure 6.6 Friction coefficient curve of B0.5~B3.5 coatings in dry N_2.

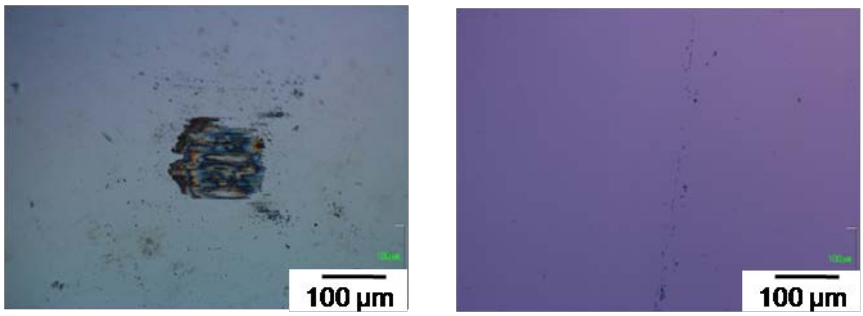

(a) B0.5 coating

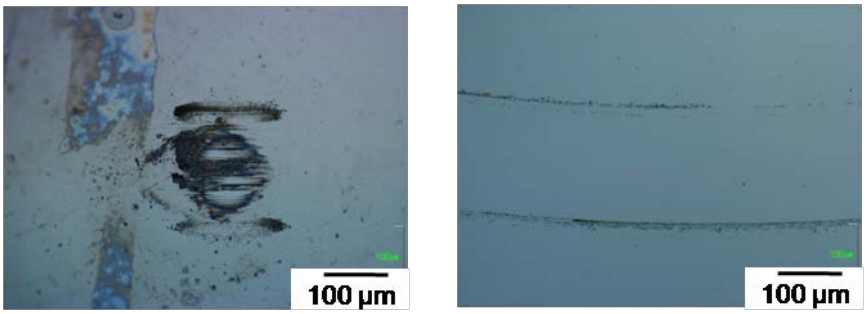

(b) B1.0 coating

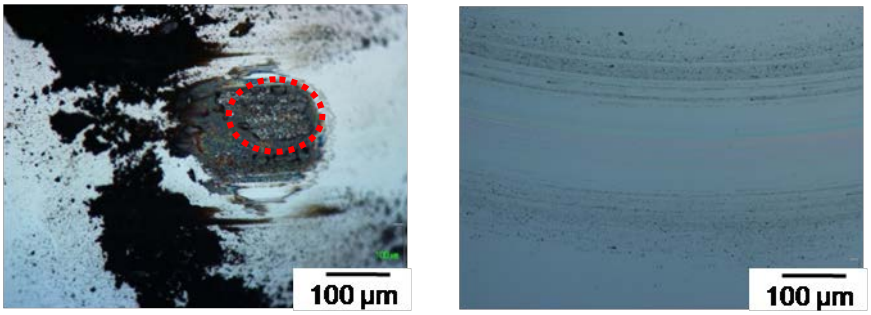

(c) B1.5 coating (detached area of transfer layer in dotted red circle)

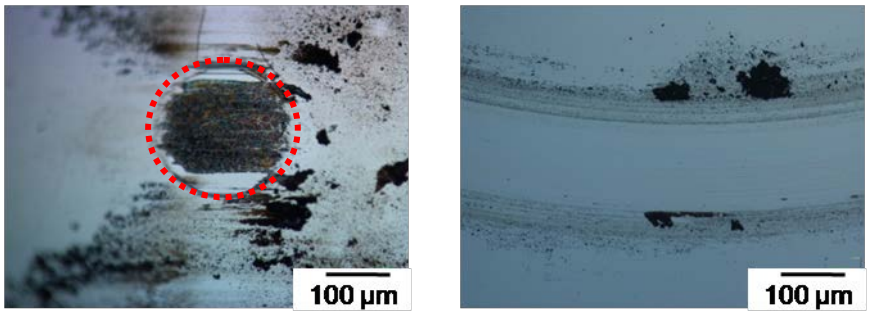

(d) B2.0 coating (detached area of transfer layer in dotted red circle)

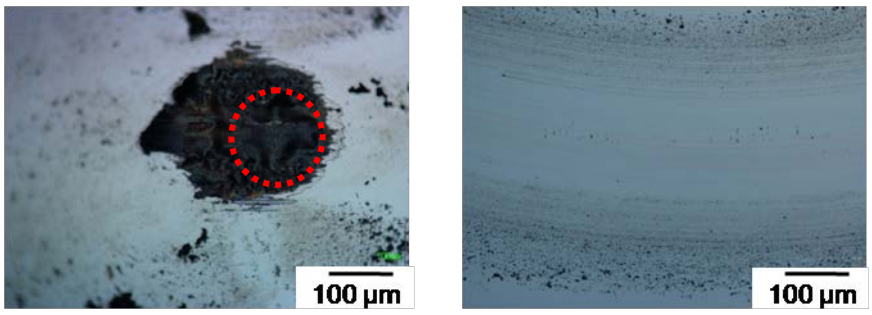

(e) B2.5 coating (detached area of transfer layer in dotted red circle)

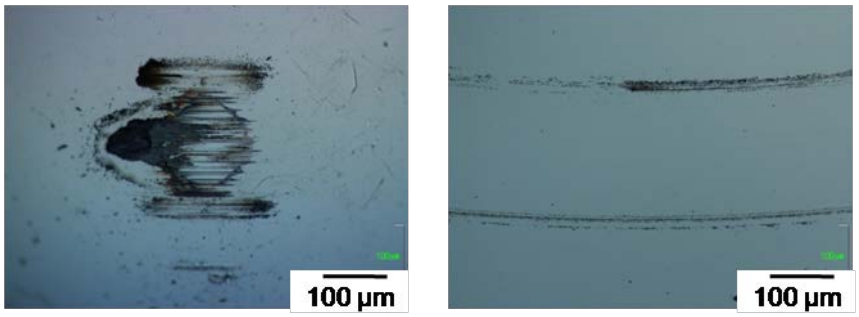

(f) B3.0 coating

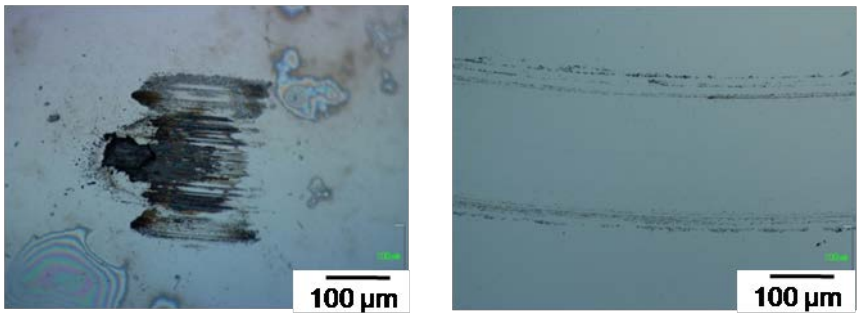

(g) B3.5 coating

Figure 6.7 Optical microscopy observation of wear scars on balls (left side) and wear tracks (right side) on tested coatings sliding in dry N_2 for 110 m (i.e.5000 cycles).

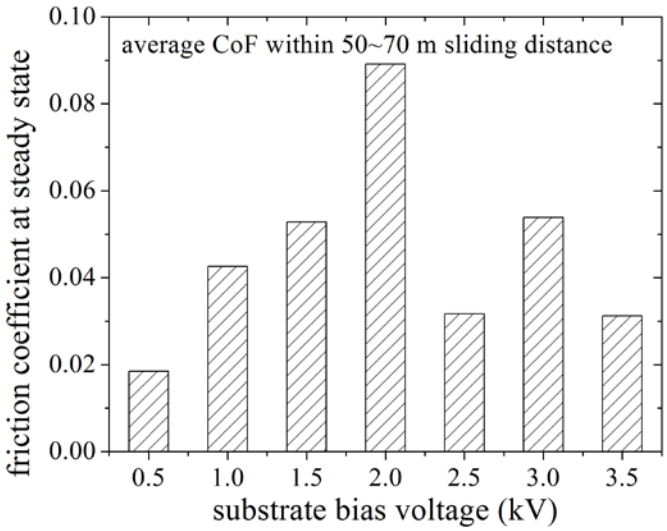

Figure 6.8 The average friction coefficient at steady state within 50~70 m sliding distance as a function of substrate bias voltage of a-C:H coatings.

6.3.2 Friction behavior in ambient air

The sliding tests in ambient air were prolonged to 1500 m, as shown in Fig. 6.9. The running-in period in ambient air prolonged as long as 300 m, and no clear steady state friction coefficient could be seen during further distance. Fig. 6.10 shows optical observation of wear marks on steel balls and tested coating surfaces after 1500 m sliding. Compared with the tribo-tests in N_2 atmosphere, the CoFs in ambient air was

much higher (generally in range of 0.1~0.4) with more serious wear as well. Meanwhile, the color of wear debris adhered around contact surfaces turned to be rusty red, implying an active tribochemical oxidation of SUJ2 balls due to the ample presence of oxygen and water molecular in ambient air. The average value of CoF during 450~1500 m sliding are in plotted Fig. 6.11, also showing relatively higher CoF in B1.0~B2.0 coatings.

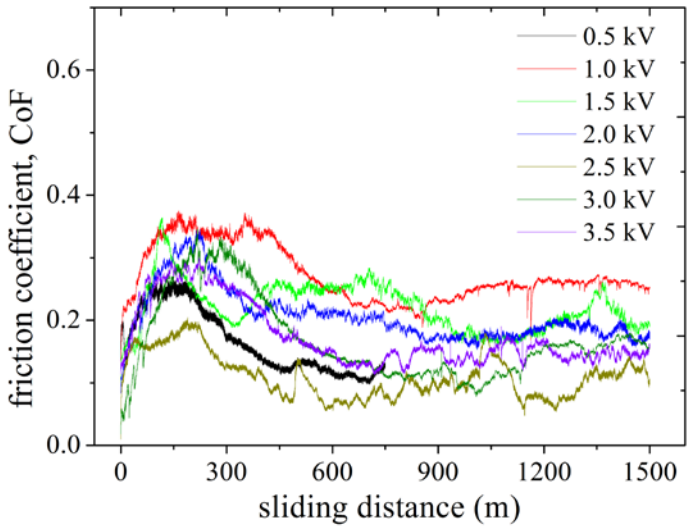

Figure 6.9 Friction coefficient of B0.5~B3.5 coating in ambient atmosphere as a function of sliding distance.

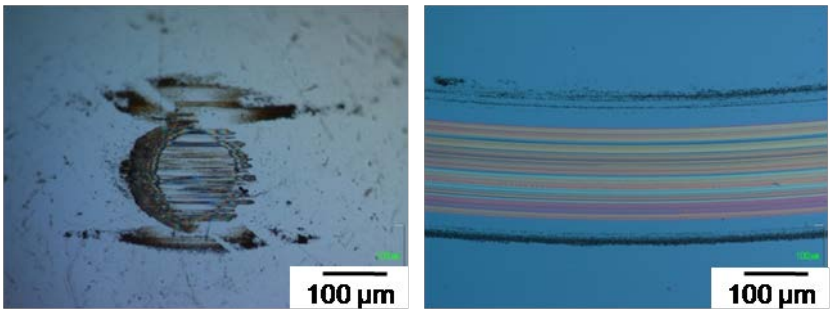

(a) 0.5 kV

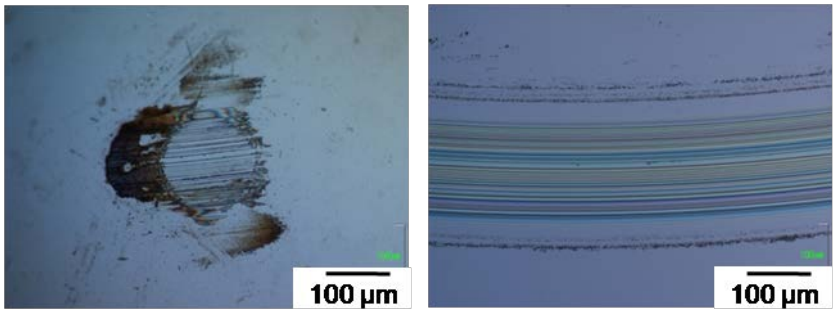

(b) B1.0 coating

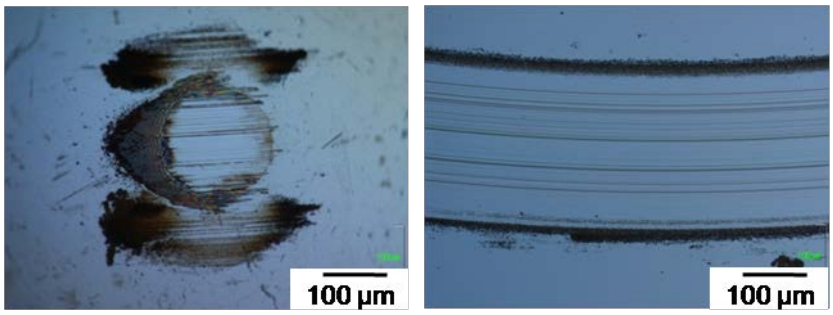

(c) B1.5 coating

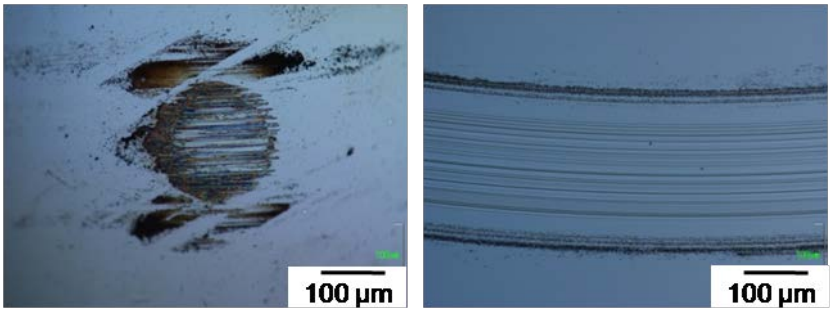

(d) B2.0 coating

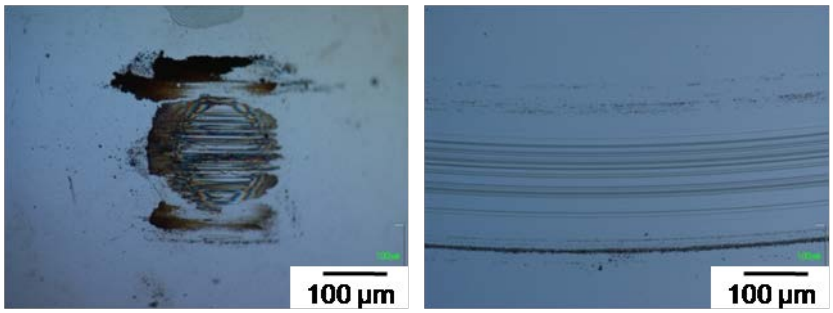

(e) B2.5 coating

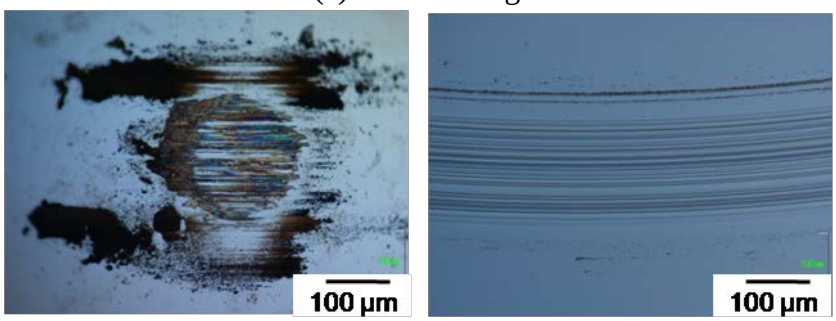

(f) B3.0 coating

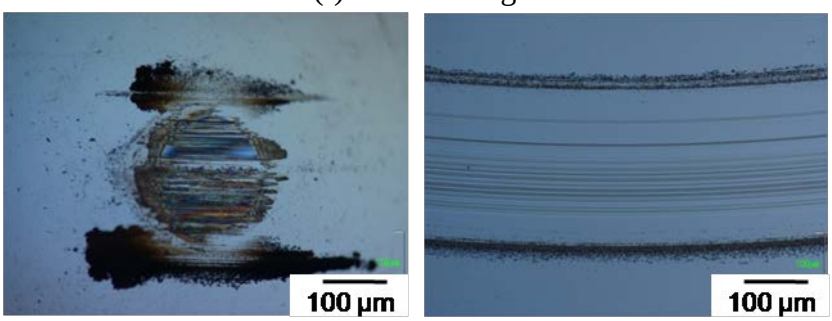

(g) B3.5 coating

Figure 6.10 Optical microscopy observation of wear scars on balls and wear tracks on tested coatings sliding in ambient atmosphere for 1500 m.

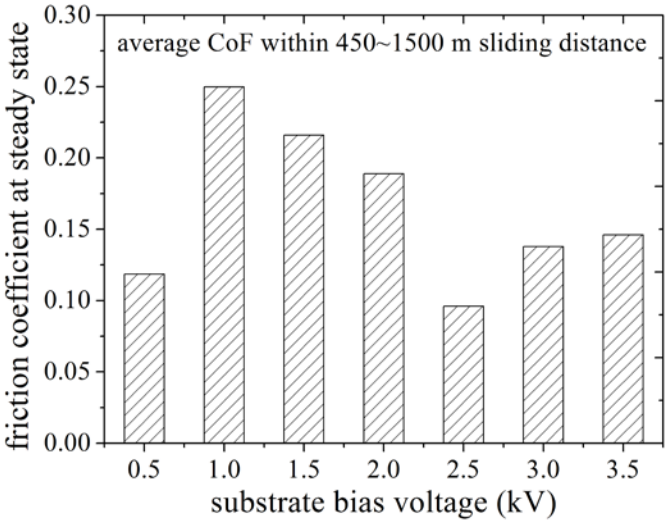

Figure 6.11 The average friction coefficient at steady state within 450~1500 m sliding distance as a function of substrate bias voltage of a-C:H coatings.

6.4 Discussions

6.4.1 Effects of nanoclustering structure on friction behavior of a-C:H coating

As the formation of transfer layer and its tribochemical lubricant mechanism have been intimately investigated [14-18], the effects of nanoclustering structure of a-C:H coatings are generally ignored in previous experimental and simulation research. However, to a certain extent, the nanoclustering structure of "parent" a-C:H coating determines the structure and lubricant property of friction-induced transfer layer. An obvious evidence for this argument is the high friction coefficient of graphite sliding in N_2, in comparison with the super-low friction coefficient of polymer-like a-C:H coating in N_2 [3, 4]. In fact, according to friction reports of pure a-C:H coatings in recent decades, super-low lubricity are more likely to occur in polymer-like a-C:H coatings with hydrogen content above 34 at.% and nanoindented hardness below 13 GPa [4, 8]. The enrichment of sp^3 $CH_{(1, 2)}$ bonds in chains of polymer-like coating is conducive to the formation of super-lubricant transfer layer stably adhered on ball surface [4].

Consistently, in this thesis we also found comparatively higher friction coefficient in diamond-like coatings (namely as bias voltage was 1.0~2.0 kV) and lower friction coefficient of polymer-like coatings and graphite-like coatings (still with hydrogen content about 18 at.%) as described in Figure 6.12 and Table 6.5. By observing the wear marks on ball and plates sides shown in Figure 6.7, we found that in case of B1.5~B2.5 coatings, very thick transfer layers were formed on ball surfaces, but a

large portion of them are detached, and lots of wear debris accumulated beside contact surfaces. It seems that diamond-like coating structure formed in 1.5~2.5 kV is unfavorable to the establishment of low-friction and durable transfer layer. A qualitative analysis on the wear marks formed in N_2 atmosphere and ambient air, including wear scars and debris on SUJ2 balls, plus the wear tracks and debris on coated Si plates were characterization by Raman spectroscopy as shown in Fig. 6.13, and Fig. 6.14 shows the three typical parameters of Raman spectra by deconvolution analysis. Clearly, it can be seen that in comparison with the as-deposited coating, the wear marks generally exhibited a shift of G peak position toward higher wavenumber by 5~30 cm^{-1}, an increase of *I(D)/I(G)* ratio by 0.2~1.5 and a reduce of G peak width by 25~50 cm^{-1}. All of these changes indicate a structure transformation of sp^3 C to sp^2 C on contact surfaces. Particularly, compared with as-deposited coating, the ball scar derived from B2.0 coating showed the largest growth of *I(D)/I(G)*, the largest reduce of G peak width and moderate up-shift of G peak, which implies a great transformation of sp^3 C to sp^2 C bonded in aromatic rings in amorphous manner. By contrast, the ball scar derived from B0.5 coating showed a reduce of *I(D)/I(G)*, a slight decrease of G peak width and moderated increase of G peak position, which implies a transformation of sp^2 C bonded from aromatic rings to chains with relatively higher coordination of hydrogens. The transfer layer in such kind of structure in rich of chain-like sp^2 $CH_{1,2}$ showed good lubricant properties in dry sliding conditions.

Also, in consideration on the nanoclustering structure of B1.5~B2.5 coatings, we inferred that the boundary hydrogen-free sp^2 C' sites trapping around graphite-like sp^2 C" clusters may inhibit the formation of well-lubricant transfer layers in rich of chain-like sp^2 $CH_{1,2}$ bonds. According to the structure characterization of studied coatings aforementioned in Chapter 4 and Chapter 5, our ion-vapor deposited a-C:H coatings mainly concentrate on sp^2-dominant area in ternary phase diagram, and tend to approach sp^2 peak with an increase of bias voltage, as illustrated in Figure 6.15a and magnified in Figure 6.15b. Specifically, for diamond-like coatings deposited under 1.5~2.5 kV, a majority of sp^3 C are tetrahedrally cross-linked by four σ bonds to form the skeleton of amorphous network, in which localized sp^2 C" clusters in medium size are embedded with highest fraction of boundary hydrogen-free sp^2 sites. Compared with polymer-like coating, such type of diamond-like structure is less likely to form well-lubricant transfer layer in rich of chain-like sp^2 $CH_{1,2}$ in tribochemical reactions.

Besides, as the nanoclustering structure evolved sensitively with an increase of bias voltage, the mechanical property of a-C:H coating also changed greatly which consequently resulted in a change of Hertz contact condition for tested counterparts. The relatively higher Hertz contact pressure may lead to a quick consume of sliders in running-in period, and the quickly-accumulated debris can easily cause a break-up of transfer layer. Thus, for B1.5~B2.0 coatings, some spikes in CoF curves were found at the beginning of sliding in Figure 6.6. Although a brand new transfer layer may re-build up soon during further sliding, it still brought out a higher steady-state CoF.

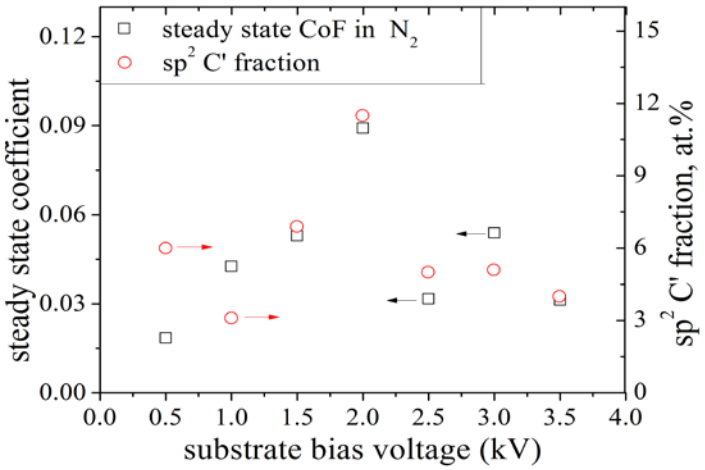

Figure 6.12 The correlations between steady state CoF in N_2 and fraction of sp^2 C' clusters as a function of substrate bias voltage.

Table 6.5 The mechanical property, Hertz contact pressure under 5 N normal load and steady-state friction coefficient of B0.5~B3.5 coating in N_2 and ambient air atmosphere.

	Hardness (GPa)	Young's Modules (GPa)	sp^2 C' fraction (at.%)	Hertz contact pressure (MPa)	CoF in N_2	CoF in ambient air
B0.5	8.94	77.78	6.0	462.77	0.018	0.119
B1.0	12.00	111.60	3.1	546.98	0.043	0.250
B1.5	14.93	160.60	6.9	674.70	0.053	0.216
B2.0	16.06	189.76	11.5	634.70	0.089	0.189
B2.5	13.09	146.61	5.0	612.72	0.032	0.096
B3.0	11.06	116.65	5.1	557.58	0.054	0.138
B3.5	10.06	98.59	4.0	517.55	0.031	0.146

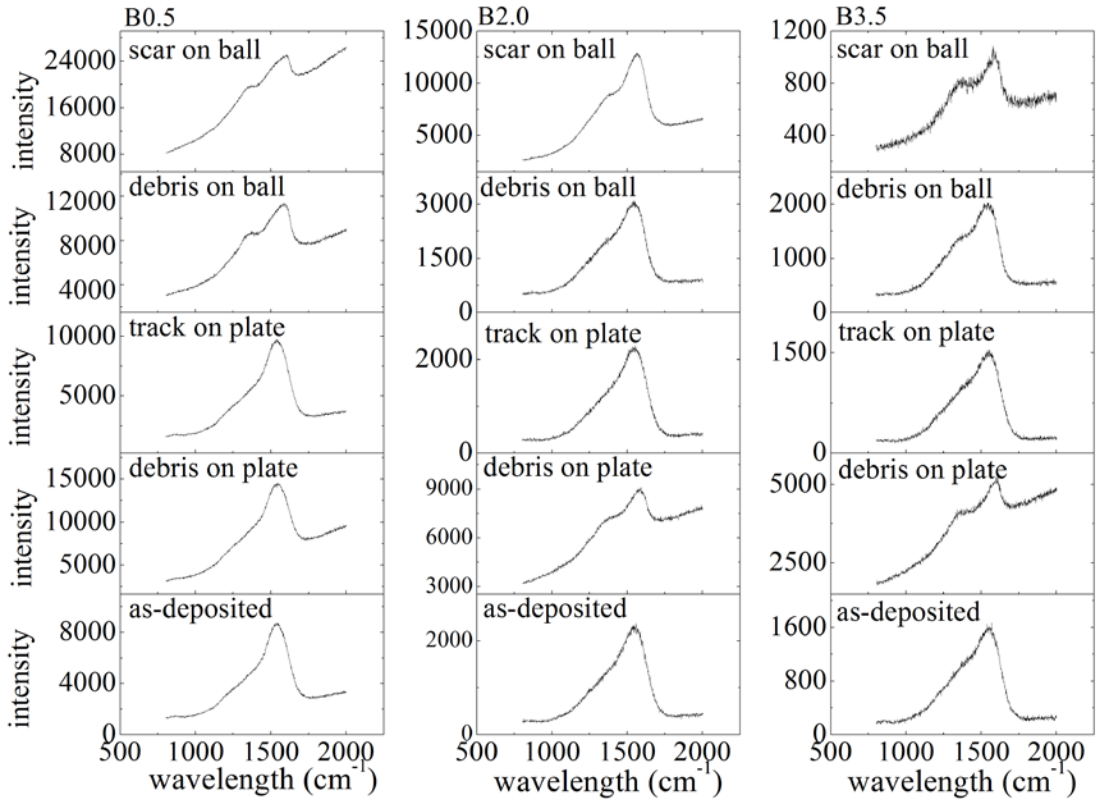

Figure 6.13 The Raman spectra of wear marks formed on ball and plate sliding against in N_2 atmosphere.

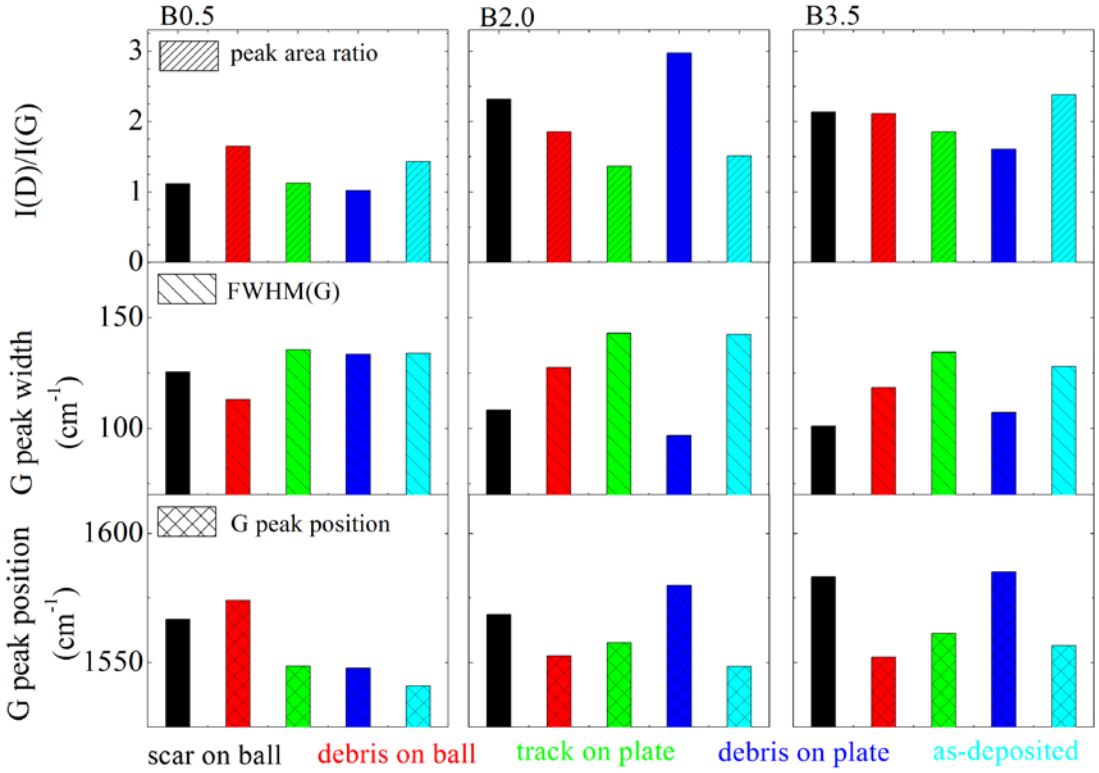

Figure 6.14 The typical Raman parameters of wear marks formed on ball and plate sliding against in N_2 atmosphere.

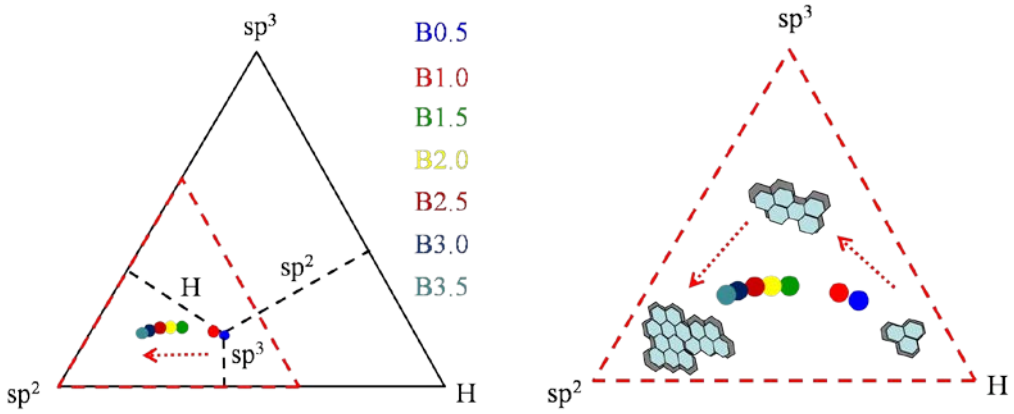

(a) (b)

Figure 6.15 The ternary phase diagram of ion-vapor deposited a-C:H coatings. (b) is an magnified description of studied a-C:H coatings localized within the dotted triangle area of typical ternary phase diagram (a), in which the summation of sp^2 C, sp^3 C and hydrogen is constant at 100 at.%.

6.4.2 Evolution of transfer layer produced in ambient air

As Raman spectra only reflects the chemical information of transfer layer after sliding, its dynamic evolution during sliding movement was missed. Especially as the tribotests are conducted in ambient air, the friction coefficient can hardly be stable after running-in period. To solve this problem, an overlapping tribotests were designed which used several set of ball/plate counterparts, sliding from the first cycle but prolonged to various sliding distances. And then, after the tests, two sliders were separated and analyzed. Additionally, except for the afore-concerned samples B1.5 and B2.0 coatings, another two coatings deposited under 0.4 Pa with bias voltage of 1.5 kV and 2.5 kV denoted as C1.5 and C2.5, respectively, were also tested for comparison. The CoF curves of overlapping sliding tests are summarized in Fig. 6.16. Except for few abnormal fluctuations in B2.0 coating, the standard deviation of CoF data is below 20%. Different from the results observed in H_2 and inert atmosphere [4-13], the running-in period of studied a-C:H/steel tribopairs sliding in ambient air was prolonged approximately to 170 m~290 m. The CoFs firstly grew up to its maximum about 0.2 over the prolonged running-in period, and then fell down to a relatively steady value about 0.14. Because of the undistinguishable running-in period in long duration tests, the average value of friction coefficient (i.e. avg. CoF) for each overlapped test was evaluated as the arithmetic average value of the whole *f(N)* curve.

Taking B2.0 as an example, the optical microscopic observation of wear marks are displayed in Fig. 6.17. According to Fig. 6.17a, a thick transfer layer was built up on

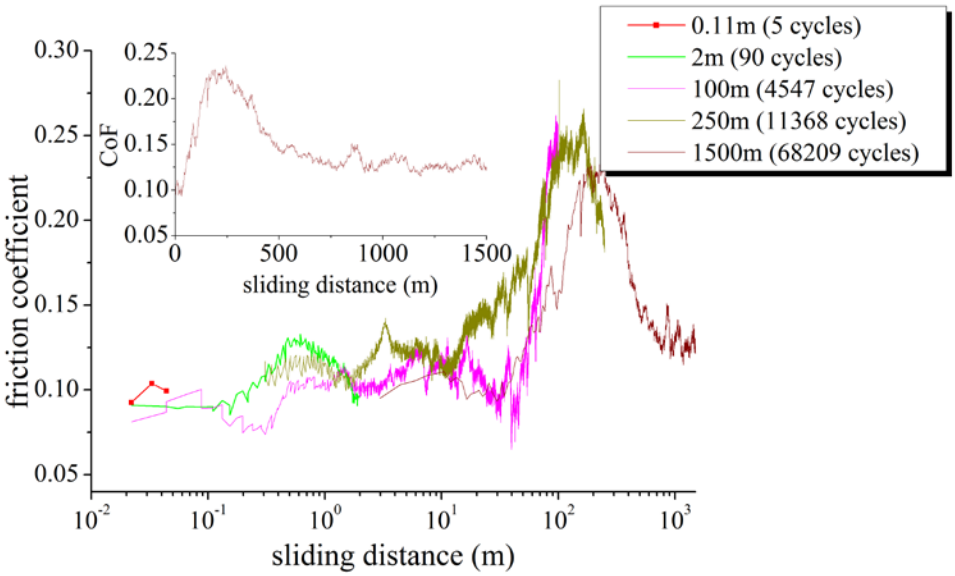

(a) B2.0 coating

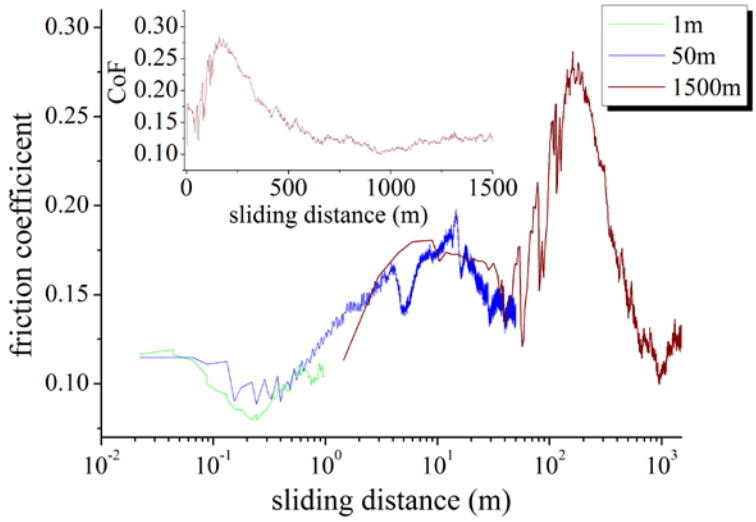

(b) B1.5 coating

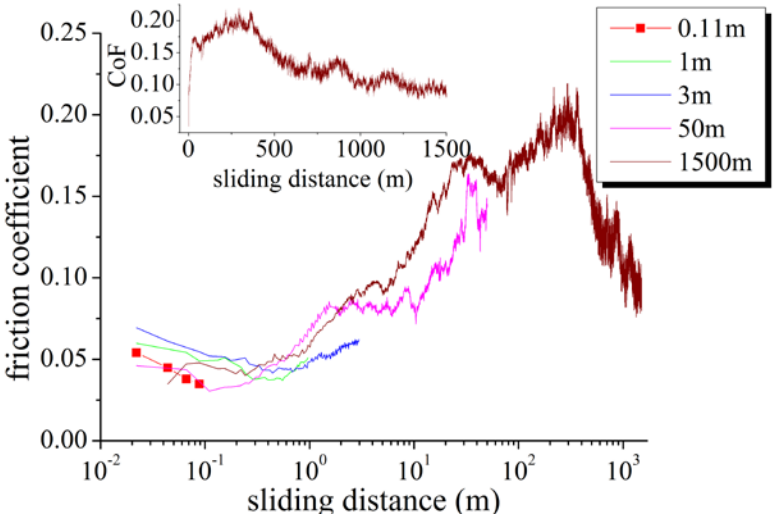

(c) C1.5 coating

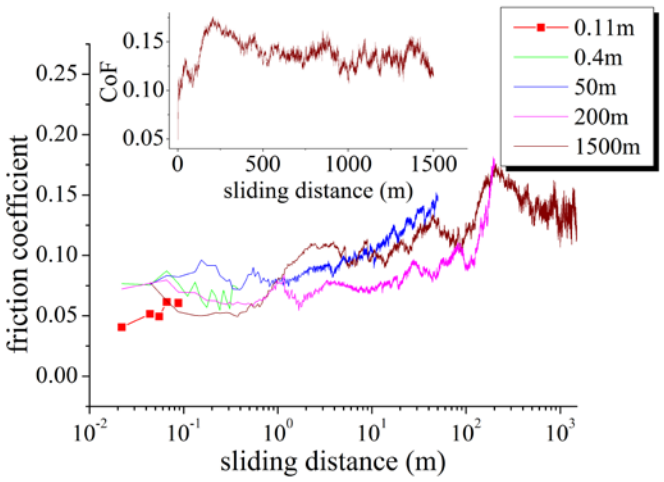

(d) C2.5 coating

Figure 6.16 Friction coefficients as a function of sliding distance *f(N)* in overlapping tribotests.

the sphere surface in the first sliding cycle (i.e. N=1, d=0.022 m), and covered the most part of contact surface. Also, a severely scratched wear scar in radius of 74 μm was formed on steel ball. Such a rapid build-up of transfer layer was also seen in the tests of other three coatings. When N reached up to 5 (i.e. N=5, d=0.11 m, see Fig. 6.16b), the wear scar radius jumped to 82 μm and the area of transfer layer increased simultaneously. More detailed information on the development of wear scar radius with sliding distance is plotted in Fig. 6.18. The wear scar radius increased greatly over the first 200 m and then entered into a steady state. No visible wear track was seen on the a-C:H coating until N=45 (i.e. d=1 m, see Fig. 6.17c and Fig. 6.17d), from which discontinuous wear tracks (inside the dashed squares of Fig. 17d) appeared on the coating, and most of transfer layer moved from the center of contact surface to the tail of wear scar (see Fig. 6.17c) and got thinner. From N=45 to N=11368 (i.e. the end of running-in period in case of B2.0 coating, d=250 m), wear tracks expanded largely in width and depth, and majority of wear debris removed to the two sides of contacting surface (see Fig. 6.17e and Fig. 6.17f). Then during the following steady sliding $4547 \leq N \leq 68209$ (i.e $100\ m \leq d \leq 1500\ m$), the wear rate of steel ball decelerated obviously while the wear rate of carbon coating accelerated moderately (see in Fig. 6.17g, Fig. 6.17h and Fig. 6.18). Visually, the transfer layers and wear debris had a rusty color due to the strong carbon oxidation in open air [25].

Based on the optical microscopy profiles, it was assumed that all the wear scars formed on steel balls were flat and circular, so that the wear rates of balls were

geometrically calculated as given in Fig. 6.19. Consistent with other reports [7, 14, 25, 29], the logarithmic wear rate of ball decreased linearly with logarithmic sliding distance.

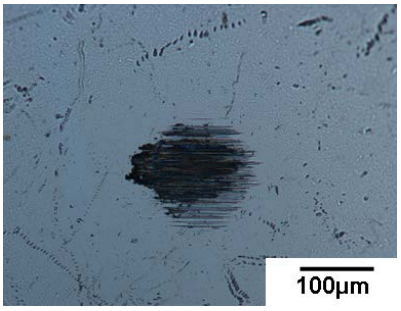

(a) N=1 (d=0.022m) ball

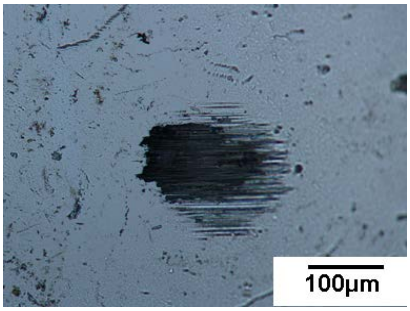

(b) N=5 (d=0.11m) ball

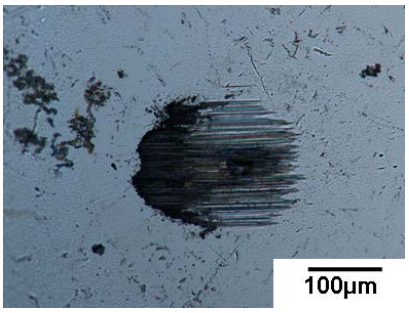

(c) N=45 (d=1m) ball

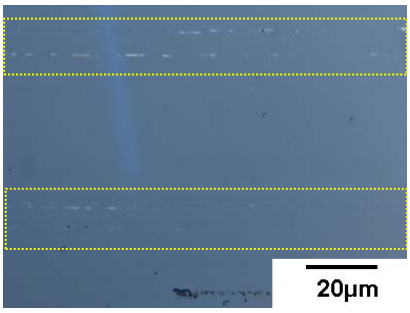

(d) N=45 (d=1m) plate

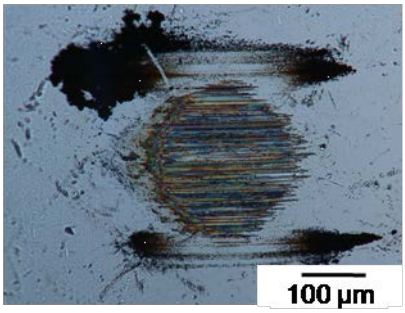

(e) N=11368 (d=250m) ball

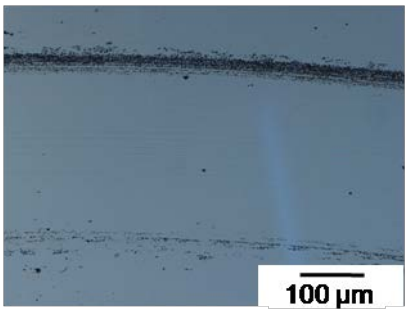

(f) N=11368 (d=250m) plate

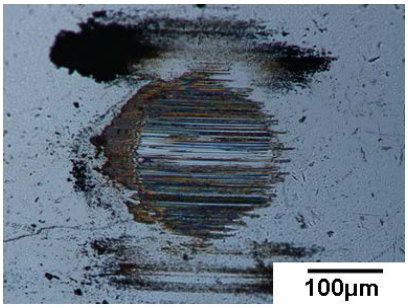

(g) N=68209 (d=1500m) ball

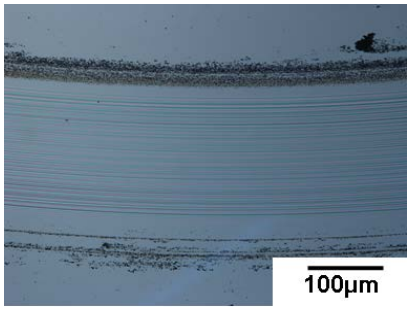

(h) N=68209 (d=1500m) plate

Figure 6.17 The wear marks derived from B2.0 coating on plates and steel balls. d represents the sliding distance.

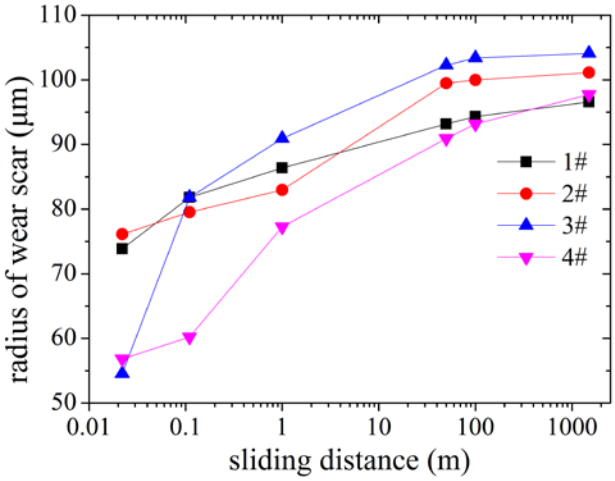

Figure 6.18 The radius of wear scar formed on steel balls in relation with increasing sliding distances.

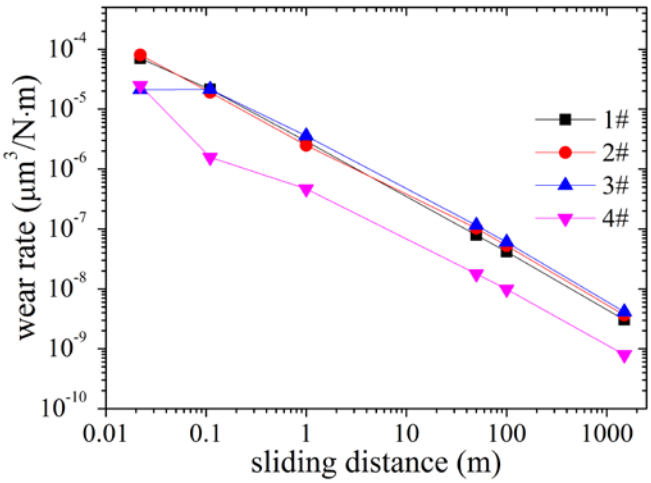

Figure 6.19 The wear rate of steel balls in relation with increasing sliding distances.

To get an insight into the wear mechanism of studied a-C:H coating, the wear marks formed in running-in period and long-duration tribotests were checked by AFM, optical microscopy and while light interferometer (WLI), as described in Fig. 6.20~Fig. 6.22. Specifically, Fig. 6.20a displays an AFM observation of the smooth surface of B2.0 a-C:H coating before sliding, and Fig. 6.20b~Fig. 6.20d compare the specific wear track formed when N = 68209, which is atomically smooth along the sliding direction (see Fig. 6.20c) but irregularly rough in transverse direction (see Fig. 6.20d). Particularly, in Fig. 6.20b and Fig. 6.20c, some mechanically scissored sharp-profiled debris was found accommodated nearby the scratched valleys in wear tracks. Such sharp-profiled wear debris could lead to a mechanical interlocking in high-pressure contact and deteriorate the rubbing condition and produce more abrasive debris in the following sliding. Actually, according to the optical microscopic

observation as shown in Fig. 6.17, majority of wear debris was compacted and adhered to the spherical counterpart, forming a transfer layer with scratched and abrasive surface. Such abrasive transfer layers were also found in WC/a-C:H coating which was tribotested in air [25]. Also, it can be seen in Fig. 6.21 that as sliding went by, the size of wear debris decreased obviously, so that the scratched marks got flattening and the compactness of transfer layers improved markedly. Both the flattening of transfer layer and its stationary adherence to steel balls could positively lead to a decrease of CoF in long-duration sliding.

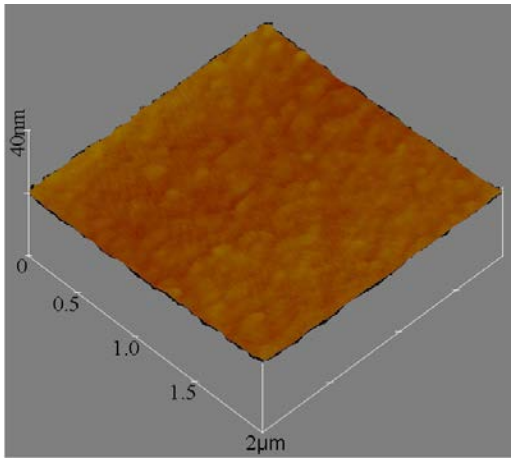

(a) as-deposited B2.0 coating

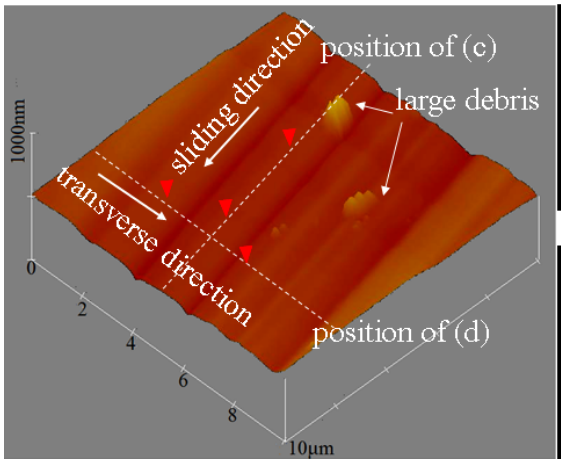

(b) wear track on B2.0 coating

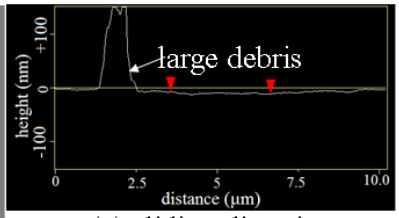

(c) sliding direction

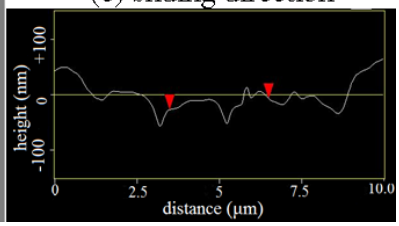

(d) transverse direction

Figure 6.20 Surface profiles of as-deposited and worn B2.0 a-C:H coating. (a) as-grown surface of B2.0 coating; (b) wear track formed on B2.0 coating when N=68209 (d=1500 m); (c) cross sectional profile of wear track along the sliding direction; (d) cross sectional profile of wear track along the transverse direction. The dotted lines and white arrows in (b) show the position of cross sectional images corresponding to (c) and (d) respectively.

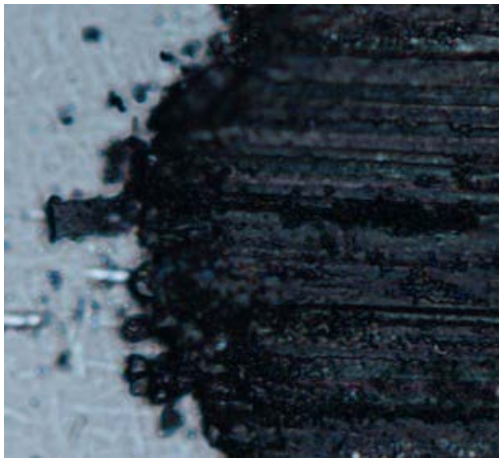

(a) *N*=45 (*d*=1 m) ball

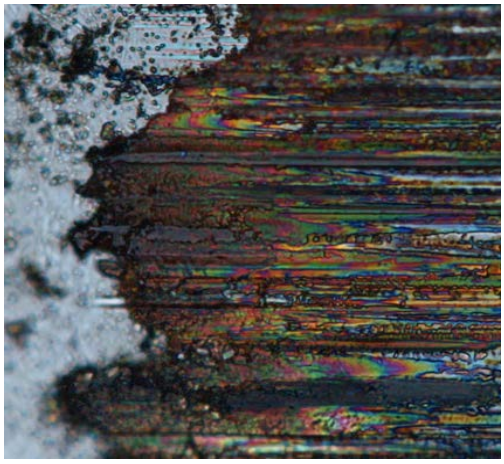

(b) *N*=2274 (*d*=50 m) ball

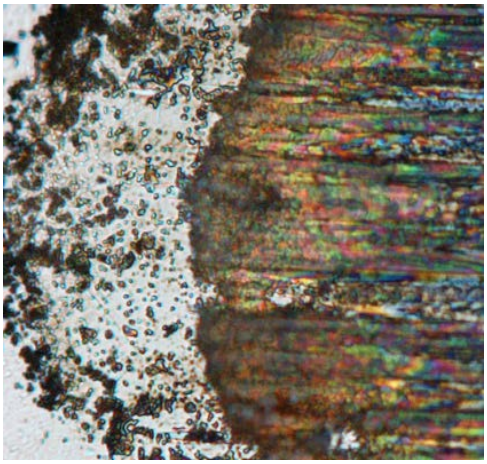

(c) *N*=4547 (*d*=100 m) ball

Figure 6.21 The optical microscopy observation of compacted wear debris adhering to steel balls sliding on B2.0 coating for various distance.

Generally, in ball-on-plate sliding tests of two dissimilar materials rubbing against each other, the softer counterpart wears more rapidly than the harder one. Such a

phenomenon was also observed in the studied a-C:H coating/steel ball tribopairs through the WLI observation. Taking C2.5 coating for example, the WLI images of specific wear marks are displayed in Fig. 6.22. In Fig. 6.22a, i.e. N=1, the spherical surface was severely scratched by initial asperities and some V-shaped tracks as deep as 200 nm~1 μm were created in an oval region (see the right picture of Fig. 6.22a). Different from the assumption established in Fig. 6.20, the wear scar was not flat and circular at the beginning of sliding but kept as spherical profile until N=2274 (see the left picture in Fig. 6.22b), from which the depth of V-shaped tracks on balls decreased below 500 nm, and the depth of wear tracks on coatings grew up to 12 nm (see the left picture in Fig. 6.22c). Afterwards during 2274≤N≤45473 (i.e. 50 m≤d≤1000 m), wear tracks on coatings enlarged remarkably to 120 nm deep and 160 μm wide (see Fig. 6.22e), while the wear scars got relatively smoother (see Fig. 6.22d). Consistent with AFM scanning, the scratched marks in WLI images revealed abrasive wear of a-C:H coating/steel ball tribopairs sliding in ambient air, especially during running-in period.

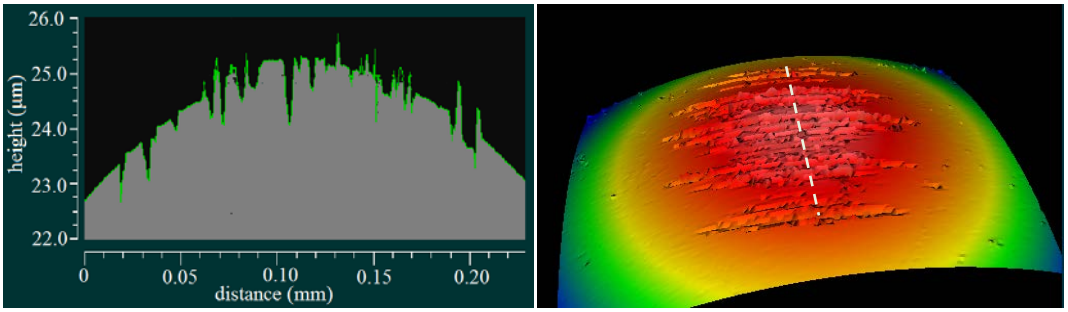

(a) N=1

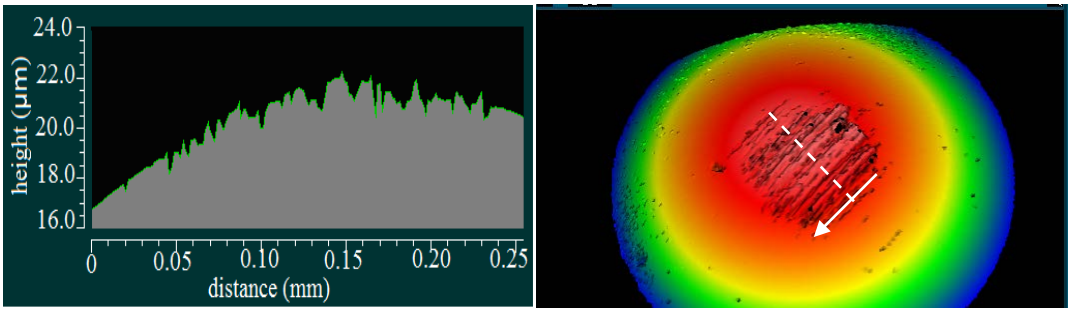

(b) N=2274

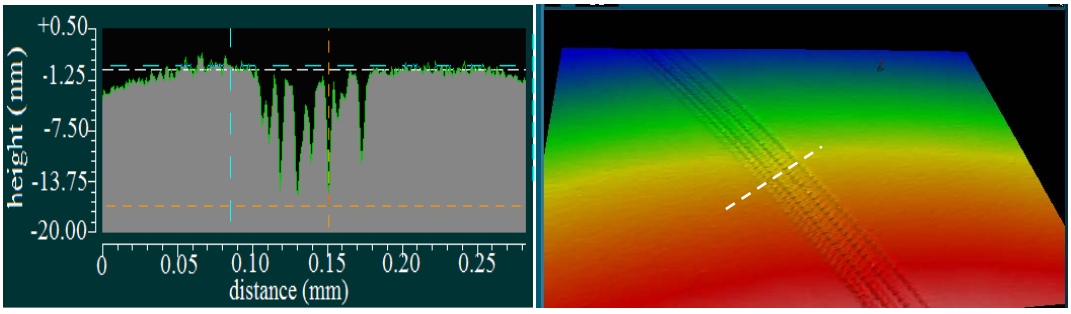

(c) N=2274

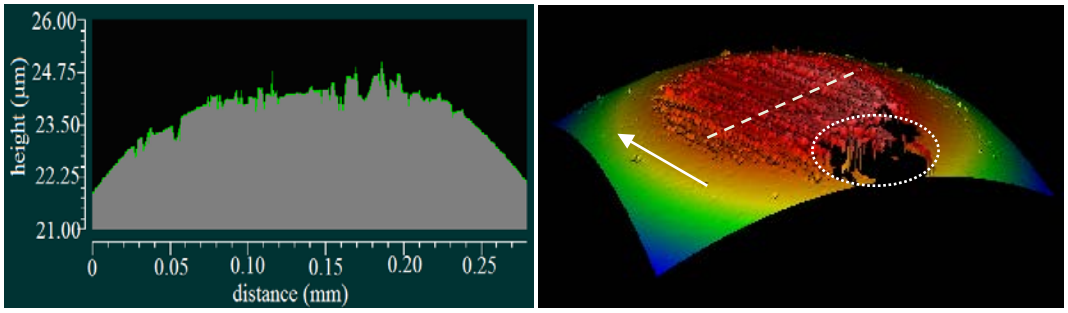

(d) N=45473

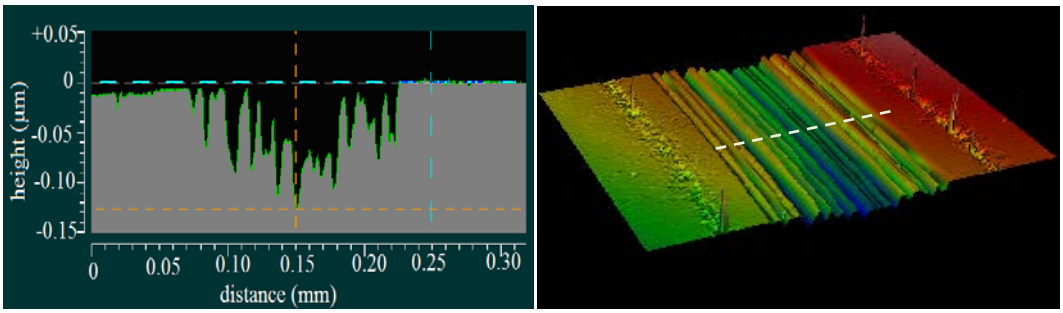

(e) N=45473

Figure 6.22 WLI profiles of wear marks derived from C2.5 coating. (a) Wear scar on ball when N=1, d=0.022 m; (b) wear scar on ball when N=2274, d=50 m; (c) wear track on plate when N=2274; (d) wear scar on ball when N=45473, d=1000 m; (e) wear track on plate when N=45473. The white dotted lines in right side indicate the analysis position of cross-sectional images shown in left side; the white solid arrows denote the relative sliding direction of balls. The black area addressed by a dotted white circle in (b) corresponds to the thickest part of transfer layer, which is beyond the detectable height of WLI.

6.4.3 Chemical characterization of transfer layers by XPS

Taking account of the repeatability of CoF curves, transfer layers derived from B2.0 and C1.5 coating in overlapping tribotests were selected and further analyzed by XPS. Particularly, in order to investigate the effects of natural oxidation of steel ball in ambient air, a blank steel ball (labeled as N=0 in Fig. 6.23) washed supersonically in acetone and exposed in the same atmosphere was also measured by XPS for comparison.

As an example, Fig. 6.23 compares the XPS C 1s, O 1s and Fe 2p3/2 spectra of transfer layers derived from B2.0 coating when N={0, 1, 2274, 11368, 68209}, respectively. All the detected spots were selected according to the scanning X-ray image (SXI) images of wear scars as shown in Fig. 6.23a, by which the spots with

highest density of secondary electrons were selected. The XPS spectra obtained from different spots on transfer layer (e.g. cross cursor 7, 9, 10 in Fig. 6.23a) was almost the same. It is noted that after one minute pre-sputtering, the nitrogen content in transfer layers and blank ball was generally below 4 at.%, and the carbon and oxygen content in blank ball was 9.2 at.% and 5.6 at.%, respectively. By comparison, without pre-sputtering the carbon and oxygen content in blank ball was 45.8 at.% and 48 at.%, respectively. Obviously, the small peaks of C 1s and O 1s spectra of blank ball (N=0) with pre-sputtering treatment indicate a negligible effect of physisorbed moistures in this *ex situ* XPS measurement, while the intensive C 1s, O 1s peaks of the worn balls ensure the validity of detected spots which were covered by a oxygen-rich layer on the top surface. The shift of Fe 2p3/2 peaks from 707.125 eV of the blank ball to 711.125 eV of the worn balls implies that the negligible natural oxidation of iron ball in ambient air was activated markedly in sliding contact [30]. Fig. 6.24 displays the evolution of chemical composition of transfer layers with an increase of sliding distances. Briefly speaking, all the transfer layers were composed of carbon and substantial content of oxygen, while the iron content was little and mainly found as oxides rather than metallic form. The oxygen content increased immediately from 5.6 at.% when N=0 to 30~50 at.% in sliding due to the tribochemical oxidation of transferred carbons in ambient air. By comparison, the iron content in transfer layer grew rapidly over the first 50 m (N≤2274) and fell back to the initial level within the following 50 m (2274≤N≤4547), and kept relatively constant afterwards. The rapid increase of iron content within 0 m≤d≤50 m is consistent well with the rapid enlargement of wear scar shown in Fig. 6.18, a rapid wear of softer counterpart in running-in period.

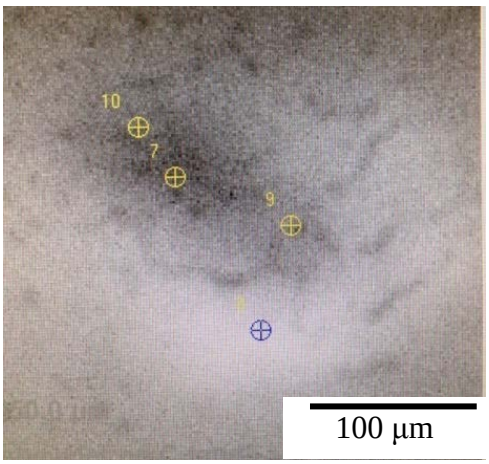

(a) SXI image of a wear scar

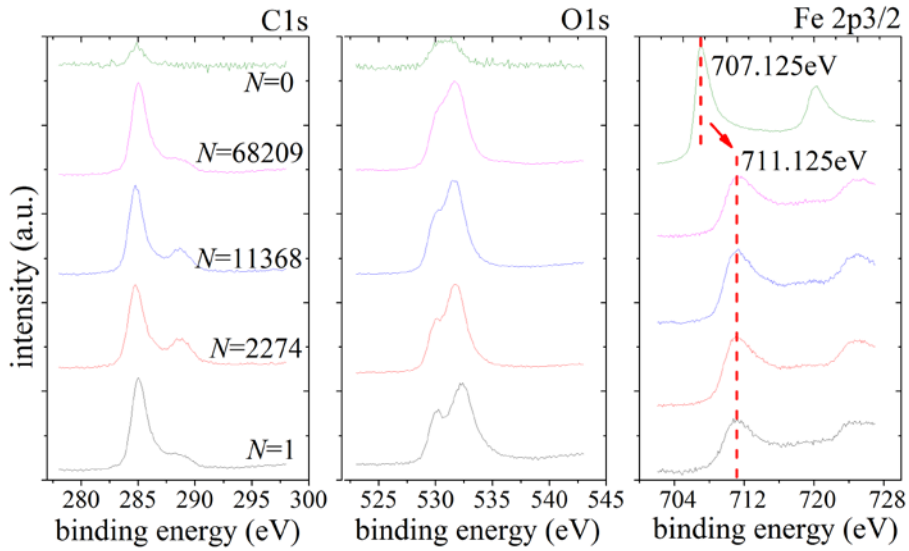

(b) XPS spectra of C1s, O1s and Fe 2p3/2

Figure 6.23 (a) SXI image of a wear scar (when N=45, d=1 m, B2.0 coating), in which the black region inside solid blue circle is transfer layer, and the grey region inside dotted red circle is the remained part of wear scar not covered by transfer layer; four cross cursors denote the selected spots for XPS measurement; (b) The XPS spectra of C 1s, O 1s and Fe 2p3/2 peaks of transfer layers derived from B2.0 coating with increasing sliding distance.

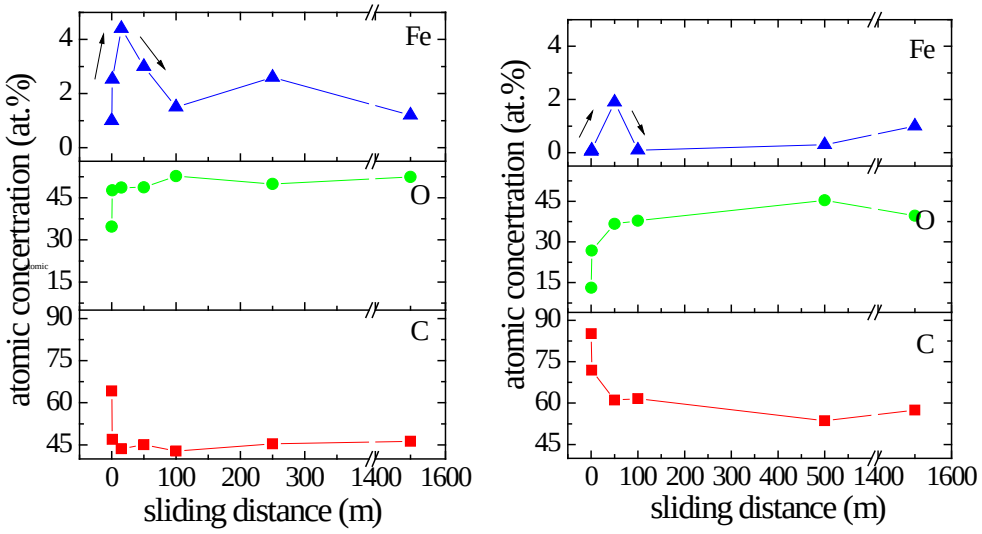

(a) B2.0 coating (b) C1.5 coating

Figure 6.24 The surface composition of transfer layers in relation to increasing sliding distance.

Further analysis of transfer layers was carried out by using EDX, and Fig. 6.25 illustrates the specific results obtained when N=2274 (i.e. d=50 m). Being consistent

with the XPS results provided in Fig. 6.24, the iron (blue color in Fig. 6.25c) content in transfer layer (black color in Fig. 6.25a) was quite limited, and intensive amount of iron was only seen in the discontinuous regions of transfer layer where direct rubbing occurred between steel ball and carbon coating. In contrast, high content of oxygen (given in Fig. 6.25d) was detected in carbon-rich regions (red in Fig. 6.25b), suggesting an active tribochemical oxidation occurred with an incorporation of O_2 and H_2O on the top surface.

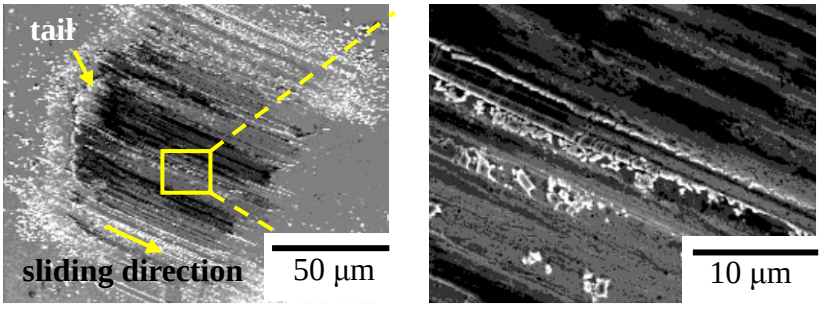

(a) SEM images

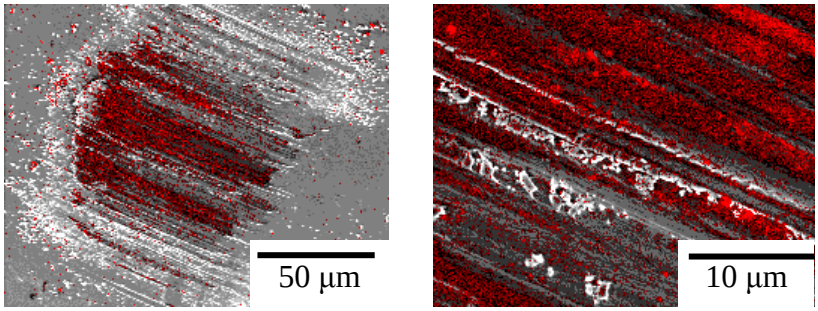

(b) carbon

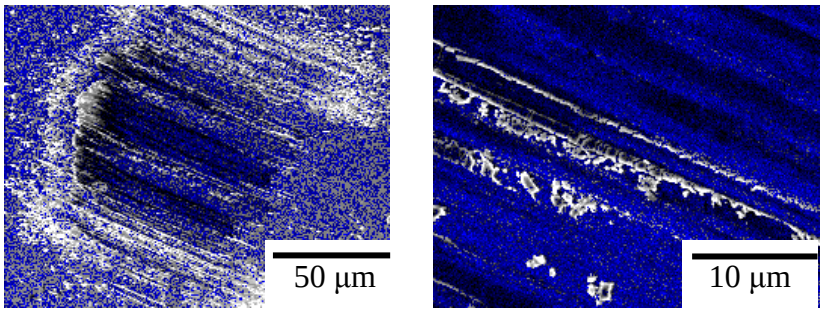

(c) iron

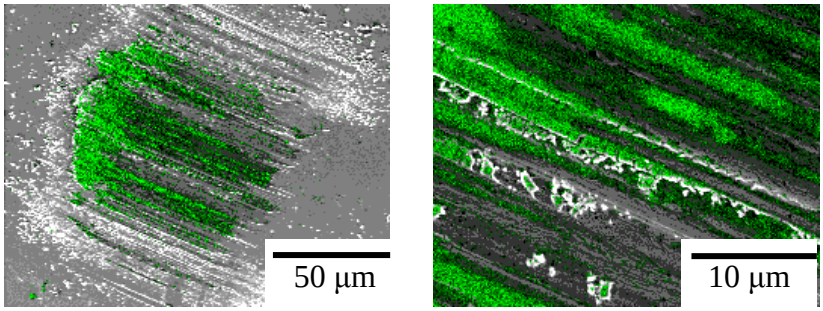

(d) oxygen

Figure 6.25 The EDX characterization wear scars derived from B2.0 coating.

Usually, with regard to the tribopairs of uncoated steel ball sliding on a-C:H coating in humid air, it is difficult to define the correlation between the nature of transfer layer and low friction performance of a-C:H coating. On one hand, transfer layers are circularly built up and broken by shear strength during sliding [14]; on the other hand, the molecular structure of transfer layers evolves continuously in sliding contact [14, 15]. Thus, both the physical and chemical nature of transfer layers have substantial effects on the friction and wear of a-C:H coatings. Moreover, a close correlation between the average contact pressure and wear rate of balls was also found in this paper, especially in the beginning of running-in period (point A→B) as shown in Fig. 6.26. In case of B2.0 coating, as the average contact pressure decreased rapidly from the maximum value (Hertz-contact pressure) at the beginning of sliding (point A) to 170 MPa at the end of long-duration sliding (point C), the wear rate of steel ball reduced greatly from 7×10^{-5} $\mu m^3/N\cdot m$ to 3×10^{-9} $\mu m^3/N\cdot m$. At the same time, the carbon content in transfer layer decreased simultaneously from 64.2 at.% to 46.3 at.% probably due to the reducing thickness of transfer layer (see Fig. 6.21). It is inferred that the total thickness of transfer layer is mainly determined by the carbon-based layer, while the thickness of chemisorption layer is generally below 6 nm in all the tested samples.

Based on the results mentioned above, a three-stage wearing process of studied a-C:H coating/steel ball tribopairs sliding in ambient air is deduced as illustrated in Fig. 6.27. At the beginning of running-in period (as long as 50 m for the four coatings), thanks to the initial roughness of counterface and the smallest Hertz-contact area, the maximum contact pressure is reached and severe wear firstly occurs on the softer counterparts. As a result, transfer layer composed of loosely compacted wear debris with relatively higher content of iron oxides is built up on the spherical body, and leads to a third-body dominated abrasive wear on the counterface. With the rapid consuming of steel spheres in the first 50 m, the average contact area ($A \propto r^2$, r is the radius of wear scar) increases greatly in this period while the average contact pressure decreases at the same speed. The following sliding within 50 m$\leq d \leq$250 m (in case of B2.0 coating) is an important period for the stabilization of mechanical interactions between counterparts. Due to the marked decrease of average contact pressure and flattening of counterface, the transfer layer gets stable and reliably adheres to the spherical surface. In the steady stage (i.e. $d \geq 245$ m in case of B2.0 coating), the

stationary shearing between transfer layer and underneath coating leads to a gradual decrease of CoFs, and both of the tribopairs are consumed at a moderate speed until the failure of a-C:H coating. The whole wearing process can be briefly described as a comparison of the wear marks in the right side of Fig. 6.27.

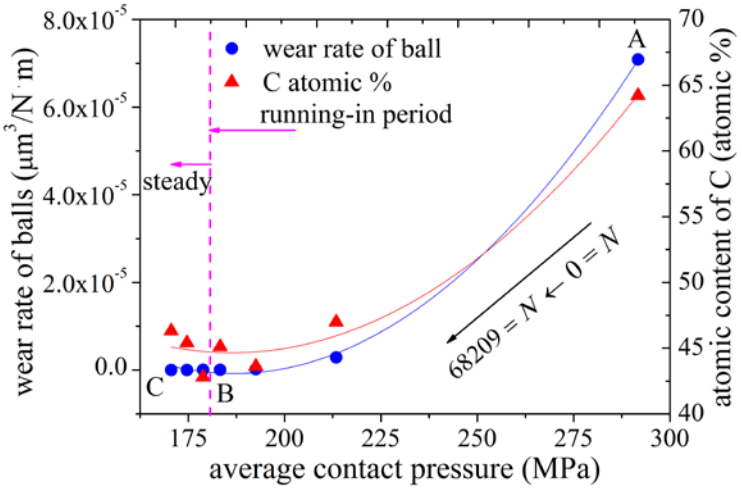

(a) B2.0 coating

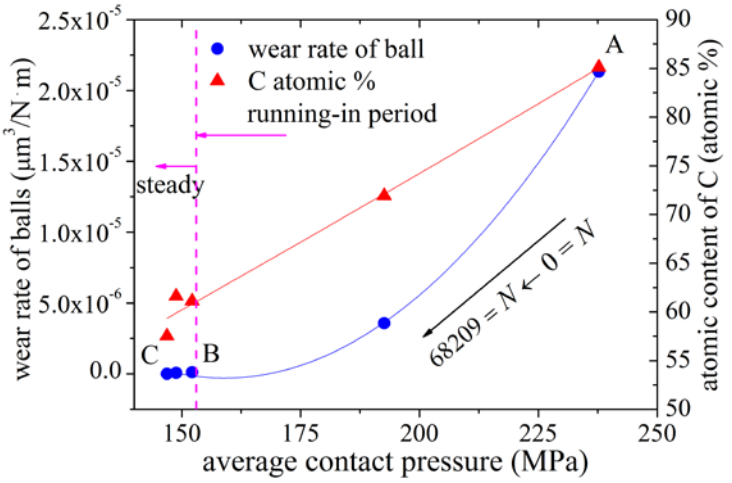

(b) C2.5 coating

Figure 6.26 The wear rate of balls and carbon content in transfer layers in relation with the average contact pressure.

More detailed information on the tribochemical interaction of studied a-C:H coating/steel ball tribopairs was revealed through the deconvolution analysis of transfer layer's C1s spectra as provided in Fig. 6.28 and Fig. 6.29. In Fig. 6.28, C 1s spectra were deconvoluted into four peaks as C1~C4 which corresponded to four types of C/C and C/O bonds, and detailed atomic content of each type was supplied in Fig. 6.28. Consistent with previous reports [5, 6, 15, 31-34], the content of C-C bonds in transfer layers reduced immediately within the first 100 m and kept below 12 at.%

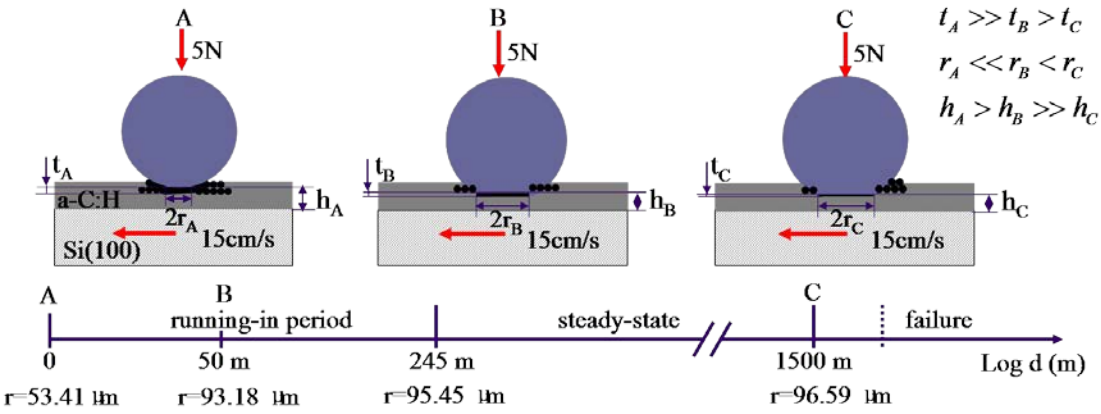

Figure 6.27 A schematic representation of the three-stage wearing process of a-C:H coating/steel ball tribopairs in ambient air. $t_{A,B,C}$ is the thickness of transfer layer in the nanometer scale, $r_{A,B,C}$ the radius of wear scar in the micrometer scale; $h_{A,B,C}$ the residual thickness of coating, i.e. the distance between steel counterfaces and the coating/substrate interface in the nanometer scale. The supplied values of $r_{A,B,C}$ correspond to the B2.0 coating.

afterwards, while the content of C/O groups got much higher than that in the as-grown coating. Specifically, the area contribution of C4 peak was generally higher than that of C3, which may be attributed to the difference in bond strength (C=O 799 kJ/mol, C-O 358 kJ/mol). Meanwhile, different transformation of C-C bond (bond strength 346 kJ/mol) was found in transfer layers derived from B2.0 and C2.5 coating respectively: in case of B2.0 coating, the amount of C-C bond decreased rapidly from the initial value of 32.64 at.% to 3~8 at.% over the first 100 m, while both the content of C=O and C-O bond increased to 3 times higher, and the C=C (bond strength 602 kJ/mol) content grew linearly from 52.5 at.% to 58.31 at.%; nevertheless, in case of C2.5 coating the broken C-C bonds mainly transferred to C=C and C=O, and the C-O content decreased rapidly over the first 50 m and kept at a low level (<9 at.%) afterwards. However, deeper understanding on this different behavior of chemical transformation is still in controversy.

In respect of the generation of C/O groups in chemisorption layer, a widely accepted mechanism is that the broken C–H bonds on the top surface generate dangling bonds C– and easily form adhesive junctions like C=O groups with ample presence of O_2 and H_2O [13, 14, 19, 20, 35, 36]. Indeed, by eliminating the effect of physisorption layer, a negative role of C/O bond on the low-friction performance is clearly revealed in Fig. 6.30. The average friction coefficient evolved correspondingly

with the total content of C–O and C=O bonds, and B2.0 coating with higher content of C/O exhibited higher CoFs than C2.5 coating. It is believed that compared with the initial a-C:H coatings which are saturated by C–H bonds (bond strength 411 kJ/mol, electro-negativity C:H=2.55:2.1) on top surface, the C/O-covered surface (electro-negativity C:O=2.55:3.44) of transfer layer generate stronger polarization toward top surfaces, and thus lead to stronger adhesion forces between sliding surfaces.

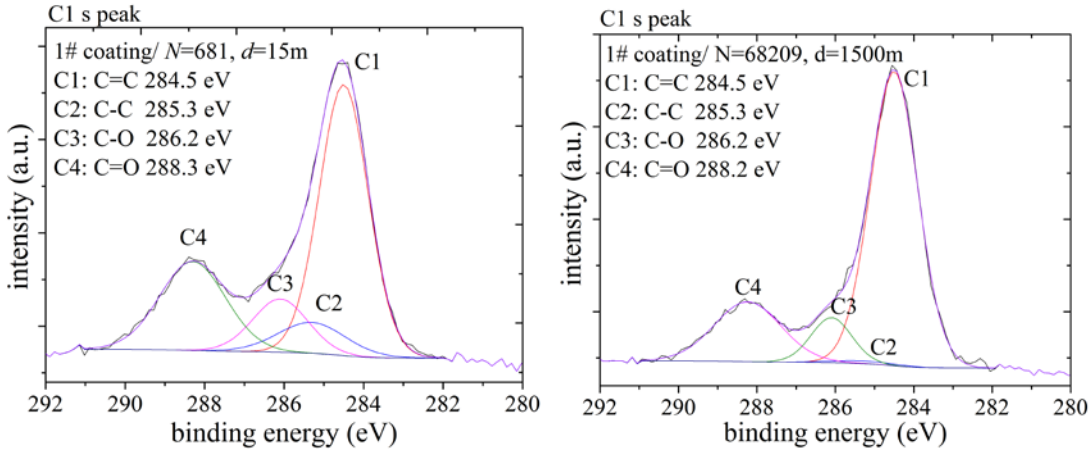

(a) *N*=681 (b) *N*=68209

Figure 6.28 Deconvolution analysis of C1s spectra of transfer layers derived from B2.0 coating when *N* was 681 and 68209, respectively.

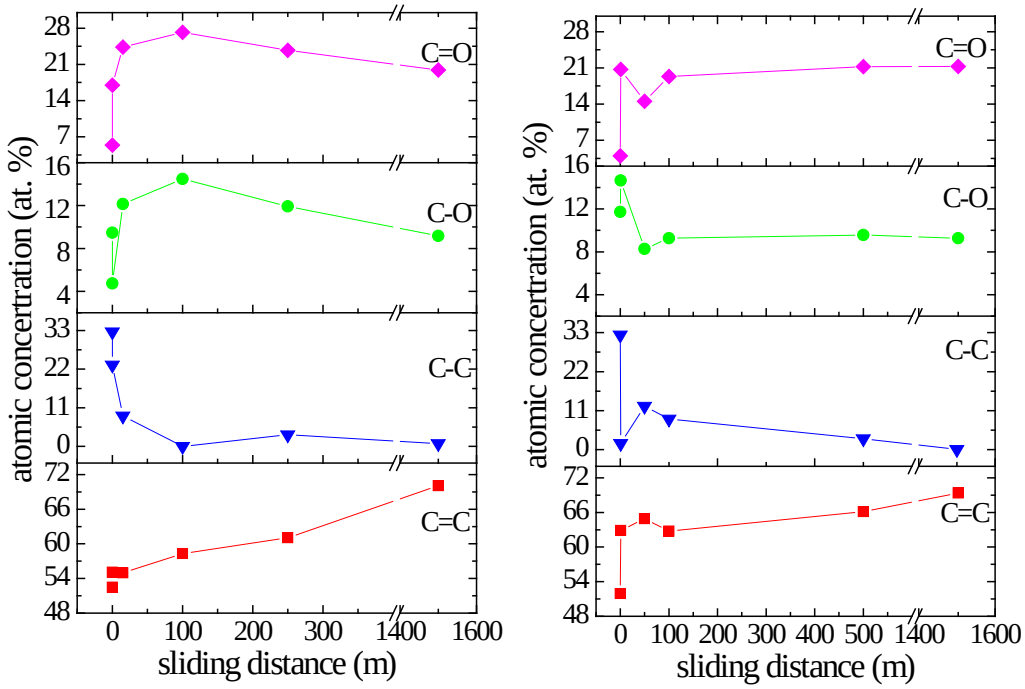

(a) B2.0 coating (b) C2.5 coating

Figure 6.29 The atomic content of various carbon bonds of transfer layers in dependence of increasing sliding distance.

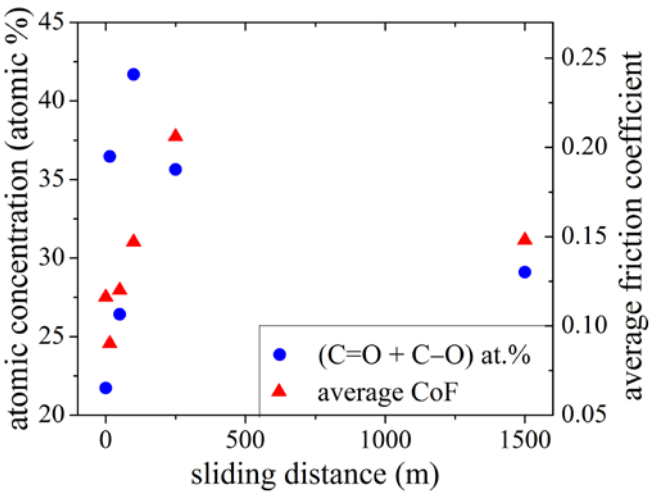

(a) B2.0 coating

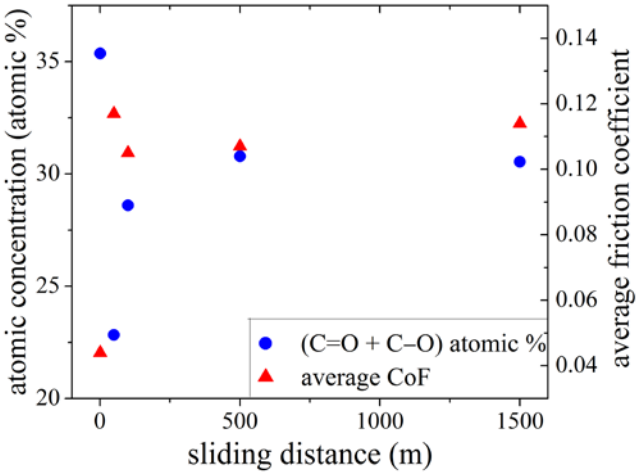

(b) C2.5 coating

Figure 6.30 The correlations between atomic content of C/O bonds and average friction coefficient with increasing sliding distance.

Meanwhile, the friction-induced phase transformation of carbon base from sp^3 C to sp^2 C could also cause addition adhesion force because of the π-π* attraction [4, 10]. Furthermore, the low fragmentation degree of hydrocarbon source ionized by hot filament method could enhance the formation of C/O groups on the top surface of a-C:H coating, and consequently lead to an increase of CoFs in ambient air [20].

6.5 Conclusions

In this paper, a-C:H coatings grown by ion vapor deposition were tribotested on a ball-on-plate device in N_2 atmosphere and ambient air. An Obvious correlation between the nanoclustering structure of a-C:H coating and its friction performance was observed, especially as tribotests conducted in N_2 atmosphere. We found

comparatively higher friction coefficient in diamond-like coatings as bias voltage was 1.5~2.5 kV and lower friction coefficient in polymer-like coatings and graphite-like coatings (still with hydrogen content about 18 at.%). A Raman characterization of wear marks revealed that compared with as-deposited coating, the ball scar derived from B0.5 coating showed a reduce of *I(D)/I(G)*, a slight decrease of G peak width and moderated increase of G peak position, which implies a transformation of sp^2 C bonded from aromatic rings to chains with relatively higher coordination of hydrogens. The transfer layer in such kind of structure in rich of chain-like sp^2 $CH_{1,2}$ can show good lubricant properties in dry sliding conditions. Also, it is inferred that the boundary hydrogen-free sp^2 C' sites trapping around graphite-like sp^2 C" clusters may inhibit the formation of well-lubricant transfer layers in rich of chain-like sp^2 $CH_{1,2}$ bonds.

Furthermore, by performing one set of overlapping tribotests of a-C:H coating/steel ball tribopairs in ambient air, both the morphology and chemical characteristics of transfer layers were tracked by *ex situ* optical microscopy, XPS and SEM/EDX. Carbon-based transfer layer was built up in the first sliding cycle in all the tribotests, and covered by an oxygen-rich chemisorption layer on the top surface. A three-stage model was presented to describe the wearing process of studied a-C:H coating/steel ball tribopairs sliding in ambient air. The XPS detection of Ar^+-cleaned transfer layer showed that except for the typical graphitization of transferred carbon materials, a noticeable tribochemical oxidation of carbon also occurred on the top surface of transfer layer and impacted the friction force strongly. The average CoFs increased correspondingly with the total content of C/O bonds in this tribochemical oxidation layer.

References

[1] S. Aisenberg, R. Chabot. Ion-beam deposition of thin films of diamondlike carbon. J. Appl. Phys. 42, 2953-2958 (1971)

[2] A. Erdemir, C. Donnet. Tribology of diamond-like carbon films: recent progress and future prospects. J. Phys. D: Appl. Phys. 39, 311-327 (2006)

[3] J. Robertson. Diamond-like amorphous carbon. Mater. Sci. Eng., R. 37, 129-281 (2002)

[4] A. Erdemir. Genesis of superlow friction and wear in diamondlike carbon films. Tribol. Int. 37, 1005-1012 (2004)

[5] A. Erdemir, O. L. Eryilmaz, I. B. Nilufer, G. R. Fenske. Synthesis of superlow friction carbon films from highly hydrogenated methane plasmas. Surf. Coat. Technol. 133-134, 448-454 (2000)

[6] A. Erdemir, C. Bindal, J. Pagan, P. Wilbur. Characterization of transfer layers on steel surfaces sliding against diamond-like hydrocarbon films in dry nitrogen. Surf. Coat. Technol. 76-77, 559-563 (1995)

[7] A. Erdemir. Design criteria for superlubricity in carbon films and related microstructures. Tribol. Int. 37, 577-583 (2004)

[8] J. Fontaine, J. L. Loubet, T. Le. Mogne, A. Grill. Superlow Friction of Diamond-Like Carbon Films: A Relation to Viscoplastic Properties. Tribol. Lett. 17, 709-714 (2004)

[9] J. Fontaine, M. Belin, T. Le. Mongne, A. Grill. How to restore superlow friction of DLC: the healing effect of hydrogen gas. Tribol. Int. 37, 869-877 (2004)

[10] C. Donnet, J. Fontaine, A. Grill, T. Le. Mogne. The role of hydrogen on the friction mechanism of diamond-like carbon films. Tribol. Lett. 9, 137-142 (2000)

[11] J. Fontaine, C. Donnet, A. Grill, T. Le. Mogne. Tribochemistry between hydrogen and diamind-like carbon films. Surf. Coat. Technol. 146-147, 286-291 (2001)

[13] J. Fontaine, T. Le Mogne, J. L. Loubet. Achieving superlow friction with hydrogenated amorphous carbon: some key requirements. Thin Solid Films. 482, 99-108 (2005)

[14] T. W. Scharf, I. L. Singer. Role of the transfer film on the friction and wear of metal carbide reinforced amorphous carbon coatings during run-in. Tribol Lett. 36, 43-53 (2009)

[15] I. L. Singer, S. D. Dvorak, K.J. Wahl, T. W. Scharf. Role of third bodies in friction and wear of protective coatings. J. Vac. Sci. Technol. A. 21, 232-240 (2003)

[16] T. W. Scharf, I. L. Singer. Role of third bodies in friction behavior of diamondlike nanocomposite coatings studied by in situ tribometry. Trib. Trans. 45, 363-371 (2002)

[17] T. W. Scharf, I. L. Singer. Monitoring transfer films and friction instabilities with in situ Raman tribometry. Trib. Lett. 14, 3-8 (2003)

[18] T. W. Scharf, I. L. Singer. Quantification of the thickness of carbon transfer films using Raman tribometry. Trib. Lett. 14, 137-145 (2003)

[19] D. S. Kim, T. E. Fischer, B. Gallois. The effects of oxygen and humidity on

friction and wear of diamond-like carbon films. Surf. Coat. Technol. 49, 537-542 (1991)

[20] K. Yuichi, K. Makoto. Influence of exposure to an atmosphere of high relative humidity on tribological properties of diamondlike carbon films. J. Vac. Sci. Technol. A. 7, 2311-2413 (1989)

[21] C. Donnet, T. Le Mogne, L. Ponsonnet, M. Belin, A. Grill, V. Patel, C. Jahnes. The respective role of oxygen and water vapor on the tribology of hydrogenated diamond-like carbon coatings. Trib. Lett., 4, 259-265 (1998)

[22] H. Ronkainen, J. Likonen, J. Koskinen, S. Varjus. Effect of tribofilm formation on the tribological performance of hydrogenated carbon coatings. Surf. Coat. Tech. 79, 87-94 (1996)

[23] Longchen Cui, Zhibin Lu, Liping Wang. Probing the low-friction mechanism of diamond-like carbon by varying of sliding velocity and vacuum pressure. Carbon. 66, 259-266 (2014)

[24] B. Marchon, N. Heiman, M. R. Khan. Evidence for tribochemical wear on amorphous carbon thin films. IEEE Trans. Magn. 26, 168-170 (1990)

[25] A. A. Voevodin, J.P. O'Neill, J. S. Zabinski. Tribological performance and tribochemistry of nanocrystalline WC/amorphous diamond-like carbon composites. Thin Solid Films. 342, 194-200 (1999)

[26] T. Y. Leung, W. F. Man, P. K. Lim, W. C. Chan, F. Gaspari, S. Zukotynski. Determination of the sp^3/sp^2 ratio of a-C by XPS and XAES. J. Non-Cryst. Solids. 254, 156–160 (1999)

[27] S. T. Jackson, R. G. Nuzzo. Determining hybridization differences for amorphous carbon from the XPS C 1s envelope. Appl. Surf. Sci. 90, 195–203 (1995)

[28] P. Merel, M. Tabbal, M. Chaker, S. Moisa, J. Margot. Direct evaluation of the sp^3 content in diamond-like-carbon films by XPS. Appl. Surf. Sci. 136, 105–110 (1998)

[29] L.Q. Li, A. Ovcharenko, I. Etsion, F. Talke. The Effect of asperity flattening during cyclic normal loading of a rough spherical contact. Tribol. Lett. 40, 347-355 (2010)

[30] T. Yamashita, P. Hayes. Analysis of XPS spectra of Fe^{2+} and Fe^{3+} ions in oxide materials. Appl. Surf. Sci. 254, 2441–2449 (2008)

[31] J. Andersson, R. A. Erck, A. Erdemir. Friction of diamond-like carbon films in different atmospheres. Wear. 254, 1070–1075 (2003)

[32] C. Donnet, M. Belin, J. C. Auge, J. M. Martin, A. Grill, P. Patel. Tribochemistry of diamond-like carbon coatings in various environments. Surf. Coat. Technol. 68/69, 626-631 (1994)

[33] J. C. Sánchez-López, A. Erdemir, C. Donnet. Friction-induced structural transformations of diamondlike carbon coatings under various atmospheres. Surf. Coat. Technol. 163-164, 444-450 (2003)

[34] Y. Liu, A. Erdemir, E. I. Meletis. An investigation of the relationship between graphitization and frictional behavior of DLC coatings. Surf. Coat. Technol. 86-87, 564-568 (1996)

[35] K. Jia, Y. Q. Li, T. E. Fischer, B. Gallois. Tribology of diamond-like carbon sliding against itself, silicon nitride, and steel. J. Mater. Res. 10, 1403-1410 (1995)

[36] J. L. Loubet, M. Bauer, A. Tonck, S. Bec, B. Gauthier-Manuel. in: Nastasi M., Parker D. M., Gleiter H., editors. Mechanical Properties and Deformation Behavior of Materials Having Ultra-Fine Microstructures, Kluwer Academic Publishers; 1993, p. 429-4

7 Summaries

In this thesis, structural characterization of ion-vapor deposited hydrogenated amorphous carbon (a-C:H) coating in terms of the $sp^3/(sp^3+sp^2)$ ratio, sp^2 site clustering structure and fabricated defect distribution has been studied by applying solid state ^{13}C NMR.

Primarily, the $sp^3/(sp^3+sp^2)$ ratio of studied coatings deposited under various substrate bias voltages was obtained by using ^{13}C MAS technique. By comparison, a higher $sp^3/(sp^3+sp^2)$ ratio was obtained by CPMAS spectra, which implies that in studied a-C:H coatings, there is a preferential coordination of hydrogen atoms to sp^3 C. Consistently, the mechanical properties of studied a-C:H coatings are not rigidly correspond to the total fraction of sp^3 C, but to the fraction of diamond-like cross-linked sp^3 C-C bonds.

Secondly, by employing ^{13}C MAS and ^{13}C CPMAS techniques, a heterogeneous nanoclustering structure composed of two distinct types of sp^2 C clusters were discovered in studied a-C:H coatings. One of them denoted as sp^2 C′ in content of 3~12 at.% is specifically localized in hydrogen-free regions, and the other in majority denoted as sp^2 C″ is hydrogenated or at least proximate to hydrogen atoms. The size of sp^2 C clusters is strongly dependent on ion energy in deposition process and thus affects the disordering of carbon network in medium range order. On basis of the notably consistent dependence of sp^2 C′ fraction and Raman G peak width on bias voltage within 0.5~3.5 kV, a heterogeneous nanoclustering model of sp^2 sites has been proposed that the sp^2 C′ sites are embedded between dominant sp^2 C″ clusters and sp^3 C matrix as grain boundaries or trapped interfaces where sp^2 hybridized bonding are highly distorted. Also, according to the Raman and optical band gap characterizations, the variation of cluster size in dependence on bias voltage was classified. When bias voltage is below 1 kV, there is a low localization of sp^2 C" sites with small cluster size so that the fraction of boundary sp^2 C' sites is also few; as it grows to 1.0~2.5 kV,

higher ion energy enhances the clustering of sp^2 C into six-fold aromatic rings so that both the size and population of sp^2 C" clusters increases largely, and accordingly the fraction of boundary sp^2 C' sites increases obviously. A further increase of bias voltage may promote a large expansion of sp^2 C" clusters through integration and reordering of individual sp^2 C" clusters into larger ones, so that the fraction of boundary sp^2 C′ sites will decrease significantly in turn.

Next, the validity of presented heterogeneous clustering model was confirmed by an exponential fitting analysis on magnetization relaxation curve of sp^2 C″, sp^2 C′ and sp^3 C spins by using saturation recovery technique. Results revealed that the spin-lattice relaxing of sp^2 C″ spins were considerably affected by paramagnetic centers with stretched index α equal 0.8 and T_1 equal 2.8 s, while the sp^2 C′ spins and sp^3 C spins showed a weak influence sp^3 C spins with T_1 equal 5 s and 3.7 s, respectively. Such differences of T_1 among sp^2 C″, sp^2 C′ and sp^3 C spins verify the heterogeneous structure of studied a-C:H coatings, and the stretched-exponential approximation of sp^2 C″ spins obviously suggests a partial distribution of paramagnetic centers near sp^2 C″ clusters. For ^{1}H spins, the magnetization recovery curves showed fine stretched-exponential approximation with stretched index α about 0.5 and T_1 within 20~40 ms and better bi-exponential approximation with two T_1 components fluctuating within 25~55 ms and 0.1~0.3 ms in fraction of 70~80% and 30%~20%, respectively. Both the ultra short component of T_1(H) and the stretched index α approaching 0.5 certainly suggest considerable presence of paramagnetic centers in studied coatings. An interrupted ^{13}C CPMAS saturation recovery spectra with relaxing interval as the short component of T_1(H) showed that most of quick-relaxing protons localize in sp^2 C″ clusters but nearly absent in sp^3 matrix and boundary sp^2 C' sites.

Finally, considering the unique heterogeneous structure and their effects on tribological properties of studied coating, tribotests were conducted in N_2 atmosphere and ambient air by using a standard ball-on-plate tribometer. Obvious correlations between nanoclustering structure and friction performance of a-C:H coatings has been

observed especially in N_2 atmosphere. Comparatively higher friction coefficient generally occurred in phase of diamond-like coatings, namely as bias voltage was 1.0~2.0 kV, while lower friction coefficient usually occurred in polymer-like and graphite-like coatings (still with hydrogen content about 18 at.%). A characterization of wear marks by Raman spectroscopy demonstrated that compared with as-deposited coating, the ball scar derived from B2.0 coating showed largest growth of *I(D)/I(G)* and reduce of G peak width with moderate upward shift of G peak position which implied a great transformation of sp^3 C to amorphous sp^2 C in aromatic rings, while the ball scar derived from B0.5 coating showed a reduce of *I(D)/I(G)* and G peak width with moderated upward shift of G peak position which implied a transformation of sp^2 C from aromatic rings to chains, in coordination with hydrogens and showing good solid lubricity. It was inferred that the boundary sp^2 C' sites trapping around sp^2 C" clusters may inhibit the formation of lubricant transfer layers enriched of sp^2 C-H bonds in chains under dry sliding conditions and lead to high friction coefficient. By comparison, the overlapping tribotests of a-C:H coating/steel ball tribopairs in ambient air showed that with the presence of oxygen and water molecule in sliding atmosphere, the noticeable oxidizing tribochemical reactions would play a dominant role in the determination of lubricant properties of transfer layers.

Publications

I. Journals

[1] Jiao Xu, Masahiro Kawaguchi, Takahisa Kato. *Evolution of transfer layers on steel balls sliding against hydrogenated amorphous carbon coatings in ambient air.* Tribology International. 70, 42-51(2014)

[2] Jiao Xu, Sadayuki Watanabe, Hideo Hayashi, Masahiro Kawaguchi, Takahisa Kato. *Structural characterization of ion-vapor deposited hydrogenated amorphous carbon coatings by solid state 13C nuclear magnetic resonance.* Journal of Applied Physics. 115, 014303 (2014)

II. Important Proceedings and Conferences

[3] Jiao Xu, Sadayuki Watanabe, Hideo Hayashi, Masahiro Kawaguchi, Takahisa Kato. *Structure characterization of hydrogenated amorphous carbon coating by solid state ^{13}C NMR.* Proceedings of JAST Tribology Conference, Tokyo, Japan, May 2014.

[4] Jiao Xu, Sadayuki Watanabe, Hideo Hayashi, Masahiro Kawaguchi, Takahisa Kato. *Structure characterization of ion-vapor deposited a-C:H coating by solid state 13C NMR.* The 7th China International Symposium on Tribology (CIST 2014), Xuzhou, China, Apr. 2014.

[5] Jiao Xu, Sadayuki Watanabe, Hideo Hayashi, Masahiro Kawaguchi, Takahisa Kato. *Quantifying sp^2C/sp^3C of hydrogenated Amorphous Carbon Coatings by Solid State ^{13}C Nuclear Magnetic Resonance.* Proceedings of JAST Tribology Conference, Tokyo, Japan, May 2013.